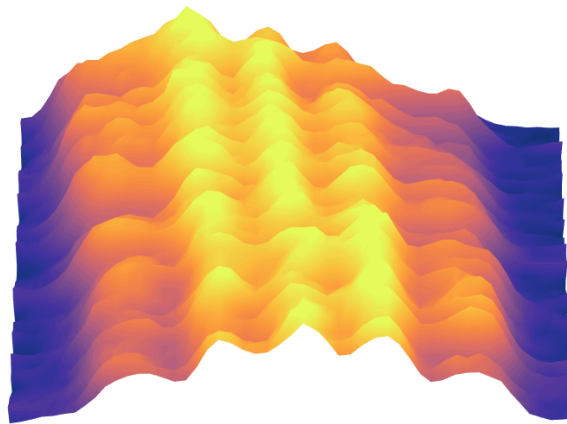

A TALE OF TWO INTERFACES

PHOTONS AND SPINS LINKED BY A SOLID-STATE ARTIFICIAL
ATOM



This thesis is submitted for the degree of
Doctor of Philosophy

Magdalene College, University of Cambridge

Candidate: Jonathan H. BODEY
Supervisor: Prof. Mete ATATÜRE

July 2021

Cover illustration: 3D plot of data in Fig. 5.7 (a)

For Andrew and Angela Bodey.

Abstract

An electron spin confined to a self-assembled quantum dot presents itself as a natural candidate for the node of a quantum network, offering a highly coherent interface between a solid-state spin and an optical photon. Crucial to the construction of such a network will be the exploitation of the long-lived coherence of the surrounding environment of nuclear spins. This dissertation presents a series of experiments which address some of the challenges of exploiting quantum dots for quantum technologies.

First, we implement a new technique for performing coherent control of a spin confined to a quantum dot, achieving the highest control fidelity ever reported in this type of system. The technique is fully flexible, meaning that we can programmatically design control sequences of arbitrary complexity.

Next, we use this control technique to mitigate the unwanted effects of the nuclear spin environment on the electron spin. We show that we can tune the rate of coupling to the nuclei, allowing us to protect a known quantum state stored on the electron spin by taking it out of resonance with environmental modes.

We then show that we can resolve collective spin-wave modes of the nuclei, each associated with a single spin flip distributed among the ensemble. By probing the coupling frequency between the electron spin and these nuclear modes, we show how to extract information about the population distribution of the nuclear ensemble across its single-particle spin-states. In our case, this procedure reveals the presence of entanglement within the nuclei, manifesting itself as a many-body dark state.

Finally, we perform the first spin-control experiments of an electron spin confined to an optically active gallium arsenide quantum dot. We demonstrate coherent control of an electron spin, and probe its coherence via free induction decay and Hahn-echo spectroscopy.

The scientific insights and technical knowledge gained from this work could enable the construction of a quantum dot system consisting of a qubit (an electron spin) and a high-fidelity, *in situ* quantum memory (the ensemble of nuclear spins). This leads towards the assembly of a physically distributed, coherently connected array of quantum dots: a quantum network.

Declaration

This dissertation is the result of my own work and includes nothing which is the outcome of work done in collaboration except as declared in the Preface and specified in the text.

It is not substantially the same as any that I have submitted, or, is being concurrently submitted for a degree or diploma or other qualification at the University of Cambridge or any other University or similar institution except as declared in the Preface and specified in the text. I further state that no substantial part of my dissertation has already been submitted, or, is being concurrently submitted for any such degree, diploma or other qualification at the University of Cambridge or any other University or similar institution except as declared in the Preface and specified in the text.

It does not exceed the prescribed word limit of 60,000 words, including abstract, tables, footnotes, and appendices.

Jonathan H. Bodey

July 2021

Acknowledgements

The work contained in this dissertation is the culmination of almost 4 years of collective efforts, and some thanks are due to those who made it happen.

Firstly, I want to thank my supervisor, Prof. Mete Atatüre, for giving me the opportunity to work in his group. Practically speaking he provides equipment and money, but much more importantly he supplies the enthusiasm and drive which underpins all of the work presented here. He even once forgave me for making him stand in silence in front of a large audience at the APS March meeting for several minutes whilst my ancient computer restarted.

Next, Rob Stockill and I took the measurements of Chapter 3 (and the start of Chapter 4) together. Claire Le Gall then joined me in the lab for the remaining measurements of Chapter 4, as well as performing all of the associated modelling. It is only with hindsight that I can appreciate just how patient Rob & Claire were in teaching me how to run the experiments. I really learnt a lot from working with them. I'm also extremely grateful to Claire (for the 14th time, and counting!) for critically reading this thesis.

Gabriel Éthier-Majcher and Dorian Gangloff are responsible for develop-

ing the nuclear spin cooling technique detailed in Chapters 4 & 5. On top of this, Dorian's guidance and vision underpins the results of Chapter 5. Both Gabriel and Dorian provided stimulating and relaxed company in the lab, in the pub, and away on conferences (Toronto with Gabriel / Rome, Boston & Paris with Dorian). I only regret Gabriel's taste in t-shirts, and Dorian's liking of ice-cold showers.

Clara Bachorz and I took the data in Chapter 5 together, and Leon Zaporski performed all of the modelling. The results of Chapter 6 were then a team effort between Leon and me. Both were very effective lab-mates, and we had a lot of fun together. If I could have had just another month with Leon in the lab, maybe I could have finally persuaded him to start using a lab book.

Daniel Jackson deserves credit for his top quality lab company, expert assistance with experimental issues (especially python), impeccable musical taste, and for all the times he fixed the printer. He still doesn't deserve Shakira though.

The rest of the quantum dot team during my time here also of course merit a mention: Lukas Huthmacher (fellow rower, cyclist, and Porcupine Tree enthusiast), the indefatigable Constantin Lang, and newest members Urs Haeusler and Noah Shofer (the future of QDs is bright - no pun intended).

Next on the list, I have to acknowledge those responsible for first luring me into the Quantum Optical Materials and Systems research group: Dhiren Kara, and also Matteo Barbone and Alejandro Rodriguez-Pardo Montblanch. I'm grateful to all the members past and present of the wider QOMS team for making it such a great place to work - you will all be missed.

Lastly, I am fortunate to be able to credit my parents (and my siblings)

for their unconditional support, without which this thesis (and all of the preamble...) would not have been possible. Emily has been there for me throughout the last 4 years, and a few more before that as well, and I couldn't have done it without her.

Contents

1	Introduction	1
2	InGaAs Quantum Dots: Methods and Phenomena	4
2.1	Sample structure	5
2.2	Bound states	8
2.2.1	Neutral exciton	10
2.2.2	Negatively charged exciton	11
2.2.3	Positively charged exciton	12
2.3	Experimental setup	14
2.4	Experimental techniques	16
2.4.1	Photoluminescence	16
2.4.2	Resonance fluorescence	19
2.5	Quantum dot spin control	28
2.5.1	In principle	29
2.5.2	In practice	32
2.5.3	Experimental setup	33
2.6	Nuclear spin interactions	35
2.6.1	Physical origin	35
2.6.2	Nuclear spin feedback	38

2.7	Spin coherence	40
2.8	Summary	47
3	Flexible Control of a Spin in a Quantum Dot	49
3.1	Background	50
3.2	Spin control in the rotating frame	52
3.3	Experimental setup	55
3.4	Driven spin-Rabi oscillations	56
3.5	Dependence on power	58
3.6	Dependence on single-photon detuning	59
3.7	Ramsey interferometry I	60
3.8	Phase control	62
3.9	Ramsey interferometry II	64
3.10	Pulse fidelity	66
3.11	Conclusions and Outlook	68
4	Optical Spin Locking of a Solid-State Qubit	71
4.1	Experimental setup	72
4.2	Preliminary spin control	73
4.3	Composite control sequences	74
4.4	Nuclear state preparation	77
4.5	Coherent electron spin control	84
4.6	A return to composite pulses	85
4.7	Power dependence of Rabi oscillations	89
4.7.1	Fitting in the low-power regime	90
4.7.2	The three regimes of electron Rabi oscillations	93
4.7.3	Hartmann-Hahn resonances in a QD	95

4.8	Spin locking	99
4.8.1	The three regimes of spin locking	100
4.8.2	State preservation using spin locking	102
4.9	Laser-induced spin relaxation	105
4.10	Conclusions & Outlook	107
5	Quantum Correlations in a Mesoscopic Ensemble	109
5.1	A many-body system of nuclear spins	110
5.2	Nuclear magnons in quantum dots	114
5.3	Magnons as a measurement technique	119
5.4	Polarising using Raman cooling	121
5.5	Probing magnon asymmetry	123
5.6	Species-resolved spin-state reconstruction	126
5.7	Full population reconstruction	131
5.8	An entangled many-body state	133
5.9	Conclusions and Outlook	139
6	A Spin Confined to a GaAs Quantum Dot	142
6.1	Background	143
6.2	Sample structure	145
6.3	Experimental setup	146
6.4	Sample characterisation	148
6.5	Spin lifetime	151
6.6	Spin control	155
6.7	Spin coherence	155
6.7.1	Ramsey interferometry	155
6.7.2	Hahn-echo spectroscopy	159

6.8	Line stability	160
6.9	Conclusions and Outlook	161
7	Conclusions and Outlook	165
	Appendices	169
A	Microwave system	170
A.1	Setup #1: Phase-disabled hole spin control	170
A.2	Setup #2: Phase-enabled hole spin control	171
A.3	Setup #3: Electron spin control	172
A.4	Setup #4: Nuclear spin polarisation	173

List of Figures

2.1	Schematic diagram of our layered QD sample structure.	7
2.2	QD-confined spin band structure schematic.	9
2.3	QD exciton level structure.	11
2.4	Simplified experimental setup diagram.	14
2.5	QD photoluminescence spectrum.	17
2.6	Photoluminescence as a function of gate voltage.	18
2.7	Saturation curve.	24
2.8	Resonance fluorescence on the neutral and negative excitons.	26
2.9	Resonance fluorescence on the negative exciton, under applied external magnetic field in Voigt geometry.	28
2.10	A spin Rabi rotation driven by an ultrashort pulse.	31
2.11	A schematic of our construction apparatus for sequences of ultrashort pulses.	34
2.12	A schematic diagram of the “dragging” process.	39
2.13	Ramsey interferometry of a QD electron spin.	43
2.14	Hahn echo of an electron spin.	45
3.1	X^+ level diagram.	51
3.2	Microwave modulation schematic.	53

3.3	Rabi oscillations as a function of microwave detuning.	57
3.4	Rabi oscillations as a function of drive power.	59
3.5	Rabi oscillations as a function of single-photon detuning.	60
3.6	Ramsey interferometry as a function of detuning.	62
3.7	Ramsey interferometry at zero delay, demonstrating drive phase control.	63
3.8	Ramsey interferometry as a function of detuning, using a nuclear spin feedback cancellation technique.	66
3.9	Rabi oscillations and extracted Rabi frequency as a function of power.	67
4.1	Preliminary electron spin control.	73
4.2	Electron spin control using a simple composite pulse.	76
4.3	Introduction to nuclear spin state preparation using Raman cooling.	78
4.4	Ramsey interferometry on an electron spin in a cooled nuclear spin bath.	82
4.5	Rabi oscillations as a function of single-photon detuning, along with fidelity and Q factor.	84
4.6	Testing the fidelity of composite rotations against regular pulses.	87
4.7	Rabi oscillations versus Rabi frequency.	89
4.8	Electron spin Rabi at low power.	92
4.9	Extracted parameters vs. Ω	93
4.10	Hartmann-Hahn level diagram.	96
4.11	Nuclear level spectral densities.	97
4.12	Modelled decay rate and Q factor.	98
4.13	Spin locking pulse sequence.	100

4.14 Spin locking vs. power.	101
4.15 Modelled spin locking.	103
4.16 Full spin-locking decay profile.	104
4.17 Optically induced spin relaxation.	106
5.1 Nuclear spin distribution schematic.	112
5.2 Electro-nuclear ladder of states.	115
5.3 The emergence of nuclear magnons.	117
5.4 Magnons between nuclear levels.	119
5.5 Raman dragging schematic.	122
5.6 Cooling performance vs. Overhauser shift.	123
5.7 Magnon spectrum vs. Overhauser shift.	124
5.8 Coherent magnon injection.	126
5.9 Deconvolved magnon spectrum.	127
5.10 Arsenic spin-state population differences.	130
5.11 Arsenic spin-state populations.	132
5.12 Arsenic spin-state distributions.	133
5.13 Species-specific asymmetry-commensurate polarisations.	136
5.14 Entanglement in a nuclear ensemble.	138
6.1 GaAs QD sample.	147
6.2 PL of a GaAs QD at 0 T.	149
6.3 Neutral exciton RF.	149
6.4 PL of a GaAs QD at 6.5 T.	151
6.5 RF map of X^-	152
6.6 Spin pumping pulse sequence schematic.	153
6.7 Spin pumping vs. laser power.	153
6.8 A lower bound on spin lifetime.	154

6.9	Rabi oscillations of an electron spin in a GaAs QD.	156
6.10	Ramsey interferometry on an electron spin in a GaAs QD . . .	156
6.11	Spin coherence of a GaAs QD.	158
6.12	Hahn-echo spectroscopy of a GaAs QD.	159
6.13	QD count rate over time.	160
6.14	QD frequency over time.	162
A.1	Microwave setup #1 schematic.	171
A.2	Microwave setup #2 schematic.	171
A.3	Microwave setup #3 schematic.	172
A.4	Microwave setup #4 schematic.	174

Chapter 1

Introduction

In recent decades since the introduction of Erwin Schrödinger's foundational wave equation for particles [1], the fundamentally quantum nature of the world has consistently been supported by several keystone discoveries [2–7]. More recently, the study of many-body systems governed by quantum laws [8, 9] has motivated the development of a technique to simulate their behaviour. Quantum physics can be exploited for this task by assembling large-scale entangled states of coherent quantum objects [10]. These objects are often two-level systems, referred to as quantum bits or qubits accordingly [11]. Distributed entanglement is emerging as an extremely powerful resource, providing novel routes to information processing and secure communication [12–15]. These two avenues are elegantly combined under the quantum internet - a physically distributed network of coherently connected quantum bits [16].

Early work towards assembling a quantum network centred on single atoms [17] and ions [18–20], thanks in part to their outstanding environ-

mental isolation. More recently, highly sophisticated design and fabrication have enabled the study of local (single chip) networks of qubits housed on superconducting circuits [21–24] and in defects in silicon [25, 26]. However, the construction of a spatially distributed quantum network relies on both scalability and efficient interface with photonic channels. This dual requirement brings solid-state quantum emitters - where a defect in a crystalline structure supports optical excitation - into the limelight [27]. There are many such systems, including atomic defects in diamond [28], emitters in two-dimensional materials [29], and single charges in semiconductors [30], each with its own unique advantages and challenges.

The platform for this dissertation will be a mesoscopic defect (10^5 atoms) of indium-gallium arsenide embedded in a gallium arsenide bulk. Since the defect has a smaller bandgap than the bulk, this can give strong confinement of a resident electron, quantising its energy spectrum. This structure, known as a quantum dot (QD), can have a very strong interaction with light, allowing for measurement and control of a confined spin. Whilst these spins themselves have been proposed as a platform for quantum information processing [31–33], the best-in-class spin-photon interface makes the QD an attractive candidate for the source of entangled states of photons [34–37], and for the node of a quantum network. Several landmark capabilities on the road towards these end goals have been demonstrated, including spin initialisation [38–40], coherent manipulation [41–43], single-shot readout [44, 45], spin-photon [46–48] and spin-spin [49, 50] entanglement. Despite this spectacular progress, there remain several challenges which must be addressed to allow QDs to fulfil their promise as quantum network nodes.

This dissertation will present experiments which focus on addressing some of these challenges. First, in Chapter 2, we will outline the state of

play for InGaAs QDs, alongside the techniques and equipment which we will employ throughout the work. In Chapter 3, we develop a new technique for manipulating a single spin confined to a QD. The advantages of this technique over the previous state-of-the-art allow us to implement arbitrary control sequences, which we use in Chapter 4 to protect a known quantum state from decoherence. We further use this technique to tune the interaction between a confined electron spin and its environment of nuclear spins, which in Chapter 5 allows us to probe the state of these nuclei, revealing the presence of many-body quantum correlations. Chapter 6 presents work developing spin control in a new generation of samples, allowing us to probe their spin coherence for the first time. Finally, Chapter 7 concludes the dissertation, and gives some brief perspectives on future experiments.

Chapter 2

InGaAs Quantum Dots: Methods and Phenomena

Modern semiconductor growth techniques and apparatus, notably molecular beam epitaxy [51, 52], have allowed for the production and study of highly sophisticated semiconductor structures. These include self-assembled quantum dots (QDs), consisting of a mesoscopic defect embedded in a bulk semiconductor. If this defect is chosen to have a smaller band gap than the bulk, its energy structure will resemble a trap and allow confinement of charges [53–57].

This condition is met by indium gallium arsenide QDs [58] embedded in a gallium arsenide/aluminium gallium arsenide structure, and this system will be the initial focus of this report. The size and shape of the InGaAs defect give, to a very good approximation, zero-dimensional confinement and the structure is then able to house a selection of bound states [59], the most important of which include single charges, neutral excitons, and singly

charged excitons. These bound states are described by a discrete energy spectrum, giving the QD its alternative name: artificial atom [60–62]. The solid-state nature of a QD, however, means that the physics governing its behaviour is far richer than for a corresponding isolated atom [63].

2.1 Sample structure

InGaAs QDs form spontaneously during Molecular Beam Epitaxy, under a process known as Stranski-Krastanov growth [64, 65]. The 6% mismatch in lattice parameter between InAs and GaAs means that when growing InAs on a GaAs substrate, the interface is strained. After ~ 1.6 monolayers of InAs have been grown, further InAs prefers to nucleate into islands on top of this original layer of InAs (which is termed the “wetting layer”) [66–71]. These islands measure around 20nm in diameter and 5nm in height; strongest confinement is along the growth axis. The QDs are capped with further GaAs to prevent oxidation and interaction with surface states, and we are left with randomly distributed array of InAs clusters made of $10^4 - 10^5$ atoms.

When designing a structure in which to house our QDs, shown in Fig. 2.1 (a), some important considerations are taken into account. Firstly, since the QDs are to be addressed using optics, it is important to maximise the quality of their already excellent optical interface to allow the collection of as many emitted photons as possible. To this end, the QDs are grown on top of a distributed Bragg reflector (DBR) [72], which allows collection of downwardly emitted photons. Placing the QDs at $\frac{\lambda(2n+1)}{4}$ above the DBR ensures constructive interference between photons which reflect from the DBR and photons which are originally emitted upwards by the QD. In ad-

dition, the difference in refractive index of GaAs and air [73] can cause total internal reflection of photons at the sample surface [74]. To mitigate this we top the structure with a super-hemispherical (also called “Weierstrass”) Zirconia solid immersion lens (SIL), giving smaller jumps in refractive index at the interfaces and enhancing collection efficiency [75–77]. The shape of the SIL also serves to funnel photons towards the vertical emission direction.

Secondly, QDs are capable of supporting several different types of bound state, each distinguished by their charge; these bound states are discussed further in Section 2.2. Interfacing the properties of these bound states with optical modes requires that the desired type of bound state can be selected. In addition, the charge state of the QD must be stable, and isolated from electrical noise, in order to achieve sufficient spin-lifetime properties (further discussed in Section 2.7). This is done by integrating the QDs into a Schottky diode structure, shown schematically in Fig. 2.1 (b). Such a diode structure has an in-built junction potential, V_{diode} , leading to a sloped band structure across the diode (Fig. 2.1 [b]). In addition, we make top and back contacts, allowing a voltage bias V_{gate} to be applied across the structure. When this bias is sufficient to bring the energy of a single electron in the QD below the Fermi energy of the n-doped reservoir, a single electron tunnels into the QD. From there, the extra Coulomb energy of an additional charge forms a Coulomb blockade to prevent additional charges from entering [78, 79]. In this way, the charge state of the QD can be straightforwardly selected [80]. This bias additionally exerts a DC Stark effect [81] on the QD level structure, allowing the energy of the transitions to be tuned. The samples are designed to study the neutral and negative excitons and thus are n-doped, allowing easy selection of this charge state by simply selecting a gate voltage such that an electron can tunnel into the QD from the doping

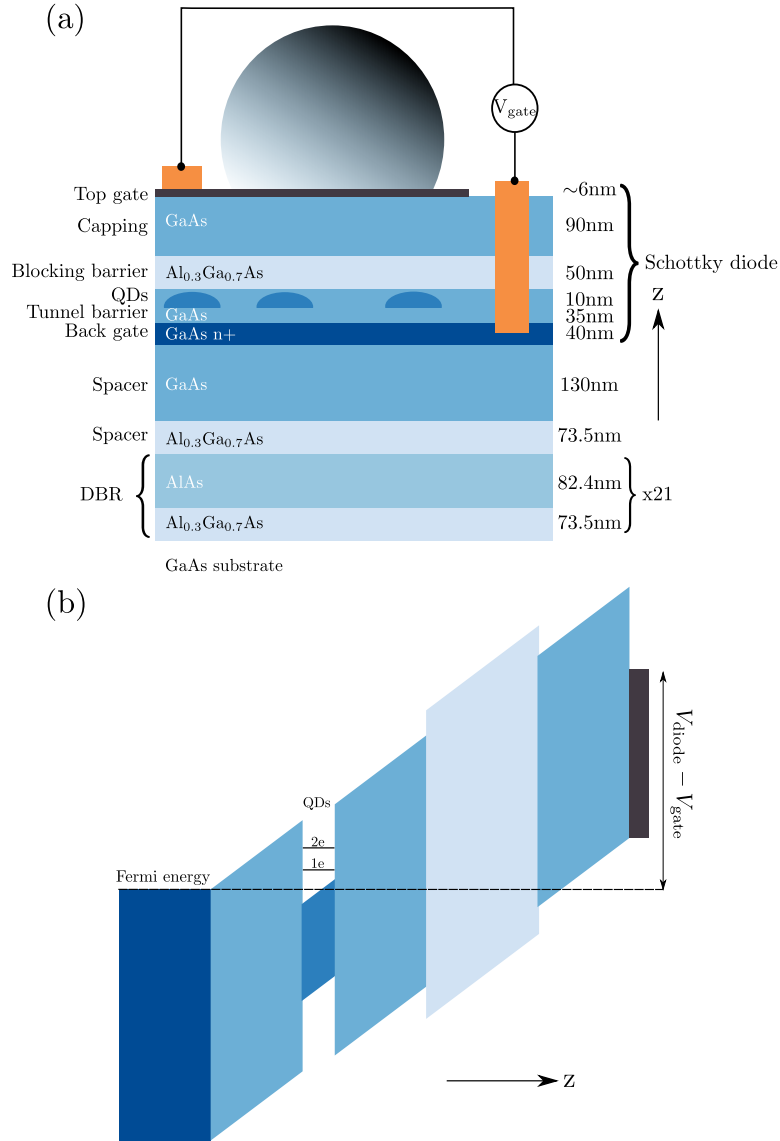


Figure 2.1: The layered sample structure. (a) Schematic side view. The growth direction is labelled by z . (b) Schematic band energies across the Schottky diode, which has an intrinsic bias V_{diode} .

layer. Positive excitons can be studied by driving the neutral exciton transition optically, generating an electron-hole pair, and selecting a gate voltage to tunnel the electron out of the QD. The QDs must be isolated from the n-doped layer in order to avoid fast spin thermalisation with the Fermi sea, and for this reason they are protected by a 35-nm tunnel barrier from below; in order to minimise charge leakage, a 50-nm blocking barrier protects them from above.

The InGaAs samples used in this dissertation were grown at the EPSRC National Centre for III-V Technologies in Sheffield, UK.

2.2 Bound states

The general form of the band structure of a crystal is determined by the type of compounds of which it is composed, and the structure which they adopt. We consider solid state structures based on III-V semiconductors, arranged in the zincblende structure; Figure 2.2 depicts the band structure of such a material. The crystal ground state corresponds to a fully occupied valence band and an empty conduction band, and all other QD states are considered relative to this ground state. The below follows the discussion in [82].

In the region around the Γ point, where the wavenumber $k = 0$, the conduction band (c) consists of an almost-parabolic dispersion and an orbital angular momentum of $L = 0$. This means that an electron in a bound state will have total angular momentum $J = 1/2$ and projection $m_J = \pm 1/2$.

By contrast, the highest-energy valence band states have p-like atomic orbitals, with $L = 1$. Populating with a pseudospin-1/2 hole leads to states with a total angular momentum of $J = 1/2$ and $J = 3/2$, which are split

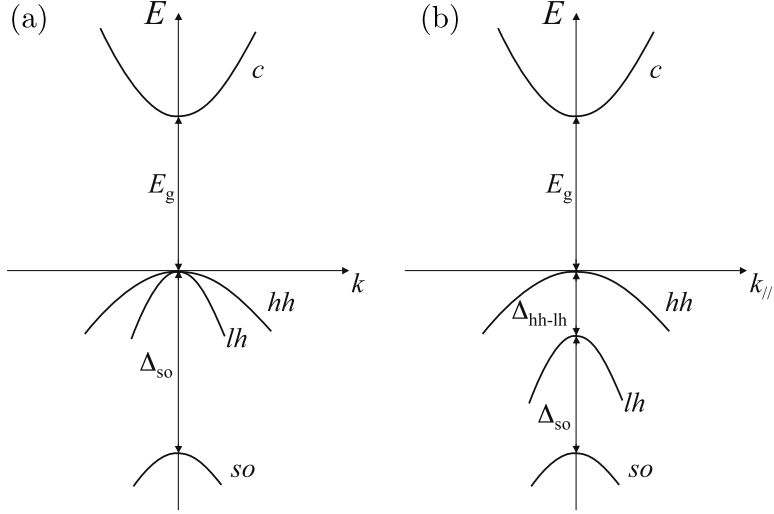


Figure 2.2: A schematic representation of the band structure of a spin confined to a QD in the vicinity of the Γ point, taken from [82]. *c*: conduction band, *hh*: heavy hole, *lh*: light hole, *so*: split off. (a): strain free. (b): uniaxial strain. $k_{||}$: wavevector perpendicular to strain axis.

by the spin-orbit interaction. The $J = 1/2$ states are referred to as the “split-off” (*so*) band thanks to their energy difference Δ_{so} caused by this interaction, which is sufficient to neglect these states from our discussion. The $J = 3/2$ states can take an angular momentum projection of $m_J = 1/2$ and $m_J = 3/2$. The strain present in our samples - an intrinsic part of the QD growth process, discussed further in Section 2.1 - means that the $J = 3/2$ states are split in energy by Δ_{hh-lh} at $k = 0$, with the highest being the state with angular momentum projection $m_J = \pm 3/2$. The relatively shallow curvature for this level earns it the name “heavy hole” (*hh*), due to its high effective mass compared with the $m_J = 1/2$ states (“light hole”, *lh*). This splitting means that all bound states considered in this report are formed using predominantly heavy holes, with a small light hole component. These bound states are discussed below.

2.2.1 Neutral exciton

Optical excitation of the crystal ground state allows an electron to move into the conduction band, leaving a hole in its place; this electron-hole pair is then bound together by the Coulomb interaction. Since a photon is able to transfer ± 1 unit of angular momentum, the formation of a neutral exciton with total angular momentum ± 1 is allowed, and this arrangement is known as a bright exciton. The other possibility is the alignment of the total angular momenta of the electron and the hole, giving the exciton a total angular momentum of ± 2 . The optical generation of this state is forbidden, and it is known as the dark exciton accordingly. Now exclusively considering the case of the bright exciton, whose schematic structure is shown in Figure 2.3 (a), we have the following possible configurations:

$$\psi_x = \frac{1}{\sqrt{2}}(|\uparrow\downarrow\rangle + |\downarrow\uparrow\rangle) \quad (2.1)$$

$$\psi_y = \frac{1}{\sqrt{2}}(|\uparrow\downarrow\rangle - |\downarrow\uparrow\rangle) \quad (2.2)$$

where \uparrow (\downarrow) denotes an electron with total angular momentum $+1/2$ ($-1/2$), whilst \uparrow (\downarrow) refers to a heavy hole with total angular momentum $+3/2$ ($-3/2$). The spin eigenstates are mixed into these states by the spin exchange interaction between the electron and the hole, which is present because the QD is not circularly symmetric [83, 84]; this gives a fine structure splitting Δ_{FS} to the neutral exciton.

The total angular momentum of the energy eigenstates determines the selection rules for optical excitation of the transitions. Since both ψ_x and ψ_y contain equal superpositions of states with angular momentum ± 1 , their angular momentum projection is zero and as a result they must be excited

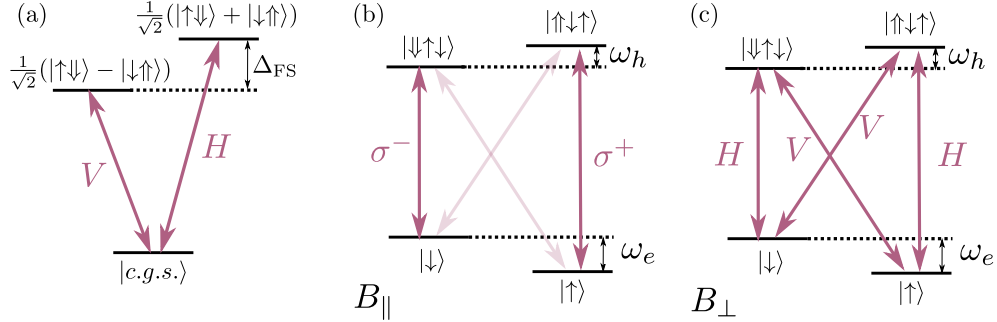


Figure 2.3: \uparrow, \downarrow denotes electron spin, hole pseudospin. (a) The neutral exciton transitions in the absence of magnetic field. Transitions from the crystal ground state (c.g.s.) are split by the fine structure splitting, Δ_{FS} . (b) The negative exciton transitions, under an external magnetic field parallel to the QD growth axis. Diagonal transitions are weakly allowed via the small light-hole component present in the excited states. (c) Same as (b), but under an external magnetic field perpendicular to the QD growth axis. In this case the z-eigenstates are mixed, giving four linearly polarised transitions. Their energy separations are dictated by the electron and hole Zeeman energies, ω_e, ω_h .

with linearly polarised light. Applying a magnetic field strong enough to dictate the quantisation axis allows the spin eigenstates to be recovered, returning us to the circularly polarised selection rules which would be present without the effect of spin exchange.

2.2.2 Negatively charged exciton

If instead we start from a ground state of a single electron in the QD, we then have access to a different family of states known as the negative trion, which is depicted in Figure 2.3 (b,c). Optical excitation again generates an electron-hole pair, resulting in an excited state of two electrons in a spin singlet, accompanied by a hole. In this case there is no net electron spin in the excited states, and no hole pseudospin in the ground states, and as a result the spin eigenstates are not affected by any exchange interaction. The states are differentiated solely by the spin of the unpaired particle, which for the ground states is the electron and for the excited states is the hole. This

means that both the ground states and excited states are doubly degenerate in the absence of applied magnetic field.

In the presence of an external magnetic field along the QD growth axis (“Faraday geometry”, Fig. 2.3 [b]), the selection rules require circularly polarised light for the transitions $|\uparrow\rangle \leftrightarrow |\uparrow\downarrow\uparrow\rangle$ and $|\downarrow\rangle \leftrightarrow |\downarrow\downarrow\uparrow\rangle$. The remaining optical-frequency transitions are forbidden since they require a transfer of ± 2 units of angular momentum by a single photon, and can only take place to first order via the small light-hole component of the excited state pseudospin [38]. In this configuration, therefore, the electron spin states are not coupled to each other via optical transitions.

Aligning the magnetic field perpendicular to the QD growth axis (“Voigt geometry, Fig. 2.3 [c]) defines a new quantisation axis, and the eigenstates can be expressed as superpositions of those defined by the growth axis. Similarly, superposing the circular transitions from Faraday geometry results in four equally favoured, linearly polarised, transitions. Under this condition the electron spin states are connected via two equal-strength Λ -systems consisting of optical-frequency transitions [85]. Because this configuration connects spin states to each other via optical transitions, allowing for coherent spin control [42, 43], Voigt geometry is employed throughout this dissertation.

2.2.3 Positively charged exciton

This system consists of a QD populated by a single heavy hole. This leads to ground states differentiated by hole pseudospin $|\uparrow\rangle, |\downarrow\rangle$ and excited states containing a hole pseudospin singlet and an unpaired electron spin $|\uparrow\downarrow\uparrow\rangle, |\downarrow\downarrow\uparrow\rangle$. The system, known as X^+ , supports the same transitions

as X^- and the two arrangements are largely similar.

Throughout this dissertation, we work mainly with either the negative or the positive exciton, in Voigt geometry. The two-level ground state manifold, formed by the two spin projections of the electron or hole, forms a natural basis in which to conduct qubit control experiments, enabled by optical transitions [86].

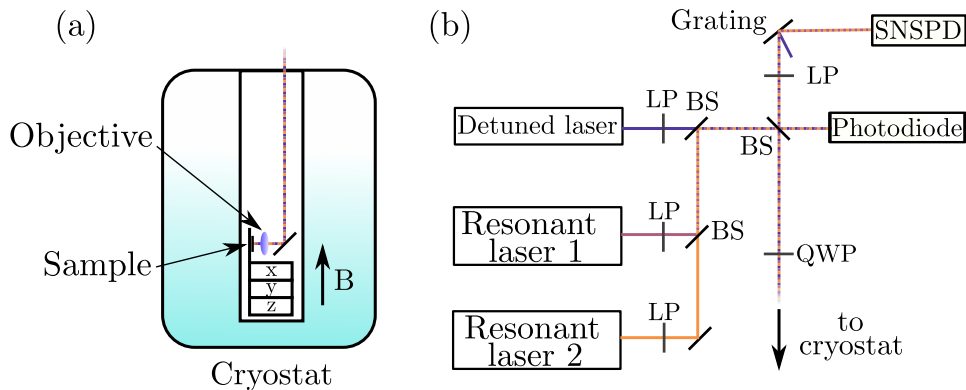


Figure 2.4: A simplified diagram of our setup. (a) Cryostat system, with sample mounted in Voigt geometry. (b) Optical setup. LP: linear polariser, BS: 90:10 beamsplitter, QWP: quarter wave plate, SNSPD: superconducting nanowire single-photon detector.

2.3 Experimental setup

Figure 2.4 contains a schematic diagram of our experimental setup. The solid-state nature of the QD sample means that at ambient temperatures, incoherent scattering via highly occupied phonon modes degrades the quality of optical transitions [87–89]. To mitigate this, we house our sample inside a liquid-helium bath cryostat at 4.2K (Fig. 2.4 [a]). Within the cryostat, the sample is placed inside an insert containing low pressure helium gas, simultaneously ensuring good thermal contact with the liquid helium, and allowing optical access to the sample. The insert is surrounded by superconducting electromagnetic coils, which can generate a magnetic field of up to 9 Tesla along the direction of optical access. For this reason, we must orient the growth axis of the sample perpendicular to the optical axis of the cryostat in order to operate in Voigt geometry. The sample is further mounted on a piezoelectric stack to give nanoscale three-dimensional control over its position, and is further connected electrically to an external voltage source

(not shown), to allow DC Stark shift tuning and charge state selection.

Optical access to the cryostat is achieved using a home-built confocal microscope, depicted schematically in Fig. 2.4 (b), in combination with a 0.5 NA aspheric objective lens immediately before the sample (inside the insert, shown in Fig. 2.4 [a]).

The microscope itself is a dark-field confocal microscope [90]. Linear polarisers on the excitation arms (which can accommodate both resonant and detuned lasers) and collection arms of the microscope allow the laser background, reflected from the sample, to be suppressed by a factor of $\sim 10^5$. Detuned laser background can be additionally filtered using a holographic grating (produced by Spectrogon) which features a 90% diffraction efficiency into the first order mode. The excitation light is sculpted into the desired polarisation (linear, or circular) using a combination of the aforementioned linear polarisers and a quarter-wave plate. Finally, a beamsplitter immediately preceding the cryostat is used to pick off light to send to a photodiode, which allows the excitation power to be stabilised.

These optical modes are shaped into pulses in the time domain using both electro-optic modulators (EOMs) and acousto-optic modulators (AOMs), in series. We use the photodiode signal to feed back on the AOM transmission, in order to stabilise the input power. The EOMs (custom-made by EOSpace) have a 20-GHz bandwidth, which allows us to form short pulses. Whilst an AOM pulse is slower (our AOMs are either 80MHz or 350MHz), we nevertheless use a simultaneous AOM pulse in order to achieve a high pulse suppression ratio, whilst retaining the precise pulse shaping offered by the EOM.

The transmission of an EOM or AOM is tuned via the voltage bias across it. For an AOM, the origin (where transmission is minimised) is always

found when no bias is applied. However, in the case of an EOM, this origin drifts significantly over time, and the bias voltage must therefore be actively stabilised. This is done by monitoring the optical intensity after the EOM. Into the voltage bias we feed the output of a PID loop (SRS SIM960), and the output of a lock-in amplifier (SRS SR830 DSP). The lock-in applies an oscillating bias to the EOM, and is fed the optical intensity after the EOM in return. Using the PID stabiliser to set the error signal of the lock-in to zero, with the correct sign of the P parameter of the stabiliser, ensures that we remain at the minimum of EOM transmission (changing the sign of P moves us to a transmission maximum).

In order to detect signal from our QD, we use either a spectrometer (in which case we must of course bypass the grating), a silicon-based avalanche photodiode (APD), or (most commonly) a superconducting nanowire single-photon detector (SNSPD). In all, we achieve an estimated photon detection efficiency of around 0.1% (0.4%) with an APD (SNSPD).

The inputs and outputs of the microscope are delivered from the lasers and to the detectors using a series of optical fibres.

2.4 Experimental techniques

Having established the QD bound states of interest and the general setup with which we can study them, we now proceed to the techniques used to perform our experiments.

2.4.1 Photoluminescence

Photoluminescence (PL) refers to optical emission which is optically activated by a non-resonant laser. In the case of InGaAs QDs, optical activation

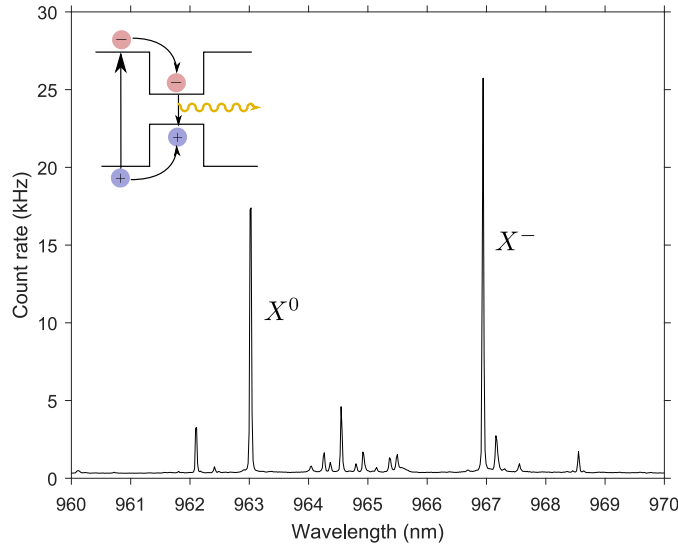


Figure 2.5: A typical QD photoluminescence spectrum. The two most prominent lines are labelled with their exciton complex. Inset: schematic of the PL excitation and recombination channel.

is achieved using a 780nm laser. Because this is above the band gap of the structure, valence band electrons can be promoted to the conduction band, leaving a hole behind. These free charge carriers enter the wetting layer, where they form excitons. When in the vicinity of a QD, excitons can relax non-radiatively into the lowest-energy state, before radiative recombination (inset to Fig. 2.5). The frequency of recombination is characteristic of the QD and exciton complex and depends on the competition of confinement strength, binding energy, and Coulomb repulsion.

Passing the collected light to a spectrometer results in a spectrum such as the one shown in Fig. 2.5. Laser background is automatically filtered by its large detuning from the optical transitions. The spectrum contains multiple lines because our optical excitation can load the structure with charges, and the resulting recombination channels will all be observed in

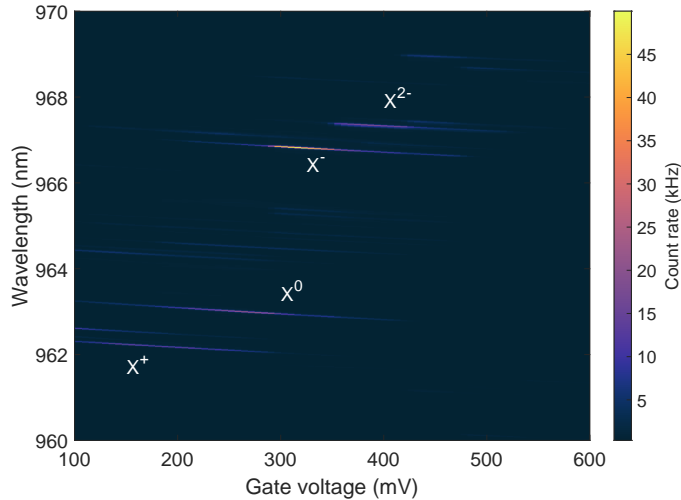


Figure 2.6: A photoluminescence spectrum, as a function of applied voltage bias. Lines shift linearly with gate voltage thanks to the DC Stark shift, and disappear outside of a fixed gate voltage range as the QD is loaded with different charge configurations.

a time-averaged measurement. In this spectrum, we observe two bright, narrow peaks at 963nm and 967nm, corresponding to the neutral exciton (X^0) and the negative exciton (X^-) respectively. The 10-GHz resolution of our spectrometer does not allow us to resolve the fine structure splitting of X^0 . The 4-nm redshift of X^- relative to X^0 , a hallmark of these InGaAs QDs which allows assignment of these two lines, is caused by the competition between the changes in Coulomb energy and binding energy of the two complexes [82].

Now varying the gate voltage across the sample whilst measuring PL, we bring different QD excitons into stability, resulting in the PL map presented in Fig. 2.6. As the bias voltage is increased, states of increasing negative charge sequentially come into stability. Each of these is visible over a gate

voltage range (often called a charging plateau), the middle of which exhibits long-lived (\sim ms) charge states. Across its plateau, the emission wavelength of an exciton is tuned with gate voltage via the DC Stark shift. At certain gate voltages, multiple lines are visible, for the reasons given above.

This technique allows the emission frequencies and gate voltage stability plateaus for the excitons of interest (which for this work are the X^+ , X^0 , and X^-) to be characterised. During this stage of characterisation, we also align our QD and microscope in order to maximise collection efficiency. PL is a crucial step in characterising a QD, but does not allow for coherent interaction with the QD bound states; emission under PL is entirely spontaneous (i.e. incoherent).

2.4.2 Resonance fluorescence

Theoretical introduction: Resonance fluorescence (RF) here refers to the interaction between near-resonant optical modes and the bound states of our QD. Here, we outline the essential principles of operation, using the simple example of a two-level system. Whilst a full quantum treatment can be used [91], identical results are realised semiclassically, by treating the optical field as a classical field [92, 93], and we here adopt the latter approach for simplicity.

First, we introduce the Hamiltonian for our two-level system, which consists of a ground state $|g\rangle$ and an excited state $|e\rangle$, separated by an energy ω :

$$\hat{H}_0 = \hbar\omega |e\rangle \langle e|. \quad (2.3)$$

We then introduce a drive field, with electric field strength E_0 , at fre-

quency ω_L , and which without loss of generality we assume to be linearly polarised along the x axis. The interaction Hamiltonian can be written:

$$\hat{H}_1 = -\vec{d} \cdot \vec{x} E_0 \cos \omega_L t \quad (2.4)$$

where \vec{x} is a unit vector along the x axis, and \vec{d} is the electric dipole operator.

Then, the Hamiltonian can be expressed in the rotating frame, corresponding to removing a common rotation at ω_L from all terms. In addition, we make the rotating wave approximation, since we are concerned with the case where our drive field is near-resonant. We arrive at:

$$\hat{H} = -\hbar\delta |e\rangle \langle e| + \frac{\hbar\Omega}{2} (|e\rangle \langle g| + |g\rangle \langle e|) \quad (2.5)$$

where $\delta = \omega_L - \omega$ refers to the detuning of the drive field from the transition frequency, and $\Omega = -E_0 \langle e | \vec{d} | g \rangle / \hbar$ is the Rabi frequency at which the two levels are coupled [94].

Of course, introducing an additional term to the Hamiltonian changes the eigenbasis of the system, which becomes:

$$|+\rangle = \sin \theta |g\rangle + \cos \theta |e\rangle \quad (2.6)$$

$$|-\rangle = \cos \theta |g\rangle - \sin \theta |e\rangle \quad (2.7)$$

with a mixing angle $\theta = \arctan \left[\Omega / (\delta + \sqrt{\Omega^2 + \delta^2}) \right]$; these states are termed the dressed states. The eigenenergies which accompany these dressed states are:

$$E_{\pm} = \frac{\hbar}{2} \left(\delta \pm \sqrt{\Omega^2 + \delta^2} \right). \quad (2.8)$$

This energy shift from the bare, undriven eigenenergies is termed the Autler-Townes splitting [81,92,95]. These effects, which are hallmarks of the coherent light-matter interaction with a two-level system, were first observed in atomic systems [96,97] and were later measured in self-assembled QDs [98–100].

In order to arrive at a description which corresponds to physical reality, we include relaxation into our example. To do this, we express the decay rate from $|e\rangle$ to $|g\rangle$ as Γ , which sets a lifetime $T_1 = 1/\Gamma$ on the excited state. At the same time, we move into the density matrix formalism, where the density matrix for a general state $|\psi\rangle$ is:

$$\rho = |\psi\rangle\langle\psi| = \begin{pmatrix} \rho_{ee} & \rho_{eg} \\ \rho_{ge} & \rho_{gg} \end{pmatrix}. \quad (2.9)$$

The diagonal terms, often named the populations, give the probability of finding the system in $|g\rangle$ and $|e\rangle$, as denoted by their indices. The off-diagonal terms, called the coherences, describe the phase relationship between $|g\rangle$ and $|e\rangle$ when they are present in superposition.

In this formalism, the equations of motion can be found:

$$\dot{\rho} = -\frac{i}{\hbar}[\hat{H}_1, \rho] - \frac{1}{2}\{c^\dagger c, \rho\} + c\rho c^\dagger \quad (2.10)$$

and using the following dephasing matrix, to include the excited-state lifetime:

$$c = \frac{1}{\sqrt{T_1}} \begin{pmatrix} 0 & 0 \\ 1 & 0 \end{pmatrix} \quad (2.11)$$

we arrive at:

$$\dot{\rho}_{ee} = i\frac{\Omega}{2}(\rho_{eg} - \rho_{ge}) - \frac{\rho_{ee}}{T_1} (= -\dot{\rho}_{gg}) \quad (2.12)$$

$$\dot{\rho}_{ge} = i\frac{\Omega}{2}(\rho_{gg} - \rho_{ee}) - \rho_{ge}\left(\frac{1}{2T_1} + i\delta\right) (= (\dot{\rho}_{eg})^*). \quad (2.13)$$

These expressions elegantly capture the coherent nature of the driven transfer of population between $|g\rangle$ and $|e\rangle$; the rate of change of these populations is intimately connected to generation of coherences in the system, and vice versa. In addition, we note the rate of population relaxation is $1/T_1 = \Gamma$, as we imposed. However, the rate of loss of coherence is limited to $1/(2T_1)$, which denotes the so-called transform limit where decoherence is driven exclusively by relaxation [101]. More generally, we can write the decoherence rate:

$$\frac{1}{T_2} = \frac{1}{2T_1} + \gamma_2 \quad (2.14)$$

where the coherence time T_2 now accounts for an additional pure dephasing rate γ_2 , at which coherence is removed from the system without affecting populations. This is a general expression and can be applied to any two-level system; later in this discussion, it will be particularly relevant to the ground-state manifolds of X^- and X^+ , consisting of two spin projections (see Section 2.7). However, we can also use it to describe the coherence of photon emission (i.e. we take the two levels to be, for example, the crystal ground state and one of the X^0 optical excited states). In this case, the excited-state lifetime is usually a few hundred ps [102], and because the excitation process is typically much slower than this, we can take the system to be at steady state. For optical transitions in QDs, we can encounter two

main dephasing channels. The first is spectral wandering which is slow when compared to the lifetime, and which can be straightforwardly modelled by considering a spread of transition frequencies. The second stems from interaction with the phonon bath, giving rise to a phonon sideband (biased towards redshifted emission due to temperature-suppression of phonon absorption [103]) which can be spectrally filtered due to its non-Markovian nature [104]. Experimental studies have shown that pure dephasing is not relevant to QD optical transitions [105, 106]. Nevertheless, we keep the following expressions general by including T_2 .

In the steady state, Eqs. 2.12 and 2.13 both equal zero, and we can straightforwardly calculate the excited-state population:

$$\rho_{ee} = \frac{1}{2} \frac{\Omega^2}{(T_1 T_2)^{-1} + \delta^2 T_2 T_1^{-1} + \Omega^2}. \quad (2.15)$$

It is convenient to define the saturation parameter, $s = T_1 T_2 \Omega^2$, which allows us to recast Eq. 2.15 in the following form:

$$\rho_{ee} = \frac{1}{2} \frac{s}{1 + s + \delta^2 T_2^2}. \quad (2.16)$$

This expression has a maximum value of $\frac{1}{2}$, which it approaches as $s \rightarrow \infty$. The excited state population expressed here is directly proportional to the count rate measured experimentally, with the proportionality constant set in our case by the QD brightness and experimental collection efficiency. When using a drive field which is resonant with the transition i.e. $\delta = 0$, we obtain the data presented in Fig. 2.7, alongside which is plotted a fit of the form shown in Eq. 2.16.

Saturation measurements such as these are very important for our ex-

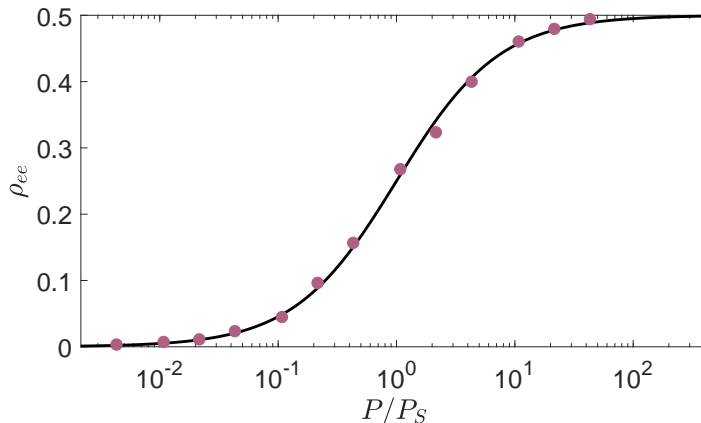


Figure 2.7: Count rate of the low energy X^0 transition at 0 T (pink circles) under resonant excitation, as a function of excitation power P . A fit of the functional form $a \frac{P}{P+P_S}$ (black curve) allows the saturation power P_S and count rate when $\rho_{ee} = 0.5 a$ to be extracted and the axes to be relabelled accordingly.

periments, because they allow both the QD brightness and saturation power to be monitored and routinely optimised, by aligning the QD to the collection arm (for brightness) or excitation arm (for saturation power) of our microscope.

The state of the art in QDs: The energy associated with the creation (or recombination) of an electron-hole pair in a QD depends on the occupancy of the QD, because of the Coulomb interaction. Under resonant excitation, only one electron-hole pair can occupy the QD at a time, because further electron-hole pairs require a different energy to be generated. Therefore, in this configuration, the system behaves as an effective two-level system, because other excited states (containing additional charges or electron-hole pairs) are far from resonance. Based on this principle, QDs have been shown to emit single photons, independent of the excitation intensity [107–110]. In order for these single photons to be useful for quantum

technologies, they must also be indistinguishable; this has been addressed using a variety of techniques, including spectral filtering of incoherent phonon-assisted emission [111,112], direct measurement and stabilisation of environmental noise [101,103,113–116], post selection of emitted photons [117], Purcell enhancement to shorten the radiative lifetime T_1 [118–124], and photon shaping by working in the regime where photon emission is mostly coherent [106,125,126]. The very high intrinsic brightness of QDs, combined with microstructures designed to achieve high collection efficiencies, have moved QDs clearly into the lead as a bright, deterministic source of indistinguishable single photons [127–131]. These works demonstrate the outstanding optical quality of QDs.

Experimental implementation: Having explored the general concept of resonance fluorescence, we now shift our focus to its particular application in our QD system. We wish to measure RF of optical transitions in the QD, including the X^0 , X^- and X^+ . In order to do this, we must use a laser which is resonant with the optical-frequency transition in question. The signal collected is composed of QD emission (the RF signal) and laser light which is reflected from the sample. Here, we can no longer use the spectral filtering (which was previously exploited in PL) to remove the laser background. Instead, we use a system of polarisation optics in order to ensure that we collect light of orthogonal polarisation to the laser excitation [132]. Using this method prevents us from aligning our excitation polarisation to the intrinsic polarisation of the transition which we wish to drive, because this would cause our polarisation suppression to simultaneously remove the QD signal. Because of this, the polarisation filtering removes approximately half of the QD emission, since we are prevented from aligning it with the polarisation of emission for the above reason.

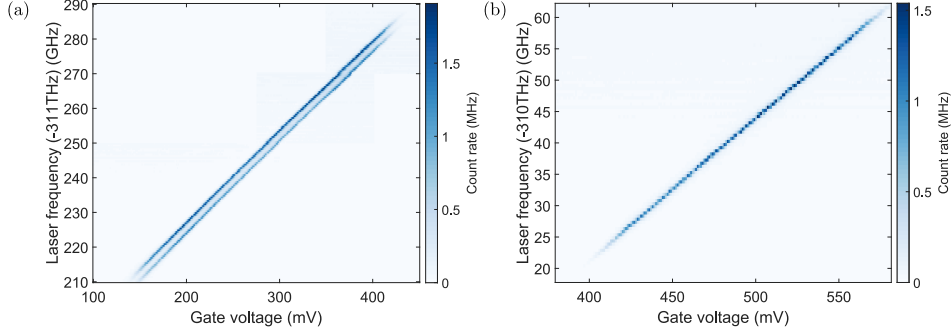


Figure 2.8: (a): Resonance fluorescence on the neutral exciton in the absence of external magnetic field. Two transitions are visible thanks to the fine structure splitting of this exciton. (b): same as (a) but for the negative exciton.

In Fig. 2.8 (a), we scan the laser frequency for a set of different gate voltages to map out the stability plateau of the neutral exciton transitions, in the absence of an external magnetic field. We work at half the saturation power of the transition in order not to power broaden or dress the states [92, 133, 134]. Using this technique we resolve the fine structure splitting of the exciton, previously invisible under PL. Performing the same procedure for the negative exciton reveals the data plotted in Fig. 2.8 (b): a single transition energy for the negative exciton. Attention should be paid to the x -axes of these two figures; the small overlap in gate voltage between the two lines (around 400mV, in this case) corresponds to the so-called “cotunnelling” region, where fast tunnelling between the two charge states takes place.

Having mapped the transitions at zero external magnetic field, we now apply a field (in Voigt geometry) and perform the same measurements. We observe a very similar response on the neutral exciton, whose splitting is now due to the combination of Zeeman effect and exchange interaction. For the negative exciton, however, the previously solitary transition splits into four

lines, separated by the electron and hole Zeeman energies (or linear combinations thereof), as shown experimentally in Fig. 2.9 (a) (and schematically in Fig. 2.3 [c]). However, the region in gate voltage over which these lines are visible is dramatically curtailed, compared to the data obtained in the absence of external magnetic field (Fig. 2.8 [b]). Indeed, we only observe RF in the cotunnelling gate region, where the electron spin is thermalised with the Fermi reservoir on a ns timescale [135, 136]. At gate voltages away from the cotunnelling region, the spin lifetime extends to several tens of μs , and no RF is measured. These observations are due to spin pumping, a very important phenomenon for all experiments which follow, and which is illustrated in Fig. 2.9 (b). A resonant laser excites population from one of the spin states to one of the excited states ($|\downarrow\rangle$ to $|\uparrow\downarrow\uparrow\rangle$) is illustrated in Fig. 2.9 (b), but any combination is possible by selecting laser frequency). From the excited state, the population can decay via either of the two radiative channels which return it to the ground state manifold; neither of these channels is preferred to the other. If the population returns to its original state, it is then re-excited by the resonant laser and the relaxation process repeats. However, if the population decays to the other spin state, the laser is no longer able to address it. In combination with a spin lifetime T_1 in the tens of μs in the centre of the plateau, this strongly quenches the QD emission. In Voigt geometry, spin pumping from the bright state to the dark state (in the illustrated case, from $|\downarrow\rangle$ to $|\uparrow\rangle$) only requires an average emission of two photons. Figure 2.9 (a) depicts RF measured in the cotunnelling region between the negative and neutral excitons; under these conditions the electron spin T_1 is reduced to around 1ns via rapid cotunnelling with the X^0 , meaning that an RF signal is recovered.

Probing spin-pumping in a time-resolved experiment reveals the signal

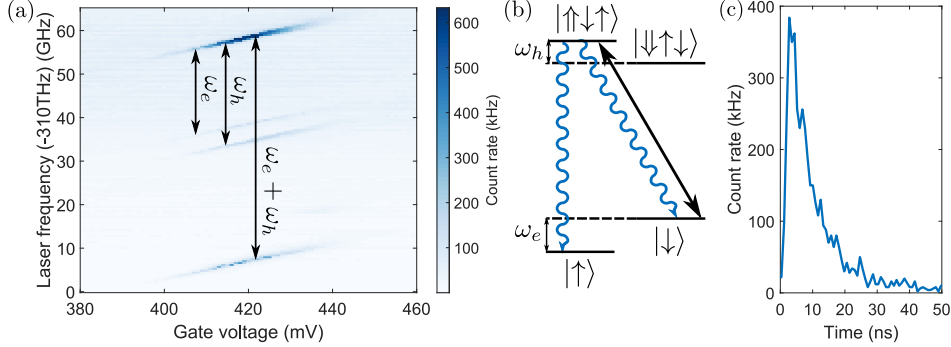


Figure 2.9: (a) Resonance fluorescence on the negative exciton measured in the cotunnelling region, under an external magnetic field of 3 T. Line splittings are determined by the electron and hole Zeeman energies, denoted ω_e and ω_h respectively. (b) Negative exciton level diagram. When driven by a resonant laser (black arrow), spontaneous decay from the excited state can proceed via two channels of equal strengths (blue wiggles). (c) Time-resolved signal obtained under driving in the configuration shown in (c), away from the cotunnelling region.

plotted in Fig. 2.9 (c). Initial fluorescence decays exponentially as the system is pumped into the dark state. Crucially, the amount of fluorescence collected is proportional to the population in the spin state under interrogation, allowing spin readout to be performed; this simultaneously initialises the spin [38, 40, 137]. This read-and-prepare process is a vital capability for quantum control. Throughout this dissertation, we use this technique to probe spin polarisation.

2.5 Quantum dot spin control

Having seen the highly coherent nature of the QD optical transitions and shown that we can read and prepare the spin of a single charge confined to a QD, we need one more capability before we can begin to exploit these spins for quantum information experiments: universal coherent control. For the purposes of the following discussion we will use the example of a single

electron, but these considerations apply equally to single holes.

At our typical external magnetic fields of a few Tesla (required for reasons discussed in Section 2.7), the electron spin states are split by a few tens of GHz (dictated by the electron g factor, which is typically close to 0.5 [138–140]). In this case, a natural approach is to drive the microwave-frequency transition resonantly using a microwave field. However, in the case of QDs, the short spin coherence of a few ns (further discussed in Section 2.7) dictates that control must be much faster than the Rabi frequencies achievable using microwaves [141–144]. In parallel, the outstanding optical interface of a QD motivates a different approach, based on ultrashort, optical pulses [138, 145–150]. This technique was demonstrated to allow full coherent control of single electron [42] and hole [151] spins in QDs, and proceeds as follows.

2.5.1 In principle

Under a magnetic field in Voigt geometry, we realise the level system shown in Fig. 2.3 (c), where the two spin-states of the QD are both linked optically to the excited state, and transitions between them can therefore be optically driven.

The state of the two-level system is described generally by [152]:

$$|\psi(t)\rangle = c_1 |\uparrow\rangle + c_2 e^{-i\omega_e t} |\downarrow\rangle \quad (2.17)$$

for two spin states $|\uparrow, \downarrow\rangle$ split in energy by $\hbar\omega_e$. We then have the density

matrix

$$\rho = \begin{bmatrix} |c_1|^2 & c_1^* c_2 e^{-i\omega_e t} \\ c_1 c_2^* e^{i\omega_e t} & |c_2|^2 \end{bmatrix} = \begin{bmatrix} \rho_{11} & \rho_{12} \\ \rho_{21} & \rho_{22} \end{bmatrix} \quad (2.18)$$

We define the Bloch vector:

$$\mathbf{R} = \begin{bmatrix} \rho_{12} + \rho_{21} \\ -i(\rho_{12} - \rho_{21}) \\ \rho_{11} - \rho_{22} \end{bmatrix} \quad (2.19)$$

In this picture, the relative population of the two states in the system is described by the z-component of the Bloch vector, whilst its x- and y-components describe the relative phase between the two states in the superposition.

The time evolution of the Bloch vector, and hence the state of the system, is defined by the level splitting $\hbar\omega_e$, which causes the x- and y-components of the Bloch vector to precess via the time dependence of ρ_{12} and ρ_{21} . Finally, we define the Rabi vector:

$$\mathbf{W} = \begin{bmatrix} \Omega \cos(\phi) \\ \Omega \sin(\phi) \\ \delta \end{bmatrix} \quad (2.20)$$

for a drive field which generates a Rabi frequency Ω , phase ϕ , and detuning δ .

In the presence of a drive field the equations of motion can be written:

$$\dot{\mathbf{R}} = \mathbf{R} \times \mathbf{W} \quad (2.21)$$

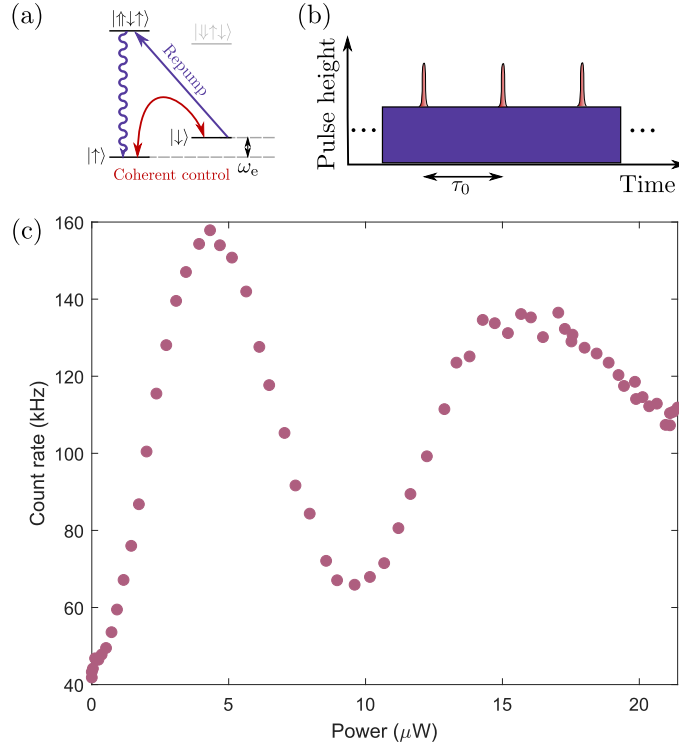


Figure 2.10: A spin Rabi rotation driven by an ultrashort pulse. (a) QD level scheme, showing action of control and repump lasers. (b) Schematic pulse sequence. The height of a train of ultrashort pulses, separated by τ_0 , is varied whilst the QD is continuously repumped. (c) Fluorescence from the readout transition is plotted as a function of average power measured at the input to the cryostat. The 40-kHz background in the absence of rotation pulses originates from the continuously-operated repump laser.

and the Bloch vector precesses around the Rabi vector with frequency $|\mathbf{W}| = \sqrt{\Omega^2 + \delta^2}$. Hence, in this manner, coherent rotations of a Bloch vector can be driven. A note on terminology: Ω is typically called the “bare Rabi frequency”, and $|\mathbf{W}|$ is normally labelled Ω' and referred to as the “grand Rabi frequency”.

2.5.2 In practice

Figure 2.10 illustrates a coherent rotation driven by an ultrashort pulse. The action of such a pulse can equivalently be considered under a Raman transition picture, or an AC Stark shift picture; we here use the latter. Due to the very high power of an ultrashort pulse, the associated Stark shift is much larger than the Zeeman energy, and we can therefore neglect the external field and consider the action of the laser pulse in the zero-field basis (c.f. Fig. 2.3 [b]). In this basis, which is equivalent to Faraday geometry, two optical transitions are allowed. Because these transitions have opposite circular polarisations, a circularly polarised pulse generates a Stark shift Ω on one of these transitions, and not the other. The large detuning Δ of the ultrashort pulse allows the excited states to be adiabatically eliminated, but a ground state AC Stark shift nevertheless remains and is given (in frequency units) by:

$$\delta(t) = \frac{1}{2}\sqrt{\Delta^2 + \Omega(t)^2} - \frac{\Delta}{2} \approx \frac{\Omega(t)^2}{4\Delta}. \quad (2.22)$$

In the previous section, we saw how to initialise the system into the $|\uparrow\rangle_x$ state, which is an eigenstate of an in-plane external magnetic field (Voigt geometry). Therefore, we consider the action of an ultrashort pulse on this initial state. The pulse arrival redefines the basis, meaning that it is convenient to recast the state as

$$|\uparrow\rangle_x = \frac{1}{\sqrt{2}}(|\uparrow\rangle_z + |\downarrow\rangle_z). \quad (2.23)$$

The AC Stark shift distinguishes the two states in this superposition, causing them to acquire a phase difference

$$\theta = \int \delta(t) dt \quad (2.24)$$

so that the state becomes

$$\frac{1}{\sqrt{2}}(|\uparrow\rangle_z + e^{i\theta} |\downarrow\rangle_z) \quad (2.25)$$

$$= \frac{1}{2}[(e^{i\theta} + 1) |\downarrow\rangle_x + (e^{i\theta} - 1) |\uparrow\rangle_x]. \quad (2.26)$$

By selecting the pulse area, which controls θ , the desired spin rotations can be performed. Experimentally this is typically done by varying the pulse power, as depicted in Fig. 2.10. Rotation around an arbitrary axis can be achieved by combining an ultrashort pulse of suitable power (giving rotation through θ around the QD growth axis) with precisely timed Larmor precession (giving rotation ϕ around the in-plane magnetic field). However, for reasons which will become obvious in the following Section, this approach is very limiting in practical terms for more complex pulse sequences.

2.5.3 Experimental setup

In order to do this, we use the setup depicted schematically in Fig. 2.11. We derive a stream of ultrashort pulses from a modelocked laser (Coherent Mira 900), which are separated temporally by a delay τ_0 . We split this stream into two halves using a 50:50 beamsplitter. One of these streams travels along a path length which can be tuned by physically moving the position z of a retroreflector (the “moving arm”). On recombination with the other stream (which traverses the “static arm”), the two pulse trains

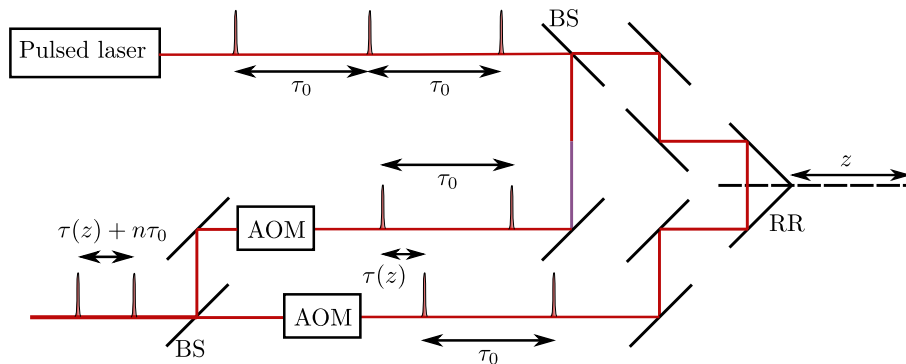


Figure 2.11: Schematic depiction of pulse sequence construction apparatus. A mod-locked laser produces pulses with a fixed repetition time of τ_0 . BS denotes a 50:50 beamsplitter, RR a retroreflector, and other solid black lines are mirrors. The retroreflector position z tunes the relative delay between the two arms, $\tau(z)$. The final delay is $\tau(z) + n\tau_0$ for integer n , depending on pulse selection from the two arms, which is done using the AOMs.

will be offset by a delay τ which depends on z . By using acousto-optic modulators (AOMs) to select pulses from the trains and by tuning z , an arbitrary delay (of $\tau(z) + n\tau_0$) between two pulses can be selected, provided that $\tau(z)$ can range from zero to $\tau_0/2$. Some multi-pulse sequences, including Hahn echo [153] and simple dynamical decoupling sequences [154, 155], are also possible using this technique [156, 157].

Using this approach, spin π -rotation fidelities of 89% and 91% have been reported for the hole and electron spin, respectively [42, 157]. These can be improved further by using compound pulses consisting of two closely spaced $\frac{\pi}{2}$ pulses. This removes the detrimental effect of spin precession during the rotation pulse, allowing electron spin rotation fidelities of 98% to be achieved [49].

2.6 Nuclear spin interactions

A QD based on III-V materials is set apart from many other systems by the nature of its hyperfine interaction, giving near-homogeneous coupling between a QD spin and its environment of nuclear spins to realise the central spin system [158–160]. The mesoscopic ensemble of nuclear spins is attractive to study because nuclear spins have very long coherence times [161], and the unique homogeneity of electro-nuclear coupling means that the QD spin fundamentally couples to an ensemble, rather than individual nuclear spins. However, we first discuss their effect on the QD bound states, which is greatly enhanced by the concentration of the wavefunction over the $\sim 10^5$ lattice sites. This mesoscopic scale is too small to be cancelled by averaging and nuclear spin interactions are a crucial consideration for all following experiments [162].

2.6.1 Physical origin

The Fermi contact interaction: Because of its contact nature, this term applies only to spins in s-shell orbitals; it is relevant for electrons but not for heavy holes. The Hamiltonian for this term takes the form [163–165]:

$$\hat{H}_{fc} = \sum_j A^j (\hat{I}_z^j \hat{S}_z + \frac{1}{2} [\hat{I}_+^j \hat{S}_- + \hat{I}_-^j \hat{S}_+]) \quad (2.27)$$

Here, j indexes nuclear site, \hat{I}^j refers to the spin of the j -th nucleus in the QD, and \hat{S} denotes the electron spin. A^j denotes the hyperfine coupling constant per nucleus, and varies to account for different nuclear species and the inhomogeneous distribution of the electron wavefunction. The total

hyperfine constant $A_j \times N$ is ~ 10 GHz for In, Ga, and As [163, 166].

The first term in the above expression alters the electron spin precession frequency around a given quantisation axis (denoted by z). We can consider this interaction in a semiclassical picture where the electron spin sees a mean field arising from an average nuclear polarisation $\langle I_z \rangle$. This mean field, which is typically termed the Overhauser field [167], can then be expressed [163]:

$$B_{\text{OH}} = \frac{\sum_j A_j \langle I_j \rangle}{g_e \mu_B} \quad (2.28)$$

At full polarisation, the Overhauser field constitutes an effective magnetic field of several Tesla [168], which is comparable to the magnetic field we can apply externally.

Whilst we operate our experiments at a temperature of 4K and under a magnetic field of a few Tesla, these conditions are insufficient to polarise the nuclei; at thermal equilibrium, the nuclear spins are unpolarised. Because the Overhauser field can be so large, the distribution of the nuclear state is crucial for determining the coherence of a confined spin. This is discussed further in Sections 2.6 and 2.7.

The final two terms in \hat{H}_{fc} enable electro-nuclear flip-flops. In practice, since we operate experiments under external fields of a few Tesla, these interactions are strongly suppressed due to the mismatch in Zeeman energies between the electron (~ 7 GHz T⁻¹ [163]) and the nuclei (7 – 13 MHz T⁻¹ [156]).

The dipolar interaction: For the heavy hole, the dominant interaction

is based on dipole-dipole coupling and takes the form [163, 169]:

$$\hat{H}_{dd} = \sum_k \frac{A_k^h}{1 + \beta^2} (\hat{I}_z^k \hat{S}_z^h + \frac{\alpha}{2} [\hat{I}_+^j \hat{S}_-^h + \hat{I}_-^j \hat{S}_+^h]) \quad (2.29)$$

β denotes the heavy hole-light hole mixing, \hat{S}^h is the pseudospin operator for heavy holes, and $\alpha = \frac{2\beta}{\sqrt{3}}$. This interaction, in contrast to the Fermi contact hyperfine interaction, is anisotropic (when $\alpha \neq 1$), meaning that the hole pseudospin has different sensitivities to Overhauser fluctuations in different directions. Secondly, the hole pseudospin hyperfine constants are about an order of magnitude weaker than those for the electron spin [169, 170], with corresponding consequences for hole pseudospin coherence; these will be discussed further in Section 2.7.

The noncollinear hyperfine interaction: The inhomogeneous strain of the QD, present due to the self-assembly growth method, induces electric field gradients which couple to the quadrupolar moments of the nuclei. This coupling tilts the quantisation axis for the nuclei away from the direction of the applied magnetic field. The Hamiltonian which describes the nuclear quadrupolar interaction can be written [163, 171–173]:

$$\hat{H}_Q = \sum_j B_Q^j \left[(\hat{I}_x^j)^2 \sin^2 \theta^j + \frac{1}{2} (\hat{I}_x^j \hat{I}_z^j + \hat{I}_z^j \hat{I}_x^j) \sin 2\theta^j + (\hat{I}_z^j)^2 \cos^2 \theta^j \right] \quad (2.30)$$

Here, we sum over the nuclear lattice sites j , each of which has a quadrupolar coupling strength B_Q , and an angle θ between the quadrupolar axis and the magnetic field.

Extracting the part of this Hamiltonian which is entirely off-diagonal in the nuclear Zeeman eigenbasis, and then performing a Schrieffer-Wolff transformation [174, 175] to result in the appropriate corrections to the Hamilto-

nian, we arrive at [171, 176]:

$$\hat{V}'_Q = -\hat{S}_z \sum_j \frac{A^j B_Q^j}{\omega_z^n} \left\{ [(\hat{I}_x^j)^2 - (\hat{I}_y^j)^2] \sin^2 \theta^j + [\hat{I}_x^j \hat{I}_z^j + \hat{I}_z^j \hat{I}_x^j] \sin 2\theta^j \right\}. \quad (2.31)$$

A^j is again the hyperfine constant per nucleus, and ω_z^n is the nuclear Zeeman energy. This perturbation to the hyperfine Hamiltonian allows a collective interaction between the electron and nuclear spins. This interaction can alter I_z by 1 unit ($\hat{I}_x \hat{I}_z$ or $\hat{I}_z \hat{I}_x$) or 2 units (\hat{I}_x^2 or \hat{I}_y^2) units, without flipping the electron spin. These therefore correspond to low-energy excitations, in the sense that for them to occur, an energy gap of only a few tens of MHz (the nuclear Zeeman energy) must be bridged. The noncollinear interaction has been reported to closely match experimental observations of the electro-nuclear dynamics [177, 178]; many of the exciting and interesting consequences of this Hamiltonian will be discussed in later sections of this dissertation.

2.6.2 Nuclear spin feedback

The nature of the interaction between bound states and nuclear spins is bidirectional: nuclear spin flips are enabled by the presence of a confined spin, and the nuclear spin state affects the confined spin via the hyperfine interaction. Together, these effects result in feedback between the bound state and nuclear spins. This effect is discussed below using the example of the neutral exciton transition.

We previously introduced the neutral exciton manifold under an external field as three states: the crystal ground state, and two optically excited

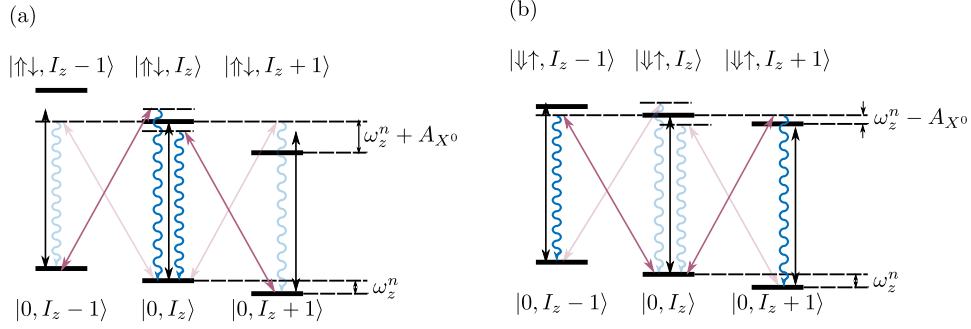


Figure 2.12: Adapted from [178]. The neutral exciton blue (red) branch (a, [b]), dressed with nuclear state parametrised by average polarisation. $|0\rangle$ denotes crystal ground state. The carrier transition is driven by a laser which is resonant when at a polarisation of I_z (black arrow). This laser can also drive diagonal, nuclear spin-flipping transitions (pink arrows), which combine with spontaneous emission (blue wiggles) to alter the nuclear spin state. Due to the resonance condition and the ladder anharmonicity, these can be relatively stronger (more opaque) or weaker (more transparent), depending on direction of change of I_z and the type of anharmonicity.

states consisting of an electron-hole pair aligned or anti-aligned with the field. We now dress the reduced manifold, formed by the ground state and the blue excited state, with the nuclear spin state characterised by its spin projection I_z . This is illustrated in Fig. 2.12 (a). The ground state manifold is split simply by the nuclear Zeeman energy ω_z^n . In the excited state manifold, an additional shift due to the hyperfine interaction between the nuclear spins and the spin of the electron-hole pair leads to a splitting of $\omega_z^n + A_{X0}$. This results in an anharmonic ladder of states. Within this ladder, in addition to the principal vertical transitions, diagonal processes are weakly allowed by the noncollinear interaction captured by Eq. 2.31. We now drive the neutral exciton transition resonantly and consider the effect of a fluctuation in I_z , increasing it to $I_z + 1$. This causes our laser to no longer be strictly resonant with the resulting neutral exciton transition, which is shifted by A_{X0} . The anharmonicity of the ladder means that the laser frequency is closer to resonance with the diagonal transition which

reduces I_z by one unit than it is to the vertical X^0 transition. The effect is reversed for fluctuations which reduce I_z . In this way, the polarisation of the nuclear spins is stabilised around a value which causes a drive laser to be resonant with the X^0 transition. If a laser is spectrally swept through this X^0 resonance, we observe a broad, flat-top resonance profile as I_z is driven to retain the resonance condition; the nuclear spin state is “dragged”.

Very similarly, if instead selecting the red excited state (Fig. 2.12 [b]), we arrive at a ladder of states of the opposite anharmonicity, and a feedback which has the opposite directionality: I_z is de-stabilised such that the nuclear spin state is driven away from resonance. This effect is termed “anti-dragging” accordingly.

Whilst the neutral exciton has been used as an illustration, these feedback effects exist for all types of bound state discussed in this work. We will revisit them in Section 3.9 in the context of the positive trion, and we will discuss feedback effects in the negative exciton system at length in Section 4.4 and throughout Chapter 5.

2.7 Spin coherence

To exploit a QD as a qubit, the negative and positive trions are natural choices thanks to their two-level ground (spin) states. We previously developed a general expression involving the coherence between two levels, shown in Eq. 2.14. Here, we apply that relationship to the two-level spin states of X^- (which are $|\uparrow\rangle, |\downarrow\rangle$) or X^+ (which are $|\uparrow\rangle, |\downarrow\rangle$). For this purpose, we will characterise the dynamics of the qubit using three timescales.

The first, known as the lifetime (T_1), refers to the timescale of population decay from the upper level to the lower. In the context of this discussion,

this refers to the timescale for a polarised spin to be thermalised (i.e. randomised). A QD spin lifetime can reach the ms regime [179]; when operating in the centre of the X^- or X^+ plateau, we typically measure a T_1 of tens of μs in our samples. This is a property of the sample heterostructure design, itself a compromise between the need for long lifetimes in the centre of the plateau for spin control, and short cotunnelling times to allow mapping of the QD resonances in the cotunnelling regime. Equation 2.14 illustrates the limit to coherence imposed by relaxation; T_1 on the scale of tens of μs is well suited to our system because the lifetime limit on coherence ($T_2 = 2T_1$) is roughly three times longer than other decoherence processes. For this reason, T_1 will not be considered further in this section.

The remaining two timescales for spin dynamics are known as the homogeneous and inhomogeneous dephasing times, denoted T_2 and T_2^* , respectively. It turns out that interactions with the surrounding nuclear spin ensemble dictate spin coherence [156, 157, 162, 180–182]. Here, we outline the physical principles behind these mechanisms.

The hyperfine interaction between the spin and surrounding nuclei can be described as an effective magnetic field on the confined spin, termed the Overhauser field [167]. The precession frequency of a confined spin is dictated by the sum effect of the external magnetic field and this Overhauser field. The nuclear spins have a complex spectral distribution containing broad low-frequency components, as well as contributions at higher frequencies (of order 10 MHz T^{-1}). This distribution is inherited by the precession frequency of a confined spin, via the Overhauser shift, causing a loss of phase information: the spin dephases.

Applying an external magnetic field suppresses the effect of these fluctuations. Considering the total field:

$$B_{tot} \equiv |\mathbf{B}_{tot}| = \sqrt{(B_{ext} + B_{OH}^{\parallel})^2 + (B_{OH}^{\perp})^2} \quad (2.32)$$

We then examine the limit of $|\mathbf{B}_{ext}| \gg |\mathbf{B}_{OH}|$, leading us to:

$$B_{tot} \approx B_{ext} + B_{OH}^{\parallel} + \frac{(B_{OH}^{\perp})^2}{2B_{ext}} \quad (2.33)$$

In this way we arrive at the result that the Overhauser field fluctuations along the direction of the external field remain linear and unsuppressed, whilst those perpendicular to the external field are suppressed by a factor $B_{OH}^{\perp}/2B_{ext} \sim 100$.

These fluctuations, and their effect on spin coherence, can be measured using Ramsey interferometry [183]. In this scheme, the spin is initialised into a superposition state $\frac{1}{\sqrt{2}}(|\uparrow\rangle + |\downarrow\rangle)$ using an initial $\pi/2$ rotation pulse. It is then allowed to undergo free precession for a time τ , during which it evolves to $\frac{1}{\sqrt{2}}(|\uparrow\rangle + e^{-i\omega t} |\downarrow\rangle)$, where ω is the sum of the Larmor frequency and the Overhauser shift. A second $\pi/2$ rotation pulse, followed by a readout, allows us to measure the spin precession, an example of which is presented in Fig. 2.13. We observe a decay envelope corresponding to the inhomogeneous dephasing time T_2^* , which is dictated by quasi-static Overhauser noise (which are the dominant noise terms in B_{OH}^{\parallel}) [156]. This noise is effectively frozen during each Ramsey experiment (a few hundred nanoseconds) but changes from run to run (on the timescale of a few milliseconds [184]), meaning that when we integrate over $\mathcal{O}(10^6)$ experimental cycles, we average over free precession at many different frequencies, giving the observed decay envelope.

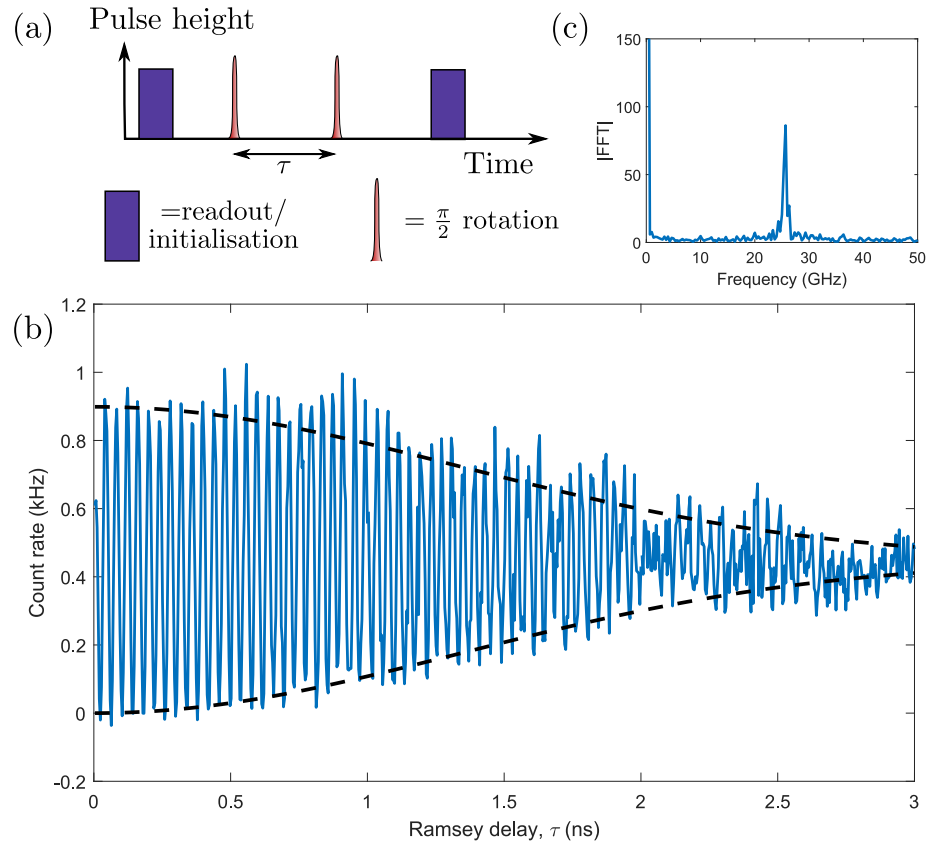


Figure 2.13: Ramsey interferometry of a QD electron spin. (a) Pulse sequence schematic. The electron spin evolves for a time τ between two $\pi/2$ pulses, before being read. (b) Readout signal as a function of τ (blue curve). The oscillation visibility decays according to a fitted Gaussian envelope (black dashed curves) yielding a T_2^* of 1.90(9) ns. (c) Fast Fourier Transform of the data in (b) illustrates the Larmor precession frequency, which is fitted as 25.402(5) GHz.

Because the precession frequency inherits the noise distribution, the decay profile is simply related to the Overhauser noise distribution by a Fourier transform; in the case of this type of T_2^* measurement, the profile is Gaussian, testifying to the quasi-static nature of the dominant noise [162]. In QDs, typical measurements observe electron spin T_2^* around 1–3 ns [156, 185–190] and hole pseudospin T_2^* around 30–40 ns [151, 157, 191, 192]. In both cases, nuclear spins constitute the principal limitation; hole pseudospins are less severely affected because the hyperfine interaction is ~ 10 times weaker than for the electron. However, hole pseudospins also couple to electrical noise, which presents an additional barrier to achieving long-lived coherence [157].

The decoherence effect of a quasi-static noise source can be efficiently removed using pulse sequences, a technique known as decoupling [193–196]. This technique can take many forms; the simplest is known as Hahn echo [153]. This sequence (depicted schematically in Fig. 2.14 [a]) is very similar to the above Ramsey sequence, with the addition of a π rotation pulse after the spin has evolved for $\tau/2$. This pulse reverses the sign of phase acquisition during the second half of the free evolution period, which cancels shifts which are static during τ . This causes a coherence echo after a full τ of evolution, whose visibility can then be probed by varying the position of the π pulse over one Larmor period. This reveals a decay profile with a characteristic timescale given by the homogeneous dephasing time, known as T_2 .

For electron spins, T_2 can be extended by increasing the external magnetic field to suppress fluctuations in B_{OH}^\perp . A non-trivial dependence on magnetic field is observed, arising from the interplay of quadrupolar effects, the Zeeman effect, and the hyperfine interaction [156]. When the external magnetic field is sufficient to allow quadrupolar effects to be neglected, an exponential decay in coherence is observed, with a coherence time T_2 typi-

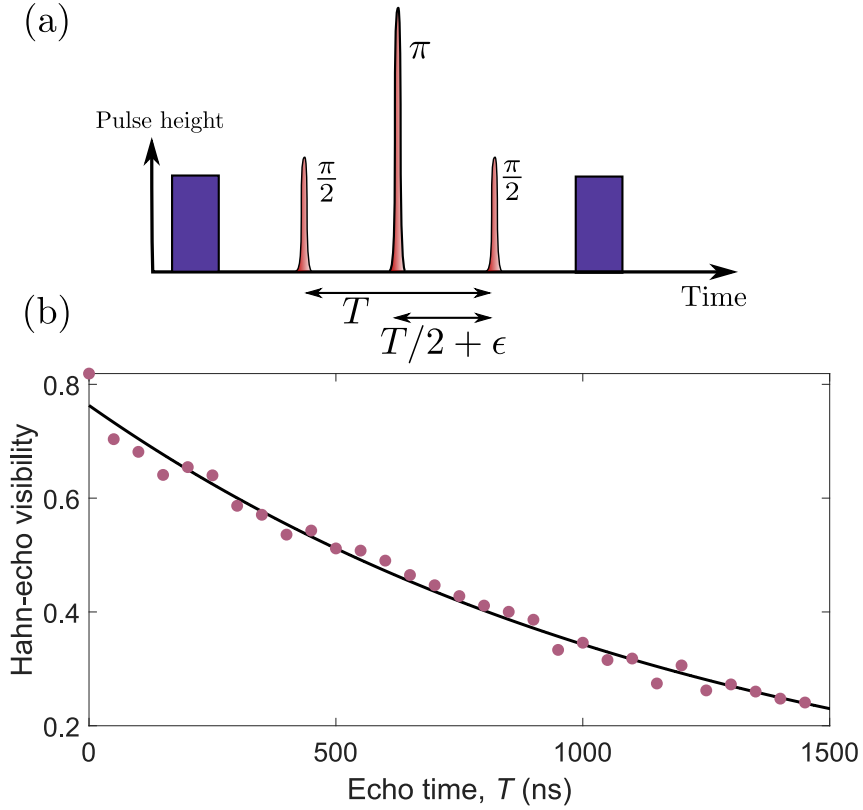


Figure 2.14: (a) Hahn-echo pulse sequence schematic. (b) Hahn echo of an electron spin, at 3.5 T. Visibility is measured as a function of Hahn-echo time T (pink circles). An exponential fit (black curve) reveals $T_2 = 1250(30)$ ns.

cally of a few μs under our usual conditions of 3-4 Tesla; we plot an example measurement in Fig. 2.14. This envelope is driven by nuclear noise which is much faster than the timescale of the experiment [156].

In addition to filtering quasi-static noise, the Hahn-echo sequence operating for a total time τ removes noise which evolves at frequencies satisfying $\omega = \frac{(2n+1)\pi}{\tau}$ for integer n . In contrast, noise at frequencies $\omega = \frac{2n\pi}{\tau}$ is enhanced. As is evident from Eq. 2.31, the noncollinear interaction renders the electron spin splitting sensitive to transverse components of the nuclear polarisation. This means that there exist characteristic frequencies

in the nuclear noise spectrum corresponding to the nuclear Zeeman energies, causing dramatic drops and revivals in electron spin coherence in a Hahn-echo measurement [197]. At Hahn-echo delays commensurate with a nuclear Zeeman frequency, noise at these frequencies is amplified and coherence sharply reduced [156]. In this way, the Hahn-echo sequence (and decoupling sequences in general) act as sophisticated probes of the nuclear noise spectrum [198, 199]. As the magnetic field is increased, coupling to nuclear noise is suppressed as the Zeeman interaction dominates the nuclear dynamics, reducing the strength of noncollinear coupling. This is the reason that drops and revivals are not visible in Fig. 2.14.

For hole pseudospins, a similar increase in T_2 is observed on increasing the external field, up to ~ 5 Tesla. Beyond this, electrical noise from the sample structure becomes dominant and the coherence begins to decrease again. This electrical noise causes fluctuations in the average position of the hole within the QD, and the inhomogeneous strain alters the mixing between heavy- and light-hole states, modifying the effective hole g factor. This effect becomes worse at large B-fields since the decoherence stems from fluctuations in the level splitting, which is linear in magnetic field for Zeeman levels. In our samples, there exists a coherence optimum at around 4T [157].

For the above reasons, the Hahn-echo sequence can be pictured as a periodic notch filter in frequency space, allowing certain frequencies to pass and removing others [193, 196, 200–203]. Other dynamical decoupling sequences can also be pictured in this way. Beyond, if the noise spectrum is known, the ideal decoupling sequence can even be reverse-engineered by designing the desired filter function [204–206].

2.8 Summary

At this point, we conclude our whistle-stop tour of the past few decades of experimental and theoretical efforts in the study of InGaAs quantum dots with a summary of key achievements and outstanding challenges.

Firstly, coherent control of single spins confined to QDs has been achieved using ultrafast optical pulses, allowing complete quantum control over both confined electrons [42] and holes [151]. This technique has driven the study of QD spin physics to great sophistication, yielding important insights into spin coherence [156, 157]. However, this sophistication has been reached within the tight limits imposed by the impracticality of spin control using ultrafast pulses, which leaves many spin control protocols out of reach.

Secondly, nuclear spins in QDs have been extensively probed using a variety of techniques, shedding much light on the physics which governs their behaviour [163]. However, work to-date has largely addressed the nuclei as an obstacle to be navigated, rather than as a resource to be exploited.

This dissertation is intended to move smoothly through these challenges. In Chapter 3, we develop a new optical technique for performing QD spin control, applied to a single hole. We demonstrate the high fidelity and arbitrary flexibility of our technique, which allows us to construct pulse sequences at will, designed electronically and delivered via imprinting a microwave signal onto laser light.

In Chapter 4 we apply the same technique to the control of a single electron spin. In order to do this, we must cool the nuclear spin environment, which enhances the electron spin coherence time by an order of magnitude. With this in place, we demonstrate the highest π -rotation fidelities reported in this system. From there, we use our spin control technique to show

deterministic coupling - via Hartmann-Hahn resonances - and decoupling - via spin locking - of the electron spin from its nuclear spin environment.

In Chapter 5, we turn our attention to the nuclear spins of the QD. Using the control technique developed in Chapter 3 and the nuclear resonances uncovered in Chapter 4, we reveal single collective spin excitations of the nuclear ensemble. By measuring the interaction frequency with these collective excitations, we can probe correlations in the nuclear ensemble. Using this novel technique, we witness entanglement in the form of quantum coherences akin to a dark many-body state.

Finally, in Chapter 6, we characterise the next generation of QD samples: a lattice-matched system based on GaAs QDs embedded in an AlGaAs matrix. We reveal high optical quality and long spin lifetime, allowing us to perform the first coherent control of an electron spin in this type of QD. Beyond, the highly homogeneous nuclear environment of these QDs, which we probe using Hahn-echo spectroscopy, places useful quantum technological applications firmly within reach [207].

Chapter 3

Flexible Control of a Spin in a Quantum Dot

Exploiting the attractive properties of a QD spin requires mastery of its quantum state. Whilst the current state of the art is in principle complete, it is in practice found wanting on several fronts. In this Chapter we implement a new approach to QD spin control, based on a driven Raman process. We first show that we can perform coherent rotations of a hole pseudospin using a two-colour Raman laser pulse. We then demonstrate that the technique is complete, both in principle and in practice, and benchmark the fidelity of our pseudospin rotations.

A brief note on terminology: the heavy hole studied in this Chapter carries a pseudospin, which can be $+3/2$ or $-3/2$. For the sake of simplicity, we refer to it simply as a spin throughout the Chapter.

The following experiments were carried out with Rob Stockill.

3.1 Background

We have seen that complete control of a QD spin is not an outstanding challenge [41, 42, 151]. Over a decade ago, ultrashort optical pulses were utilised to demonstrate full qubit manipulation, by combining single-axis rotations with precisely timed Larmor precession in order to reach an arbitrary point on the Bloch sphere. Because these ultrashort pulses are derived from a modelocked laser, they are generated with a fixed repetition time which is intrinsic to the source. In order to generate sequences where pulses are separated by arbitrary delays, such as a Ramsey interferometry sequence, we employ the setup previously depicted in Fig. 2.11. The pulse stream is split into two arms by a beamsplitter, termed the static and delay arms. In the delay arm, a variable path length allows the timing of pulses to be tuned relative to the static arm. When re-combined on a second beamsplitter, the two arms result in a stream of pairs of pulses separated from adjacent pairs by the laser repetition time, and within each pair by a delay (which is the delay between the static and moving arms) which can be precisely controlled. Because this delay relies on path length, it cannot be tuned on the timescale of a pulse sequence, meaning that the resulting control protocol is constrained to contain two different delays at most. This renders a plethora of desirable pulse sequences, such as most composite control sequences designed to enhance gate fidelities [208], and many types of dynamical decoupling sequence [209], impractical.

In terms of flexibility, the ideal method of spin manipulation would be to directly drive the magnetic dipole transition which connects the spin ground states, via a single-photon process involving a tens-of-GHz (microwave) field. This has been exploited for control in other systems, notably electrically de-

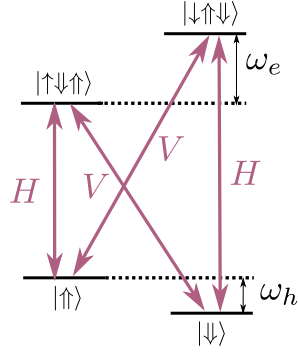


Figure 3.1: X^+ level diagram in Voigt geometry. Pink arrows are optical transitions, of linear polarisation H or V . $\omega_e(\omega_h)$ denotes the electron (hole) Zeeman energy.

finer QDs [141–144]. There, the combination of longer electron spin coherence time (tens of ns vs. a few ns [210]) and lower ESR frequencies (hundreds of MHz vs. tens of GHz [141]) when compared to self-assembled QDs facilitated the implementation of magnetic spin resonance. In our self-assembled QDs, the requirement to generate Rabi frequencies of the order of the ESR width (hundreds of MHz) using microwave fields resonant with the ESR (tens of GHz) presents severe technical challenges. For high fidelity operations, spin rotations must be completed well within the spin coherence time, which in our system places a stringent minimum on rotation speed.

For these reasons, the work of this Chapter addresses the outstanding problem of achieving arbitrary spin manipulation. At this point, we have a choice of qubit: an electron spin, or a hole spin. Here, we choose to work with the hole spin because its order-of-magnitude weaker coupling to the environment of nuclear spins makes it a cleaner platform, with easier access to the ideal spin dynamics. Quantitatively speaking, coherence stored in a hole spin will live for an order of magnitude longer than in an electron spin [156, 157, 211–213], placing a less stringent minimum on the speed of our spin control. Many important control capabilities have been demonstrated

already using holes confined to QDs, including state preparation [39, 40], ultrafast manipulation [151], and spin-spin entanglement generation [50]. Figure 3.1 depicts the relevant energy levels and allowed transitions in this basis, all of which are at optical frequency. We note that the ground states form two Λ systems of allowed transitions with the excited states.

3.2 Spin control in the rotating frame

Our approach is based on driving a Raman transition between the two ground states [214–219], for which we require an optical field composed of two colours, phase coherent with each other. Whilst such a field could be derived in a number of ways, we choose to use the technique depicted in Fig. 3.2. We modulate an optical-frequency, continuous-wave laser with a sinusoidal microwave-frequency signal, splitting the output into two sidebands separated by twice the modulation frequency. In addition, any phase offset $\Delta\phi_{\mu w}$ in the microwave signal causes the two generated sidebands to have a phase offset $2\Delta\phi_{\mu w}$ relative to each other. This technique allows us to marry the speed and fidelity of optical control with the versatility of magnetic spin resonance, because the effective drive inherits the properties of the microwave field. Crucially, since our drive now consists of two components with a frequency difference, our effective drive acquires phase at this frequency difference and so we can now picture our spin in the rotating frame. In other words, our drive is near resonant with our spin. We can therefore recast Eq. 2.17 in this picture:

$$|\psi\rangle = c_1 e^{i\delta t/2} |\uparrow\rangle + c_2 e^{-i\delta t/2} |\downarrow\rangle \quad (3.1)$$

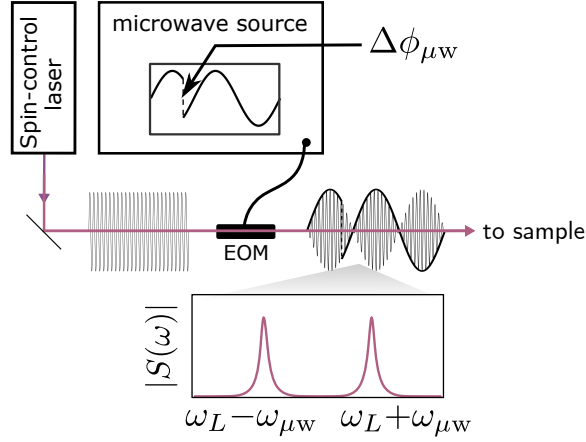


Figure 3.2: Microwave modulation schematic. A continuous-wave spin-control laser (at frequency ω_L) is modulated by a microwave-frequency signal with controllable frequency $\omega_{\mu w}$ and phase $\phi_{\mu w}$, using an electro-optic modulator (EOM). The resulting signal is composed of two sidebands, separated spectrally by $2\omega_{\mu w}$.

which leads to the density matrix:

$$\rho = \begin{bmatrix} |c_1|^2 & c_1^* c_2 e^{-i\delta t} \\ c_1 c_2^* e^{i\delta t} & |c_2|^2 \end{bmatrix} = \begin{bmatrix} \rho_{11} & \rho_{12} \\ \rho_{21} & \rho_{22} \end{bmatrix} \quad (3.2)$$

where δ refers to the effective detuning of the process, corresponding to the two-photon detuning in the case of a two-photon process such as this. We have made the rotating-wave approximation, assuming that δ is small compared to Ω .

Our Bloch vector then becomes:

$$\mathbf{R} = \begin{bmatrix} \rho_{12} + \rho_{21} \\ -i(\rho_{12} - \rho_{21}) \\ \rho_{11} - \rho_{22} \end{bmatrix} \quad (3.3)$$

As defined in Eq. 2.20, the Rabi vector is:

$$\mathbf{W} = \begin{bmatrix} \Omega \cos(\phi) \\ \Omega \sin(\phi) \\ \delta \end{bmatrix} \quad (3.4)$$

for a system in the presence of a drive field with detuning δ and Rabi frequency Ω , with phase ϕ relative to the system.

The equations of motion then reduce to:

$$\dot{\mathbf{R}} = \mathbf{R} \times \mathbf{W} \quad (3.5)$$

and described geometrically, the Bloch vector precesses around the Rabi vector at the so-called “grand Rabi frequency” $\Omega' = \sqrt{\Omega^2 + \delta^2}$. Using this technique, we have full SU(2) control over the Rabi vector itself via the optical power (which controls Ω), the microwave frequency (which controls δ), and the microwave phase (which controls ϕ).

We can make some important observations at this stage. As became obvious already in Eq. 3.1, in this reference frame, which is defined by the phase acquisition of our effective drive, spin precession is observed only when there exists a two-photon detuning in the system i.e. when $\delta \neq 0$. When interrogated resonantly using this technique, the phase of the drive exactly follows the Larmor precession of the spin, and the Bloch vector will not be observed to precess around the magnetic field. The phase of the Rabi vector relative to the Bloch vector, which defines the trajectory of the Bloch vector on the Bloch sphere, is itself defined by the microwave modulation field, which controls ϕ directly. The effective drive has inherited the versatility of the microwave field.

As can be seen in Fig. 3.1, the ground-state manifold forms two Λ -systems with the optically excited states. We must ensure that these two paths interfere constructively, which amounts to selecting circular polarisation. In this configuration, all four transitions are driven with equal strength, and we expect a Rabi frequency given by $\Omega = \Omega_L^2/\Delta$ where Ω_L is the Rabi frequency of the Raman laser on the optical transitions.

In writing Eq. 3.1 we neglected the optically excited states in our treatment. This is justified in the following way. During the process, the excited state population can be at most:

$$\rho_{ee} = \frac{\Omega_L^2}{\Omega_L^2 + \Delta^2}. \quad (3.6)$$

We can recast this expression in terms of our spin Rabi frequency Ω as:

$$\rho_{ee} = \frac{\Omega}{\Omega + \Delta}. \quad (3.7)$$

Provided we remain in the limit $\Delta \gg \Omega$, the excited states can be safely neglected.

3.3 Experimental setup

We apply this technique to our sample in Voigt geometry by passing a continuous-wave laser (Toptica DL Pro) through an amplitude electro-optic modulator (EOM) (EOSpace, Ultra-High Extinction Ratio, 20-GHz bandwidth). This EOM is controlled by the output of a switch (Mini Circuits), into which we send a continuous-wave, microwave-frequency sinusoidal signal from a signal generator (Rohde&Schwarz SMF100A), alongside a pulse sequence from a delay generator (SRS DG645) which also functions as the

clock for our experiment. Further details about the microwave system are given in Appendix A. A second laser (Toptica TA Pro), resonant with one of the transitions to an excited trion state, performs readout of our spin state as well as performing the initialisation for the next cycle [38, 40]. This is depicted in Fig. 3.3 (a). Finally, as previously described, we must drive the neutral exciton transition with a third laser (New Focus Velocity Tunable Diode Laser) in order to populate our n-doped QD sample with a hole.

3.4 Driven spin-Rabi oscillations

The first step towards demonstrating full coherent control of a qubit is to drive Rabi oscillations between the two qubit states. To this end, we drive the system with a pulse of variable length and detuning. In practice, as shown in Fig. 3.3 (b), a driving pulse of length T is paired with a complementary pulse of length $T_0 - T$, such that the total drive time is constant and the power can be stabilised. The sideband drive laser provides the vast majority of the input power and so is the only relevant laser for power stabilisation. Each region of sideband drive is followed by a readout-preparation pulse, and we measure the fluorescence during this pulse as our signal.

We show our experimental data in Fig. 3.3 (c), which demonstrates coherent Rabi oscillations of a single QD-confined hole spin using a Raman drive. We take the Fourier transform of these Rabi oscillations in Fig. 3.3 (d). We observe good quantitative agreement with the expected functional form of our Rabi frequency: $\sqrt{\Omega^2 + \delta^2}$, where Ω is the resonant Rabi frequency and δ is the two-photon detuning [152]. Additionally, we plot the visibility of our oscillations in Fig. 3.3 (e), again observing good quantitative agreement with the expected functional form: $\frac{\Omega^2}{\Omega^2 + \delta^2}$ [152].

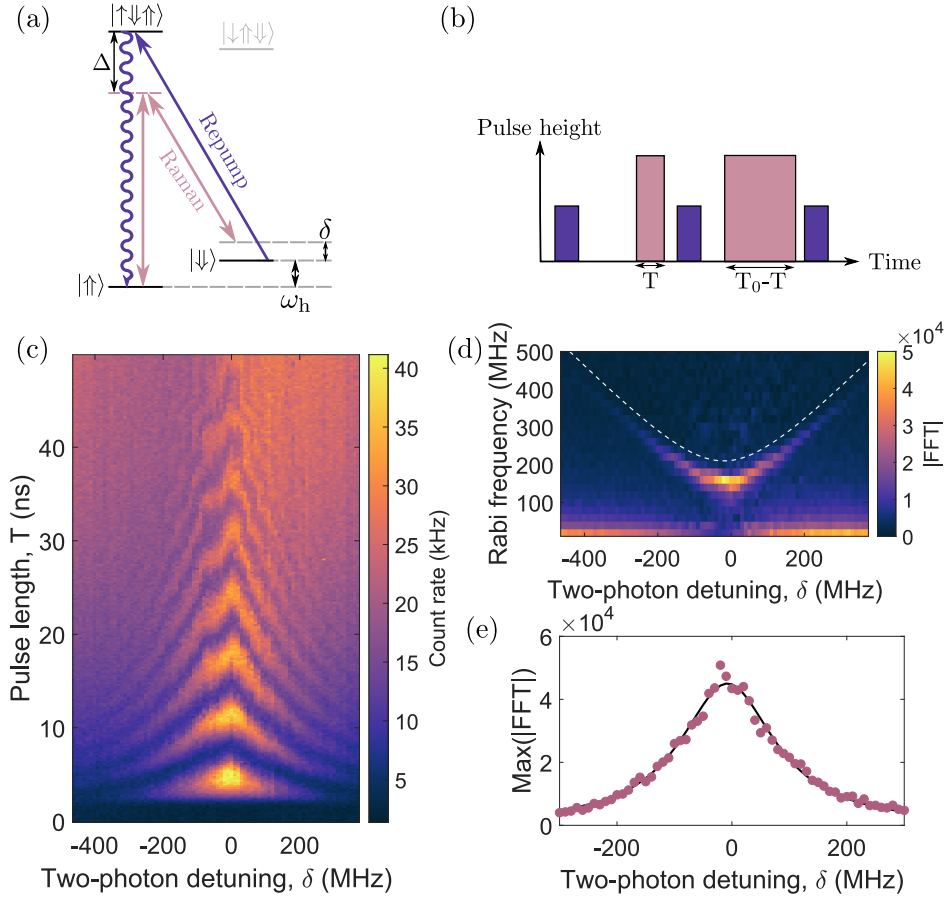


Figure 3.3: (a) Level diagram with lasers and decay channels. Transitions between the ground spin states are driven by two Raman fields (pink), detuned by Δ from the excited states and with a two-photon detuning δ from the spin resonance ω_h . We use a second laser (purple arrow) to pump population from $|\downarrow\rangle$ to the excited state, from which it decays (purple wiggles), allowing us to perform readout and preparation. (b) Rabi pulse sequence. Drive pulses are paired to conserve total pulse area. Readout pulses follow each control operation. (c) Count rate as a function of preceding drive pulse length and two-photon detuning. (d) FFT of data in (c). The white dashed line has the functional form $\sqrt{\Omega^2 + \delta^2}$ and is offset for clarity. (e) The maximum value of the data in (d) (pink data points), along with a Lorentzian fit (black curve).

In addition to these observations, our data show departures from the behaviour of an ideal two-level system. Some of these are technical: we observe a universal darkness of the system for drive times less than ~ 2 ns, due to the finite response time of our switch. Others are physical: we observe a systematic difference in long-time brightness between positive (brighter) and negative (dimmer) detunings, as well as a departure from the ideal expected frequency for small negative detunings $\delta \sim -20$ MHz. Of course, we do not expect to observe the behaviour of an ideal two-level system since this is not an accurate description of our system. These observations are likely a result of the interaction between the hole spin and its environment of nuclear spins, one consequence of which is a hole-spin-polarisation-dependent feedback on the nuclei. We will return to a much more thorough study of our QD system, including the interaction between a confined spin and the surrounding nuclear spins, in Chapters 4 & 5. For now, we continue to investigate the hole spin using our Raman control technique.

3.5 Dependence on power

For a two-photon process, we expect an effective Rabi frequency which obeys $\Omega \propto \Omega_L^2/\Delta$ [152]. We drive an electric dipole transition, meaning that the Rabi frequency Ω_L for the individual transitions is proportional to the matrix element of the relevant states with the electric dipole operator. This has the form, for example:

$$\langle \uparrow | \vec{E} | \uparrow \downarrow \uparrow \rangle = |\vec{E}| \langle \uparrow | \vec{r} | \uparrow \downarrow \uparrow \rangle \quad (3.8)$$

Here, $|\vec{E}|$ is the electric field strength of the optical field, which depends

on the square root of the laser power. As a result, we expect that a two-photon process will show a linear dependence of its Rabi frequency on laser power, in contrast to the square-root dependence of a single-photon process. In Figure 3.4, we drive Rabi oscillations at two-photon resonance for a set of different input powers. We then extract the oscillation frequency to show its dependence on power; this is well described by a linear fit to the data, evidencing the two-photon nature of the process. We note that for Rabi frequencies under 100 MHz, Rabi oscillations are impeded by nuclear feedback effects.

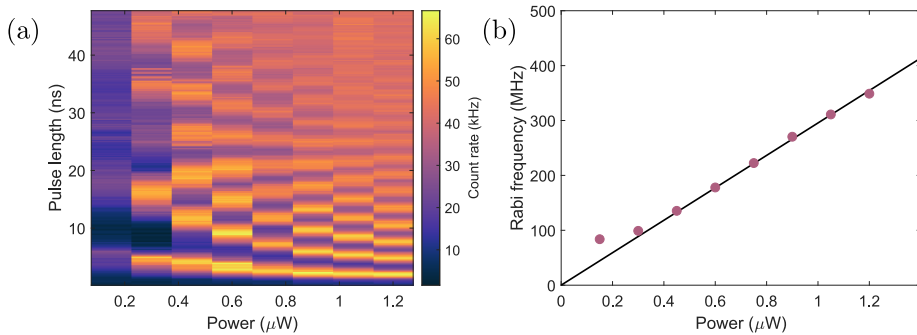


Figure 3.4: (a): Driven Rabi oscillations as a function of input laser powers. (b): Rabi frequency extracted from fits to data in (a) as a function of input laser power (pink data points), with a linear fit to the data (black curve).

3.6 Dependence on single-photon detuning

The above form of the effective Rabi frequency means that we expect a Rabi frequency depending on the single-photon detuning as $1/\Delta$ [152]. In Figure 3.5, we drive Rabi oscillations at two-photon resonance for a set of different single-photon detunings. We then extract the Rabi frequency of these oscillations and plot it as a function of single-photon detuning; the

expected behaviour is closely followed.

At single-photon detunings which are small enough to be comparable to the single-transition Rabi frequencies, we expect to generate excited-state population. In our case, the excited state is additionally broadened by a phonon sideband, which in this experiment can be seen to dramatically reduce oscillation visibility when the single-photon detuning is less than 25 GHz. This is because populating the excited states enables incoherent spontaneous decay processes, which randomise our hole spin.

In addition, we are prevented from operating at single-photon detunings exceeding 70 GHz since in this case our Rabi frequency drops below the 100 MHz cut-off shown in Fig. 3.4 to render the experiment susceptible to nuclear spin feedback effects.

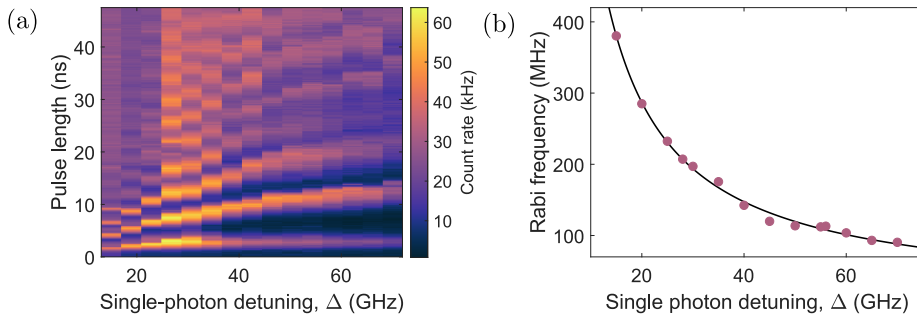


Figure 3.5: (a): Rabi oscillations as a function of single-photon detuning. (b): Rabi frequency extracted from fits to data in (a) (purple circles), which has then been fitted with Δ^β with $\beta = -1.01(9)$ (black curve).

3.7 Ramsey interferometry I

A convenient method for demonstrating access to any point on the Bloch sphere, an essential requirement for a qubit control technique, is Ramsey interferometry [183]. This involves applying two $\frac{\pi}{2}$ pulses to the qubit, sep-

arated by a variable time delay τ . During this period of free evolution, the spin precesses at the Larmor frequency, which we previously observed in Fig. 2.13. Figure 3.6 presents Ramsey interferometry performed using our Raman drive technique. In this case, the first pulse defines an initial phase for the system, rotating the Bloch vector into the equatorial plane of the Bloch sphere. Once the pulse is turned off, the Bloch vector undergoes Larmor precession in the external magnetic field. However, because the final pulse is generated using the same, phase-stable microwave signal as the first, it acquires phase during the free precession period at twice the microwave modulation frequency. For this reason, when the microwave frequency matches half of the hole Zeeman energy, no Larmor precession is observed: the final rotation pulse “Larmor-precesses” with the spin. When we do not match the hole spin resonance, the system is observed to precess at the two-photon detuning δ , which is the difference in precession frequency between the drive and spin.

Because in this case the drive acquires phase at twice the modulation frequency, the observed precession frequency is given simply by δ , the two-photon detuning. In other words, when we are on resonance with the hole spin, the Bloch and Rabi vectors are phase-locked and no precession is expected. In the data, we observe exactly this: a linear dependence of precession frequency on δ .

This ideal behaviour is partially obscured by the presence of nuclear spin feedback effects, which are likely responsible for the global oscillation on a ~ 25 ns timescale. These effects are more prominent in the case of Ramsey interferometry than under Rabi drive because the system is more sensitive to Overhauser field in this configuration. Altering the Overhauser field leads to a different precession frequency, and so a different final state. When

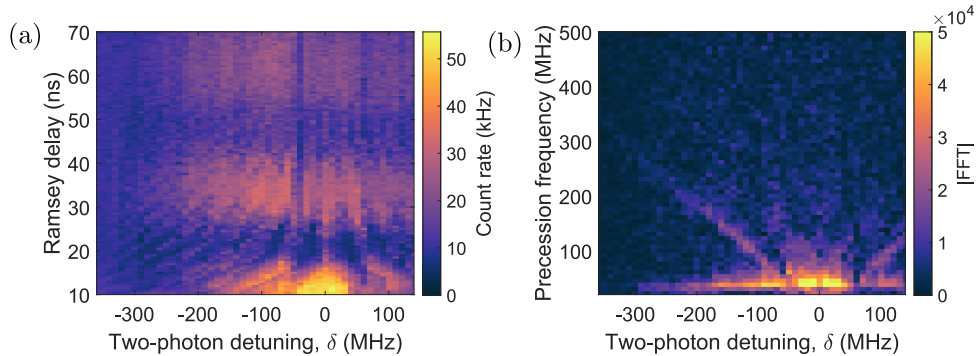


Figure 3.6: (a): Ramsey interferometry on a single hole spin, as a function of two-photon detuning δ . (b): FFT of data in (a).

we consider that our readout processes are subject to nuclear feedback and appear “dragged” or “anti-dragged” as a result, we note that Ramsey interferometry is in practice a highly effective method for altering the nuclear state [156, 220]. This has unfortunate consequences for this particular experiment, reducing our access to the ideal spin behaviour. Serendipitously, these feedback effects can be mitigated by a number of methods; we shall exploit one of them in an later version of this experiment in Section 3.9.

3.8 Phase control

An important advantage of this technique is the possibility of controlling the azimuthal angle of the Rabi vector with respect to the Bloch vector, through the phase of the microwave signal. This corresponds to full $SU(2)$ control over the Rabi vector itself, making rotation of the spin about any axis possible. Thus far, we have used the combination of microwave source, switch and delay generator in order to generate our pulse sequences. To incorporate phase control, we replace this system with an arbitrary waveform generator (AWG) (Tektronix AWG70002A). This gives us the ability to

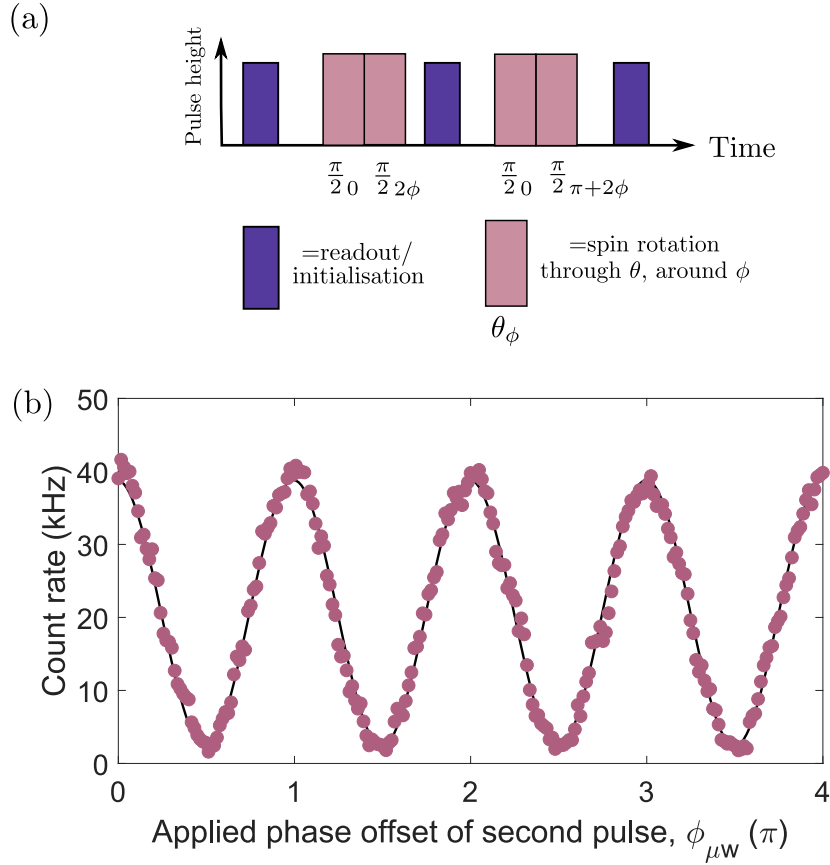


Figure 3.7: (a) Pulse sequence schematic. (b) Resulting count rate (pink circles) and a sinusoidal fit (black curve).

design waveforms electronically, whose phase we can trivially control. Since the AWG is capable of generating arbitrary waveforms, we no longer need the switch to turn the microwave signal off. We simply feed the AWG signal (after amplification, with a Tektronix PSPL5865 12.5 GHz amplifier) directly to the EOM. This setup allows us to design arbitrary pulse sequences, with freedom to vary the phase of the microwave signal within a single pulse sequence. Further details of the microwave system are given in Appendix [A](#).

We demonstrate this phase control by performing zero-delay Ramsey interferometry. In this implementation, we do not vary the separation of our two $\frac{\pi}{2}$ pulses, which is fixed at zero. We instead increase the phase of the second pulse relative to the first, as shown in Fig. 3.7 (a). This has the effect of precessing the rotation axis of the second pulse, rather than precessing the spin. The resulting fringes are plotted in Fig. 3.7 (b), and demonstrate our ability to jump the phase of our drive. The expected doubling of the microwave phase $\phi_{\mu\text{w}}$ is observed, as the pulse phase ϕ precesses through a full 2π each time $\phi_{\mu\text{w}}$ increases by π .

In addition, because these fringes were acquired using two immediately consecutive pulses, we confirm our ability to jump the phase of the drive on a fast timescale compared to the pulses themselves. In this dataset, visibility is limited simply by the fidelity of our pulses, which is discussed further in Section 3.10.

3.9 Ramsey interferometry II

One consequence of this capability is the pulse sequence depicted in Fig. 3.8 (a); here, we pair our control sequences into readouts of the $|\uparrow\rangle$ and $|\downarrow\rangle$ states. This is done by adding an additional phase of π to the final rotation pulse on the second sequence in the pair. In this manner we can avoid generation of hole spin polarisation during our sequence. To understand why this is advantageous, let us imagine using a “dragged” transition to read out and prepare the hole spin. In this case, the nuclear environment undergoes stable, negative feedback as part of the scattering process. Hence, when the scattering rate is highest, the system is most stable: it effectively prefers to be bright. The result of this process is that feedback acts on the nuclear state

in order to maximise the count rate after a Ramsey sequence. If the Ramsey delay and detuning are such that the hole spin precesses through an angle of π , the readout will be bright and feedback will be minimal. However, if the spin has precessed through $\frac{\pi}{2}$, the system is maximally sensitive to changes in Overhauser field, which will be driven to increase, increasing the Overhauser shift and the resulting precession frequency. Conversely, if the spin has precessed through $\frac{3\pi}{2}$, the system will drive a reduction in the Overhauser field for the same reason. Crucially, therefore, the sign of the feedback changes as the hole spin passes multiples of π in precession angle. With this important observation in mind, if we now consider an experiment where we alternate the hole spin state which is bright, we can reduce nuclear feedback effects [156].

To this end, we generate the pulse sequence depicted in Fig. 3.8 (a). Using this approach of pairing sequences of opposite hole spin polarisation, we repeat the measurements presented in Fig. 3.6. The resulting data are presented in Fig. 3.8 (b,c); we observe improved access to the ideal hole spin behaviour. Oscillations emerge at a frequency equal to δ , as the spin and drive precess relative to each other, with a global loss of contrast with increasing τ over the hole spin dephasing time T_2^* .

Again, as when driving Rabi oscillations, we observe the departure of our hole spin from the behaviour of an ideal two-level system. In this case, the signal is globally modulated at ~ 40 MHz, and the oscillation contrast is insensitive to δ . These effects are more pronounced than those seen under Rabi drive because the free precession of the hole spin is sensitive to the Overhauser field to first order via δ (whereas the precession [grand Rabi] frequency goes as $\sqrt{\Omega^2 + \delta^2}$ during a Rabi pulse).

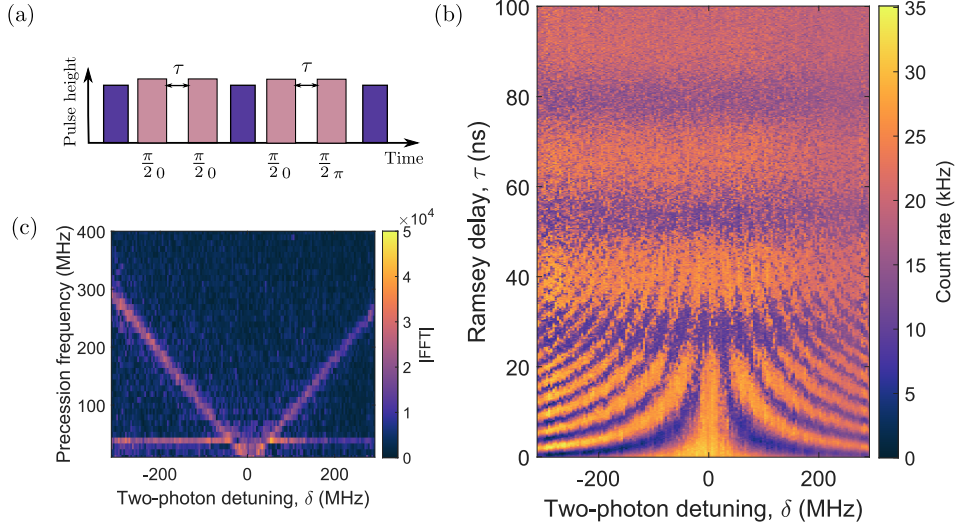


Figure 3.8: (a) Polarisation-minimising Ramsey pulse sequence schematic. (b) Measured count rate on application of the pulse sequence in (a), as a function of two-photon detuning δ . (c) FFT of data in (b).

3.10 Pulse fidelity

We now wish to characterise the fidelity of our hole spin control, which is typically performed using a series of gates randomly sampled from the possible operations (“randomised benchmarking”) [221–223]. However, for our relatively modest fidelities we can approach this simply by fitting our Rabi oscillations with the functional form $\cos(2\pi\Omega t)e^{-\Gamma t}$, allowing us to extract the Rabi frequency Ω and decay rate Γ . From these, we compute the Q factor as twice the ratio of the Rabi frequency to the decay rate. This Q factor is in direct analogy to the language used in other branches of physics, and here refers to the number of π rotations completed before the visibility falls to $\frac{1}{e}$ of its initial value. From the Q factor, the fidelity of a π rotation is simply given by $f_\pi = \frac{1}{2}(1 + e^{-\frac{1}{Q}})$, [224]. This expression

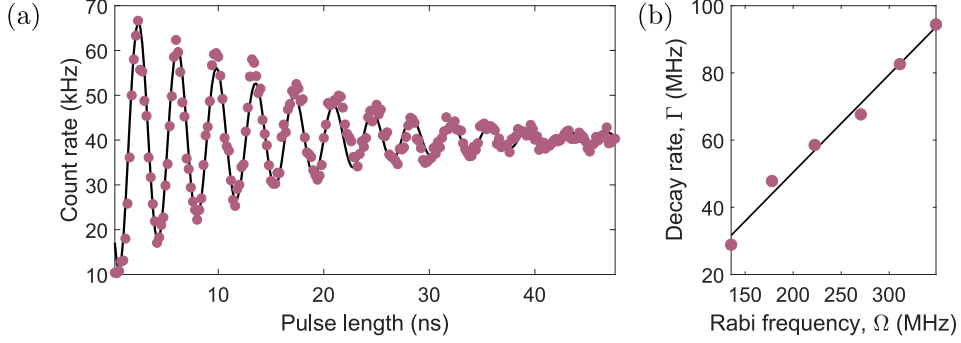


Figure 3.9: (a) Rabi oscillations of a hole spin (pink circles) and a fit (black curve), whose functional form $a \cos(2\pi\Omega t)e^{-\Gamma t} + b$ allows Rabi frequency Ω and decay rate Γ to be extracted. (b) Fitted decay rates Γ vs. fitted Rabi frequencies Ω .

applies when the Rabi frequency greatly exceeds the Overhauser width, a condition which is discussed in much more detail in Section 4.7. In our case, the Overhauser width is difficult to accurately extract from the data in Fig. 3.8 (b) due to the evident nuclear spin feedback effects, but we can safely estimate it as $\mathcal{O}(\text{MHz})$, consistent with the extensive measurements of Ref. [157].

With this in mind, Fig. 3.9 (a) depicts Rabi oscillations from which we extract a Rabi frequency of 270 ± 1 MHz and a decay rate of 67 ± 6 MHz, leading to a fidelity of $94.1 \pm 0.2\%$. This comfortably surpasses the previously measured f_π of $89 \pm 1\%$ for hole spin control using ultrashort pulses [157]. This increase in fidelity could be a result of the smaller optical power needed here, since our control pulses have lower single-photon detuning than required for an ultrashort pulse; high laser power at the sample can generate charges, which have been shown to dephase the hole spin [157].

Figure 3.9 (b) plots extracted decay rate Γ against Rabi frequency Ω . The observed dependence, which agrees closely with a linear fit, indicates their relationship of direct proportionality. Because f_π depends on their

ratio, this result indicates that we cannot exceed our currently achieved fidelities by moving to higher Rabi frequency. In doing so, we accelerate dephasing of the system, capping our Q factor and fidelity.

When the Rabi frequency is large, variations in the Overhauser field have an effect on the Rabi frequency and polar angle of the Rabi vector, which are both suppressed by a factor $\frac{1}{\Omega^2}$. However, when the Rabi frequency is decreased, our π rotations become much more sensitive to nuclear spin feedback effects, which in this regime can alter the rotation angle since they can be as large as the Rabi frequency. In this regime, control fidelity is impaired; for these reasons, we cannot improve our fidelities by tuning Rabi frequency.

3.11 Conclusions and Outlook

In this Chapter we have seen that using Raman control to manipulate a single hole spin confined to a QD circumvents many of the challenges of the previous state-of-the-art, allowing the straightforward construction of arbitrary pulse sequences. We first showed that this technique allowed the coherent control of a hole spin, and confirmed the two-photon nature of the process. We then demonstrated that this approach gave us full $SU(2)$ control over the Rabi vector itself. As a working example, this flexibility trivially allowed the construction of a Ramsey pulse sequence with improved access to the ideal quantum dynamics of the hole spin qubit. Whilst Raman control operates at lower Rabi frequency than its predecessor, the relatively long coherence time of a hole spin nevertheless enabled us to achieve a significantly higher fidelity, bringing Raman control firmly into pole position for future work involving spin control in QDs.

The immediate next step is to improve the fidelity of our operations. Whilst we have exceeded the previous state-of-the-art, our maximum fidelity of 94% still only allows 16 π -gates before the visibility falls to $1/e$, placing another hard limit on the pulse control protocols available. Experiments on different QDs have shown anticorrelation between control fidelity and electrical noise in the QD vicinity [49], but the exact microscopic mechanism remains unclear. It may be possible to improve fidelities with alterations to the device design, but in the absence of an understanding of the mechanisms at play the necessary changes are not evident.

From a longer term perspective, we must consider the hole spin in the context of our motivation of constructing a quantum network. This requires the storage of information in a network node for a time longer than the photon travel time between two nodes. Therefore, the node coherence time constrains the maximum physical separation of the nodes. In order to achieve a certain node separation, the node coherence time must be accordingly long (several tens of microseconds of coherence allows tens of km separation). Exploiting a hole spin for this task means that the storage time is given by the hole spin coherence time T_2 , which is fundamentally limited by electrical noise within the QD device [157]. Improving the T_2 of the hole spin beyond its current maximum of a few μs is a question of device engineering and sample fabrication, and will not be the focus of the remainder of this dissertation.

In order to sidestep these challenges, we change our basis to the electron spin from hereon in. The reasons for this are twofold; the first concerns fidelity, and the second coherence. The electron has previously (when working with ultrashort pulses) supported operations of higher fidelity than the hole, and we therefore hope for a straightforward improvement in control

fidelity when switching to the electron. We will see (in [Chapter 4](#)) that this requires some optimisation of the electron spin coherence, which is strictly limited by its environment of nuclear spins. Fortunately, and interestingly, we can take steps in order to lift this limit.

Chapter 4

Optical Spin Locking of a Solid-State Qubit

In Chapter 3, we implemented a new technique for controlling a hole spin confined to a QD. This technique proved itself superior to the previous state of the art in almost every regard, losing out only on rotation speed. However, whilst it surpassed pulsed laser control with regard to rotation fidelity, the maximum of 94% remains well short of the requirements of quantum technological applications.

However, in QDs, there exist two possible platforms for spin control: a single hole, or a single electron, each bringing their own challenges and opportunities. The shorter spin coherence time of an electron makes coherent control more difficult, but the electron spin could offer the potential to match or exceed the 97% rotation fidelity achieved using ultrashort pulses. This would allow Raman control to fully surpass ultrashort pulsed laser control. In parallel, the shorter electron spin coherence time originates from a

stronger coupling to the nuclear environment. Whilst this frustrates efforts to control it coherently, the two-way nature of this coupling also presents an opportunity to address the nuclear spins through their interaction with the electron spin.

In this Chapter, we demonstrate high-fidelity control of a QD electron spin, using Raman control. We circumvent the challenge of short electron spin coherence by extending it, using an optical nuclear spin narrowing technique to reduce noise from the environment. Using our Raman control technique, we are then able to deterministically enable and disable coupling to the nuclear ensemble. This allows us to protect a known quantum state from decoherence, using a particular multi-axis control sequence known as spin locking.

The measurements of Sections 4.2 & 4.3 were carried out with Rob Stockill. The remaining work presented in this Chapter was carried out with Claire Le Gall. The nuclear spin narrowing technique was developed by Dorian Gangloff and Gabriel Éthier-Majcher. Modelling of the Hartmann-Hahn resonances discussed in Section 4.7, as well as development of the theory underpinning the electro-nuclear interactions, were performed by Emil Denning. Modelling of spin locking presented in Section 4.8 was performed by Claire Le Gall. The results of this Chapter have been presented in two peer-reviewed publications [176, 224].

4.1 Experimental setup

In switching our focus from a hole spin to an electron spin, we must make some minor modifications to the experimental setup discussed in Section 3.3. Firstly, we no longer require photocreation of holes. Secondly, the electron

spin resonance is significantly larger than the hole spin resonance (in our case, 25 GHz vs. 9 GHz). The microwave frequencies required are at the bandwidth limit of our AWG, and to retain phase control of the microwave signal we therefore alter our microwave setup as detailed in Appendix A. With these small changes, we can now design arbitrary pulse sequences electronically to address the electron spin.

4.2 Preliminary spin control

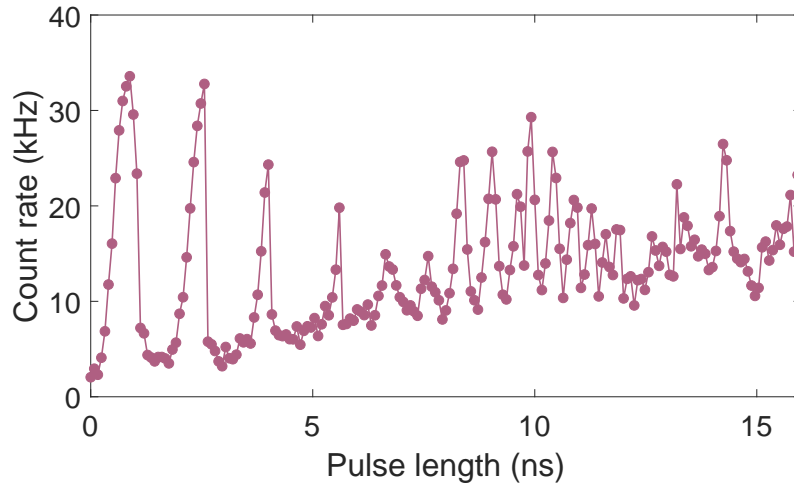


Figure 4.1: Count rate as a function of pulse length, for a Raman pulse resonant with the ESR. Data points are pink circles, and pink lines simply connect them to guide the eye.

Working with an electron spin, rather than a hole spin, increases the coupling strength between the qubit and its nuclear environment by an order of magnitude. This poses challenges for coherent control, which we were able to perform in Chapter 3 by simply driving Rabi oscillations, with no regard

given to the environmental coupling. Here, blissful ignorance of the nuclei is no longer sufficient, as we see in Fig. 4.1. We drive the system with a Raman pulse of variable length, and measure the subsequent spin polarisation via the count rate. Coherent Rabi oscillations are dramatically and emphatically obstructed by environmental coupling, leading to a saw-tooth response and a sharply reduced visibility. These interesting effects have been extensively studied in QDs (see e.g. Ref. [156]). Here, however, our aim will be to avoid them.

4.3 Composite control sequences

As we saw in Chapter 3, using Raman beams to control a spin confined to a QD brings some important advantages over the previous state of the art. Of particular relevance to this section will be the ability to implement control sequences composed of an arbitrary number of spin rotations, each rotating about an arbitrary axis, and all separated by arbitrary delays. This level of flexibility is not unique to QD spin control, and indeed has become a keystone capability in other physical systems, including nuclear magnetic resonance (NMR) [207, 225], superconducting circuits [226], and nitrogen-vacancy centres in diamond [204]. The maturity of NMR in particular has allowed the development of a wide variety of so-called “composite control” techniques.

Composite control techniques are pulse sequences which are designed to perform qubit gates with improved fidelities with respect to regular control pulses, by compensating for various types of error [208, 227]. In NMR, the most common error types are pulse length errors, where the rotation angle differs from the intention, and detuning errors, where the resonance

condition varies across the ensemble of spins under study and so gives an uneven rotation. In the case of QDs we can encounter both of these errors; whilst we control a single confined spin rather than an inhomogeneous ensemble, slow Overhauser noise means that our resonance condition varies from experimental run to run and we arrive at a similar result.

Throughout this Chapter, we will use the convention that $(\theta)_\phi$ denotes a rotation of angle θ , around a Rabi vector which has an azimuthal angle of ϕ . We begin with a simple control sequence which involves replacing a regular π_0 rotation with a composite pulse having the form [227]:

$$\frac{\pi}{2}_{\phi_1=0} \pi_{\phi_2=\frac{\pi}{2}} \frac{\pi}{2}_{\phi_3=0} \quad (4.1)$$

This sequence is designed to correct for pulse length errors; Figure 4.2 (a) depicts its performance against a direct rotation when subject to this type of error. However, we also find this protocol to exhibit enhanced robustness to detuning errors compared to a direct rotation, as shown in Fig. 4.2 (b). This sequence should therefore improve our rotation fidelities in the regime where we are limited by nuclear feedback effects, because these manifest themselves as a shift in the resonance condition (or equivalently, a detuning error).

In Fig. 4.2 (c), we drive the system with a pulse sequence whose form we tune continuously from regular to composite rotation. To do this, we vary the phase ϕ_2 of the central portion of the pulse relative to the ends. We also vary the length of the total sequence (whilst keeping the proportions fixed i.e. the ends are always half the length of the central portion). From this, we select two linecuts corresponding to a composite rotation ($\phi_2 = \frac{\pi}{2}$) and a direct rotation ($\phi_2 = 0$); these are pitted against one other as a

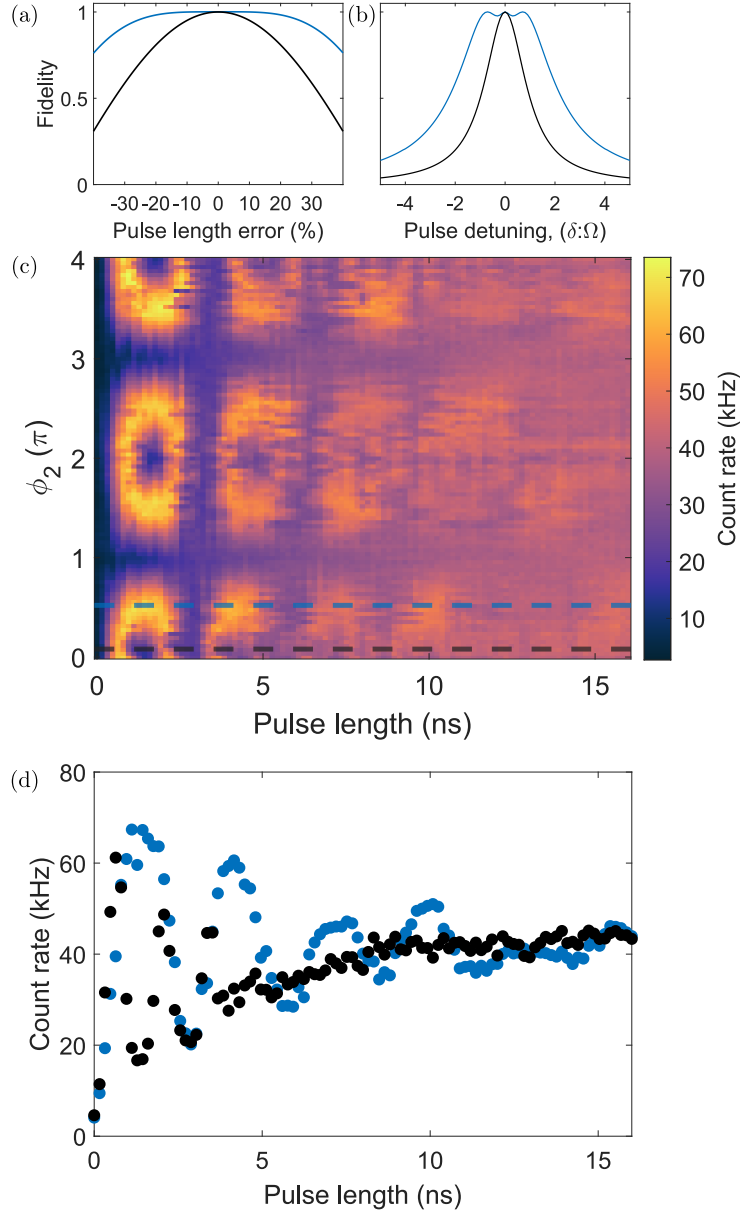


Figure 4.2: Calculated π -rotation fidelity of a composite pulse (blue curve) and a direct rotation (black curve), in the presence of (a) pulse length errors and (b) detuning errors. (c) Count rate as a function of the length of the entire pulse, and of the phase ϕ_2 of the central half of the pulse. When $\phi_2 = 0$ ($\pi/2$), direct (composite) rotations are performed. (d) Linecuts from the data in (c) as indicated by the dashed lines.

function of pulse length in Fig. 4.2 (d). Its resistance to pulse errors means that the composite rotation clearly outperforms the direct drive, exhibiting more oscillations and at a higher amplitude, over a longer period of time. Whilst this composite pulse sequence does improve our control fidelity, it nevertheless remains low. The tight lower bound on Rabi frequency imposed by the short coherence time of the electron spin, coupled with the tight upper bound on Rabi frequency imposed by the need for low population in the excited state, means that we need a different approach.

4.4 Nuclear state preparation

We can directly extend the coherence time of the electron spin using nuclear state preparation. This idea, whereby the electron is driven in such a way as to remove entropy from its environment, has been extensively studied and performed in QDs using a variety of techniques [185, 228–233]. Here, we will focus the discussion on our immediate aim, which is twofold: to reduce the Overhauser broadening of the ESR and to pin the Overhauser field close to zero.

To this end, we utilise our Raman drive by developing an approach in close analogy to Raman cooling of atoms [234, 235]. We drive our negative trion system with a Raman laser and a repump laser, as illustrated in Fig. 4.3 (a). However, in contrast to our previous pulsed experiments, we now drive the system with both lasers continuously and simultaneously (Fig. 4.3 [b]). Because the excited state population decays very quickly compared to other timescales in the system, we can reduce our consideration to an effective two-level system of the electronic spin states, shown in Fig. 4.3 (c). In this drive configuration, we have engineered an effective lifetime to $|\downarrow\rangle$,

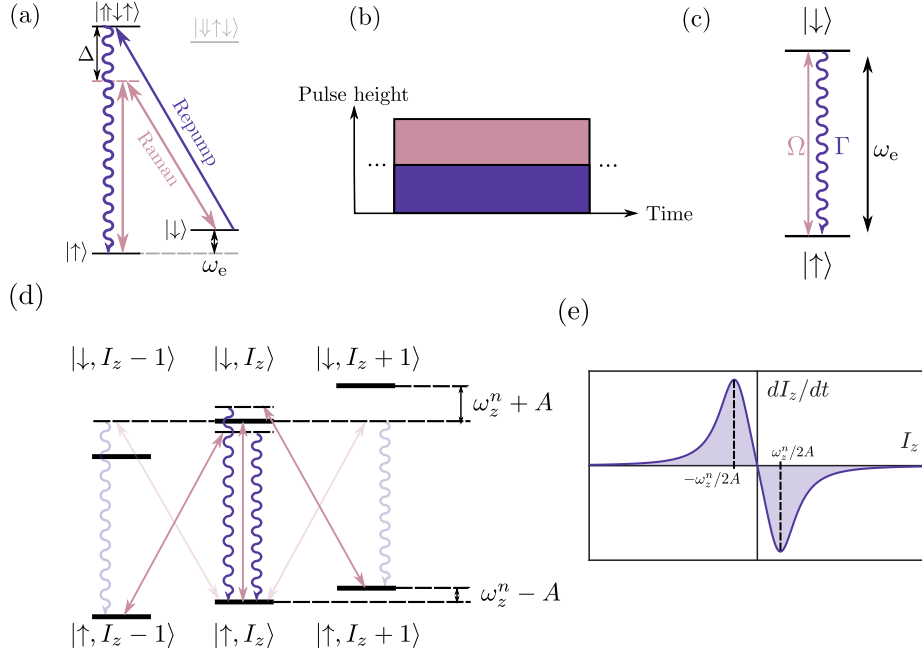


Figure 4.3: Raman cooling using the negative trion. (a) The ESR is driven by two Raman beams, detuned from the excited states. A repump laser transfers population from $|\downarrow\rangle$ to $|\uparrow\uparrow\uparrow\rangle$, from where it decays to $|\uparrow\rangle$. (b) We drive the system continuously with both Raman and repump lasers. (c) Effective two-level system formed by the electron spin states split by ω_e , driven resonantly at a Rabi frequency Ω and with effective decay rate Γ caused by the repump laser. (d) Dressing the states of (b) with nuclear state, parametrised by average polarisation I_z . The resulting ladder of states (split by the nuclear Zeeman energy ω_z^n) is anharmonic due to the hyperfine interaction between electronic and nuclear spins (characterised by A). The thick pink arrow is the ESR, which is resonantly driven. The thin but solid pink arrows are diagonal transitions, which are driven near-resonantly. The faint pink arrows are off-resonant transitions. Purple wiggly arrows are radiative decay channels. (e) Feedback function generated by the drive scheme. Fluctuations away from the preferred polarisation generate negative feedback, which peaks in strength when the Raman beams resonantly drive diagonal transitions on the ladder of states of (d). This condition is met approximately when $I_z = \pm\omega_z^n/2A$.

set by the repump power, which is much shorter than the bare spin lifetime $1/T_1$.

On top of these two electronic levels, we now bring the nuclear spin state into the picture, which we parametrise using the total polarisation I_z . The electron spin and nuclear spins have Zeeman energies ω_e and ω_z^n respectively. In addition, the hyperfine interaction (characterised by the hyperfine constant per nucleus A) between the electronic and nuclear spins causes the ESR frequency to depend on I_z via the Overhauser effect. We then arrive at the ladder of energy levels shown in Fig. 4.3 (d); anharmonicity is caused by the hyperfine interaction.

Within this ladder, we wish to understand the transitions which are allowed. Obviously, vertical transitions correspond simply to the electron spin resonance at a given nuclear polarisation. The quadrupolar Hamiltonian detailed in Section 2.6, induced by the strained setting provided by the QD, was previously expressed:

$$\hat{V}'_Q = -\hat{S}_z \sum_j \frac{A^j B_Q^j}{\omega_z^n} \left\{ \left[(\hat{I}_x^j)^2 - (\hat{I}_y^j)^2 \right] \sin^2 \theta^j + \left[\hat{I}_x^j \hat{I}_z^j + \hat{I}_z^j \hat{I}_x^j \right] \sin 2\theta^j \right\}. \quad (4.2)$$

When driving the electron spin, the relevant terms can be acquired by dressing the electron driving Hamiltonian with \hat{V}'_Q , which results in the following correction term:

$$\hat{V}''_Q = -2\Omega \hat{S}_y \sum_j \frac{A^j B_Q^j}{(\omega_z^n)^2} \left[\frac{1}{2} (\hat{I}_x^j \hat{I}_y^j + \hat{I}_y^j \hat{I}_x^j) \sin^2 \theta^j + (\hat{I}_z^j \hat{I}_y^j + \hat{I}_y^j \hat{I}_z^j) \sin 2\theta^j \right]. \quad (4.3)$$

We note that Cartesian nuclear spin operators can be related linearly to

nuclear spin ladder operators according to

$$\begin{pmatrix} \hat{I}_x \\ \hat{I}_y \end{pmatrix} = \frac{1}{2} \begin{pmatrix} 1 & 1 \\ -i & i \end{pmatrix} \begin{pmatrix} \hat{I}_+ \\ \hat{I}_- \end{pmatrix}. \quad (4.4)$$

With this in mind, terms in $\hat{I}_y\hat{I}_z$ and $\hat{I}_z\hat{I}_y$ give rise to single nuclear spin flips, and those in $\hat{I}_x\hat{I}_y$ and $\hat{I}_y\hat{I}_x$ give rise to double nuclear spin flips, taking place at a rate dictated by $AB_Q/(\omega_z^n)^2$. Both of these processes are allowed to first order by the nature of our Hamiltonian; the reader is referred to Chapter 5 for a much more detailed investigation of these interactions. For now, we note that we can therefore use the noncollinear hyperfine interaction to drive nuclear spin flips [176]. These spin flips arise as diagonal transitions on our ladder of states, connecting levels of different nuclear polarisation.

In the ladder of states shown in Fig. 4.3 (d), spontaneous I_z -preserving decay from the upper levels is driven by the repump laser, and vertical (electron-only) and diagonal (electro-nuclear) spin-flipping processes can be driven by our Raman laser. We emphasise that the Raman laser is allowed to drive 5 electron-spin-flipping transitions: the central ESR, the “first sidebands” which transform $I_z \rightarrow I_z \pm 1$, and the “second sidebands” which transform $I_z \rightarrow I_z \pm 2$.

In order to understand the action of the lasers in this configuration, we picture the system occupying a single microstate: $|\uparrow, I_z\rangle$. Of the 5 Raman-driven transitions, the ESR is by far the strongest. The first sidebands are reduced compared to the central ESR by a factor $\sqrt{N}AB_Q/(\omega_z^n)^2 \sim 0.1$ [176], and are energetically detuned from the drive by ω_z^n . Here, it is sufficient to consider only these processes: we neglect the second sidebands. When the Raman laser is exactly resonant with the ESR, the two $I_z \rightarrow I_z \pm 1$

transitions have the same detuning from the laser, and they are therefore driven at equal rates and there is no net driven polarisation: the system is stable.

We now consider the case of a nuclear state with a polarisation I_z higher than that of the state where the drive is resonant with the ESR. Because of the anharmonicity of the ladder, our drive is closer to resonance with the diagonal transition which reduces I_z than to its I_z -increasing counterpart. Conversely, a state with polarisation smaller than the ESR resonance condition leads to the reverse arrangement; transitions which increase I_z become preferred. Driving the system in this configuration therefore induces negative feedback on the nuclear polarisation, narrowing it around a stable lockpoint where the drive is resonant with the ESR. The feedback function which we generate is depicted in Fig. 4.3 (e). Fluctuations in polarisation are driven back towards the stable point. Feedback strength peaks when the Raman drive becomes exactly resonant with a diagonal transition i.e. when the change in I_z , $\Delta I_z \times 2A = \omega_z^n$.

As a side note, the choice of electron spin state which is used as the effective excited state is crucial here, since it dictates the anharmonicity of the ladder. For stable feedback, we require a ladder whose excited-state splitting exceeds its ground-state splitting. Pumping the other electron spin state results in the opposite type of anharmonicity, leading to anti-stable feedback.

Performing the cooling protocol between each experimental run has a dual effect. It resets the nuclear polarisation to a given value, which reduces nuclear spin feedback effects, and it also reduces the Overhauser fluctuations by pumping the nuclear spins into a narrowed state. We have seen that experimental sequences themselves can exert strong feedback effects onto

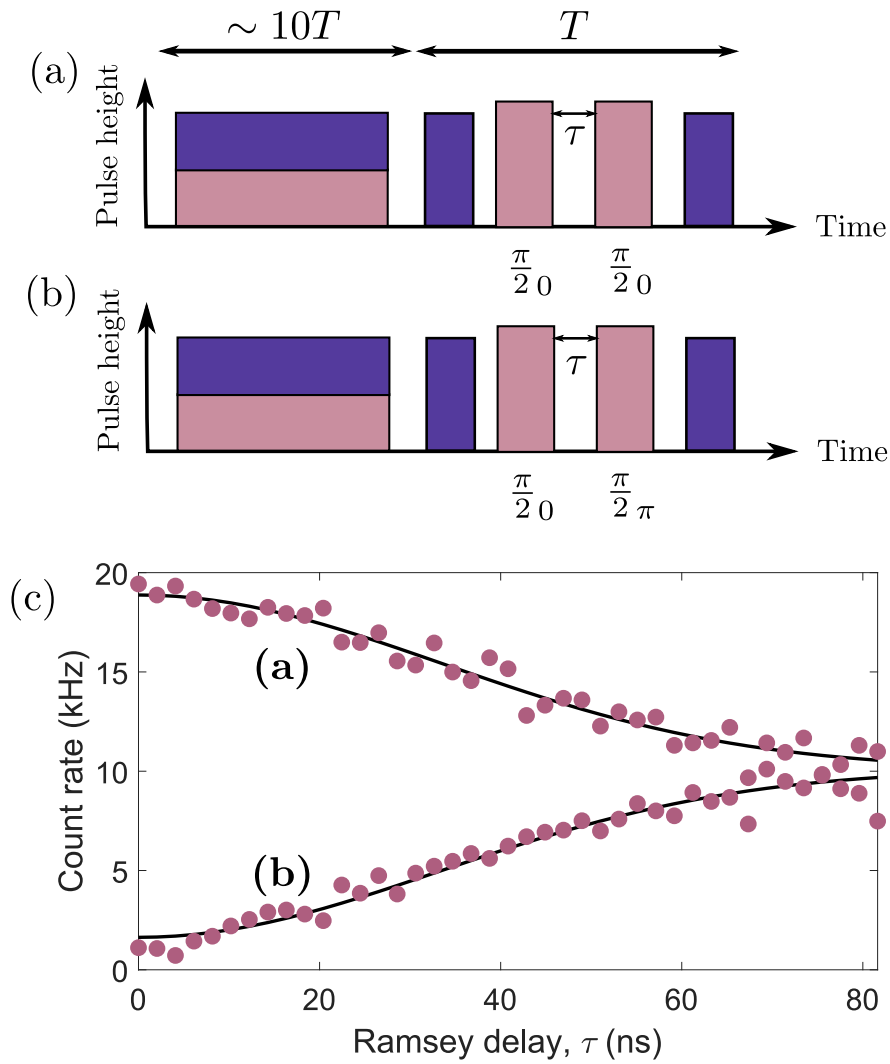


Figure 4.4: (a,b) Ramsey interferometry pulse sequence. We prepare the nuclear environment for a time $10T$, following which we perform Ramsey interferometry for T . We can choose the $\frac{\pi}{2}$ pulses to be (a) in phase or (b) in antiphase, producing the upper and lower data in (c), respectively. These are fitted (black curves) according to $\pm ae^{-(\tau/T_2^*)^2} + b$, yielding $T_2^* = 47(3)$ ns.

the nuclei, and for this reason we operate with a duty cycle exceeding 90%, meaning that we prepare the nuclear state for $> 90\%$ of the time, and perform experiments for the remainder. This ensures that the nuclear spin polarisation remains at the stable point, within the capabilities of the optical feedback.

The optimum performance of this feedback mechanism occurs when the gradient of the feedback function at the stable point is maximised i.e. when the width of the two peaks of the feedback function (Fig. 4.3 [e]) matches their splitting. It can be shown that this is achieved when the ESR Rabi frequency roughly matches half the nuclear Zeeman energy, and the effective excited-state lifetime exceeds the ESR Rabi frequency by a factor of $\sqrt{2}$ [176]. Operating under these conditions, we perform Ramsey interferometry on a confined electron spin, presenting the experimental data in Fig. 4.4. The decay profile we measure matches the Fourier transform of the nuclear distribution; since preparation narrows the distribution, we measure an extended inhomogeneous dephasing time of $T_2^* = 47(3)$ ns. This is an order of magnitude larger than the bare, unprepared T_2^* [156], and corresponds to an Overhauser width of 4.8 MHz. The precise effects of the preparation on the nuclear state will be discussed in detail in Chapter 5.

As a final side note, the reader may have noticed the parallels between the ladder of states of Fig. 4.3 (d) and the ladder of states of Fig. 2.12. Both cases can be described by an anharmonic ladder of states, containing an excited state manifold which decays to a ground state manifold, and both of these configurations exhibit feedback on the nuclei. Besides its extra tunability, the principal advantage of the Raman cooling technique is that it locks to a spin transition, rather than an optical transition. The latter is far less stable because it is sensitive to electrical noise in the environment

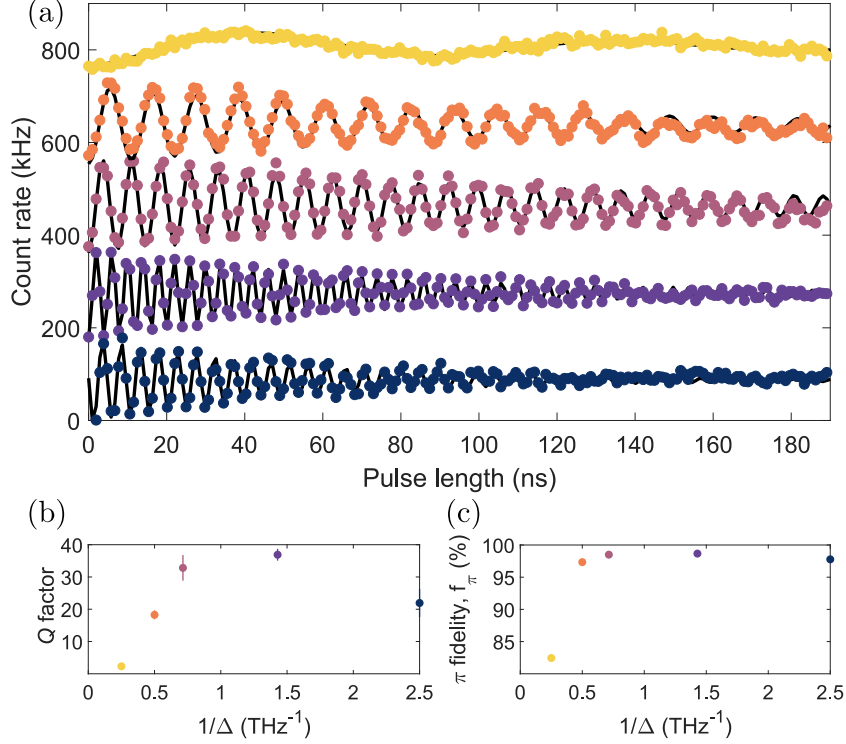


Figure 4.5: (a) Driven Rabi oscillations (coloured circles) after preparing the nuclear state, for single photon detunings $\Delta = [400, 700, 1400, 2000, 4000]$ GHz (bottom to top), offset for clarity. Plotted alongside are fits (black curves) of the form $A \cos(2\pi\Omega T)e^{-T/\tau_{1/e}} + B$. From these fits we extract a Q factor $Q = 2\Omega\tau_{1/e}$ and a π fidelity $f_\pi = \frac{1}{2}(1 + e^{-1/Q})$, which we plot against $1/\Delta$ in (b,c) respectively, indicated by colour. Error bars indicate 66% confidence intervals.

via the DC Stark effect.

4.5 Coherent electron spin control

Having prepared our nuclear environment into a narrow state with a well-defined polarisation, we now return to driving Rabi oscillations. Thanks to our preparation, the new ESR width of a few MHz enables a lower ESR drive frequency, allowing us to increase our single-photon detuning Δ far

beyond our previous limits. In Fig. 4.5 (a) we drive Rabi oscillations for a set of different single-photon detunings. By fitting the response, we can extract the Q factor and π fidelity for each configuration, which we plot in Fig. 4.5 (b,c) respectively.

As we decrease $1/\Delta$ below 1 THz^{-1} , we observe a decrease in Q and f_π , which is particularly marked at the smallest value measured: $1/\Delta = 0.25 \text{ THz}^{-1}$. Here, the fitted Rabi frequency was $10.7 \pm 0.1 \text{ MHz}$. By comparison, in this experiment, our T_2^* of 47 ns corresponds to an Overhauser width of 4.8 MHz . Under these conditions of comparable Rabi frequency and Overhauser width, we expect a considerable decrease in Q as our Rabi drive is no longer powerful enough to decouple the system from its environment. This drive-induced decoupling is discussed in Section 4.7.

Increasing $1/\Delta$ beyond 1.5 THz^{-1} , we observe another decrease in Q and f_π . This could stem from excited state population, which would increase as we increase $1/\Delta$.

We observe a peak in both Q and f_π for $1/\Delta = 1.4 \text{ THz}^{-1}$; the maximum in f_π appears less pronounced simply because of the functional form of the relation between these two parameters. We therefore select this setting for the following experiments. This corresponds to a Q factor of $37(2)$ and a π fidelity of $98.7(2)\%$.

4.6 A return to composite pulses

Having located the optimum operating conditions for Raman control, we now investigate the action of composite pulses on our electron spin [227,236].

We begin with a pulse sequence designed to correct for pulse length errors, which would effectively mitigate errors due to laser power fluctu-

ations, for example. This is because we can operate at Rabi frequencies greatly exceeding the Overhauser width, meaning that we expect detuning errors to be insignificant. The pulse sequence, termed “scrofulous” (Short Composite ROtation For Undoing Length Over and UnderShoot) by its inventors [236, 237], has a complicated general expression; however in the case of our desired π rotation, it can be written in the simple form

$$\pi_0 \pi_{\frac{2\pi}{3}} \pi_0. \quad (4.5)$$

In order to test the fidelity of this composite rotation, we implement a series of these effective π rotations (Fig. 4.6 [a,c]). In this experiment, we tune our input power in order to maximise the fidelity we measure, meaning that we can assume that any errors in pulse length are not systematic. Remaining pulse infidelity leads to a shortening of the Bloch vector, when averaged over experimental runs. Under these assumptions, we expect to see a modulation of the signal according to

$$(1 - [-f_\pi]^{N_\pi}) \quad (4.6)$$

where N_π indicates the number of π rotations applied to the system, and f_π is the fidelity of a single π rotation.

Figure 4.6 (b,d) presents a comparison of the signal we measure, alongside a fit of the above functional form. This allows us to extract fidelities of $f_\pi = 93.0 \pm 0.3\%$ for a “scrofulous” rotation, and $f_\pi = 97.1 \pm 0.2\%$ for a simple π pulse. This result suggests that pulse length errors are not our primary source of error. Instead, because the “scrofulous” sequence is longer than a regular rotation by a factor of 3, its lower performance could be caused by

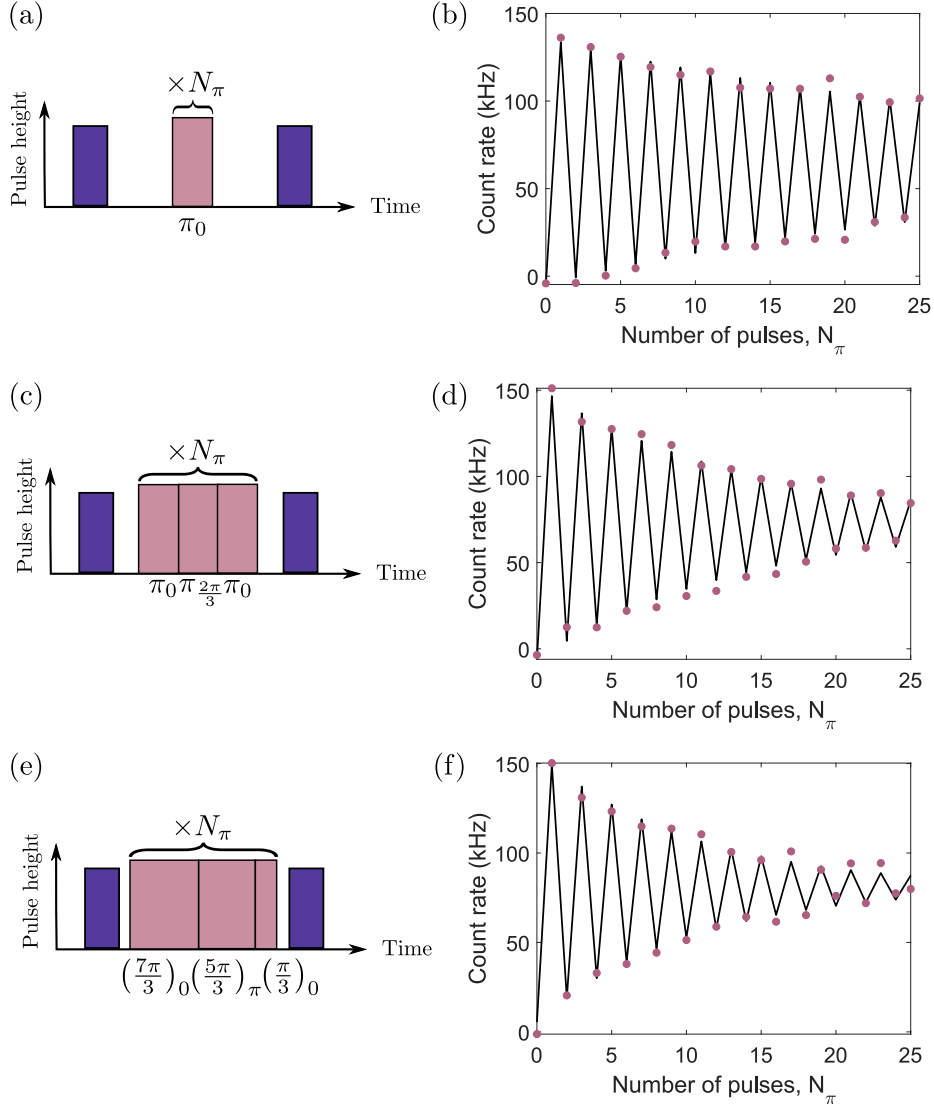


Figure 4.6: Pulse sequences for (a) regular π rotations, (c) “scrofulous” rotations and (e) “corpse” rotations. The resulting count rates are plotted in panels (b,d,f) respectively (pink circles) along with a fit of the form $a(1 - [-f_\pi]^{N_\pi}) + b$ (black curves). From the fits we extract (b) $f_\pi = 97.1(2)\%$, (d) $f_\pi = 93.0(3)\%$, and (f) $f_\pi = 90.6(4)\%$.

a dephasing process related to the total pulse area (but unrelated to errors in the pulse length). This will be discussed in further detail in Section 4.9.

Nevertheless, we proceed to test a pulse sequence designed to correct for detuning errors, in the hope of an (unexpected) improvement in fidelity. The sequence we choose, named “corpse” (Compensation for Off-Resonance with a Pulse SEquence), again has a complicated general form [236]. If a π_0 rotation is desired, however, the sequence is simplified to

$$\left(\frac{7\pi}{3}\right)_0 \left(\frac{5\pi}{3}\right)_\pi \left(\frac{\pi}{3}\right)_0. \quad (4.7)$$

Figure 4.6 (e) depicts the pulse sequence we use, and Fig. 4.6 (f) depicts the resulting count rate along with a fit. In this case, the loss in fidelity when using the composite sequence is even more pronounced: $90.6 \pm 0.4\%$ when using “corpse”. This suggests that off-resonance errors are not primarily responsible for the limitations in fidelity which we observe. In addition, this constitutes further evidence for a dephasing process related to the total pulse area, which is even larger for “corpse” than “scrofulous”.

A final note on this fidelity measurement technique: in the case of composite pulses, where an analytical expression for the pulse for smoothly increasing final rotation angle is not forthcoming, we are forced to adopt the approach of applying a series of π pulses and fitting the envelope. In order to compare these composite pulses to regular rotations, we use the same technique to benchmark the regular π rotation fidelity. In this case, we measure a lower fidelity than we previously recorded by fitting our Rabi oscillations (in Section 4.5). This is because, here, we sample a Rabi curve at multiples of π . The Rabi frequency is pre-defined by the step size of the pulse length, which we must then match by tuning the power. Previously,

we sampled the Rabi curve at very small intervals compared to the period, which renders the fidelity extraction completely insensitive to systematic errors in Rabi frequency by using the Rabi frequency as a fit parameter.

4.7 Power dependence of Rabi oscillations

Whilst we have so far observed a dephasing mechanism which depends on total pulse area, we have not yet explored for which regime of Rabi frequency this mechanism is dominant. With this in mind, we drive Rabi oscillations for a set of different Rabi frequencies, a selection of which we present in Fig. 4.7. In this experiment, our focus is on the decay time of the envelope which encloses these oscillations, since that governs our fidelity. Immediately, we can see by eye that the relation between decay rate and Rabi frequency is not monotonic; in order to capture this behaviour, we must fit the data.

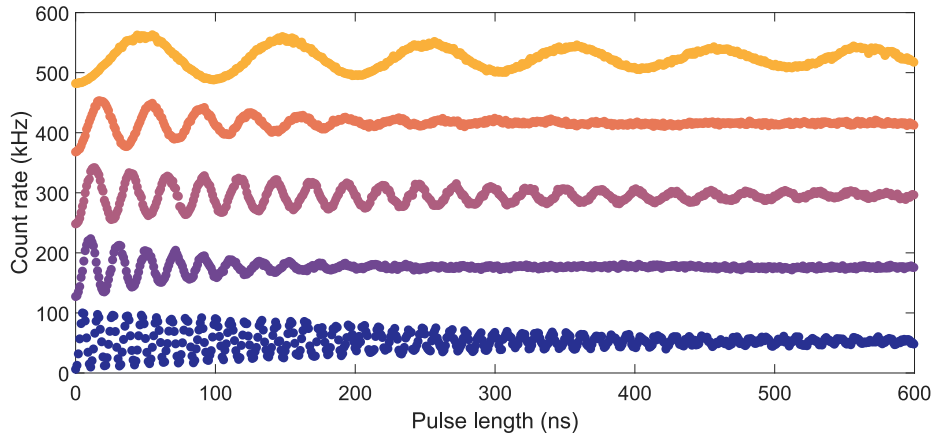


Figure 4.7: Rabi oscillations for a set of different Rabi frequencies, distinguished by colour and offset for clarity.

4.7.1 Fitting in the low-power regime

For most datasets, the decay profile is well described by an exponential envelope; in these cases, we can straightforwardly extract the decay time, Q factor, and π fidelity by fitting. However, in the regime where the Rabi frequency is on the order of the Overhauser noise, we must take a different approach.

The Overhauser noise, which is quasi-static over the course of an experimental sequence but varies from run to run [156], causes the electron spin resonance to sample values from a Gaussian distribution, centred on the electron Zeeman energy, and with a standard deviation of σ (the Overhauser width). This is equivalent to sampling the detuning δ of our drive from a Gaussian distribution, centred around zero, and with a standard deviation of σ . We recall that the Rabi vector is expressed

$$(\Omega \cos(\phi), \Omega \sin(\phi), \delta). \quad (4.8)$$

Fluctuations in detuning therefore affect both the length of the Rabi vector, which is $\Omega' = \sqrt{\Omega^2 + \delta^2}$, and its polar angle, which is $\theta = \arctan(\frac{\delta}{\Omega})$. The length of the Rabi vector is equal to the grand Rabi frequency, and dictates the oscillation frequency under our drive; in the regime where $\Omega \sim \sigma$, we are sensitive to fluctuations in δ to second order only. This means that we do not recover a Gaussian decay profile, as we measured for the case of a linear relation between precession frequency and detuning (under Ramsey interferometry, Fig. 4.4).

The polar angle of the Rabi vector controls the amplitude of oscillation which we can achieve; when the polar angle is $\frac{\pi}{2}$ the Bloch vector traces

a great circle on the Bloch sphere, and oscillation visibility is maximised. For any other value of θ , the Bloch vector traces reduced circles on the Bloch sphere. The oscillation amplitude is given by $\frac{\Omega^2}{\Omega^2 + \delta^2}$ and means that during Rabi oscillations, the average electron spin polarisation is not zero (i.e. the oscillations are not centred around the unpolarised state). This means that using Rabi frequency and decay time to extract fidelity causes an overestimation of the actual maximum population transfer.

In this regime, we instead use a two-level Bloch equation approach to model the response of our system. We describe the time evolution of the electron spin polarisation according to

$$\rho_{\downarrow\downarrow} = -\frac{1}{2} \frac{\Omega^2}{\Omega^2 + \delta^2} \left\{ \cos\left(2\pi \left[\sqrt{\Omega^2 + \delta^2}\right] t\right) + 1 \right\}. \quad (4.9)$$

Next, we constrain our Overhauser noise by performing Ramsey interferometry; the Gaussian decay profile has a characteristic time, T_2^* which is related to the Overhauser width σ according to

$$\sigma = \frac{1}{\sqrt{2\pi}T_2^*}. \quad (4.10)$$

In our case, we measure a T_2^* of 47 ns, which corresponds to $\sigma = 4.8$ MHz (this measurement was presented in Fig. 4.4). We therefore sample δ from a Gaussian distribution, centred around zero, and with standard deviation $\sigma = 4.8$ MHz.

Figure 4.8 (a) presents experimental data obtained under the condition $\Omega \sim \sigma$, along with a fit obtained using a Bloch equation approach. This fit allows us to extract both the π fidelity, by finding the maximum population transfer of the fit, and the time after which the visibility has

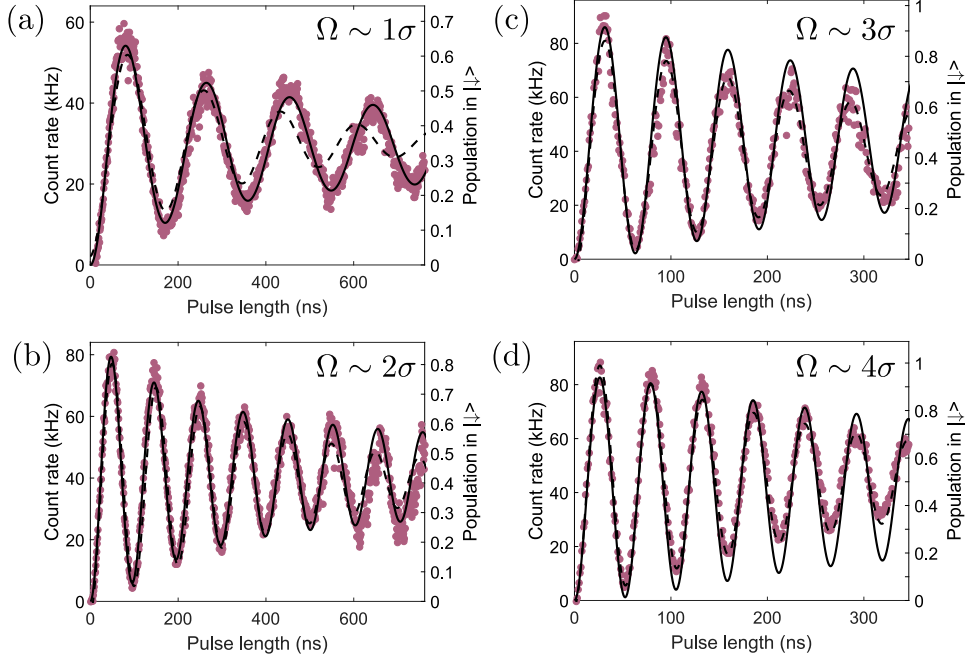


Figure 4.8: Electron spin Rabi oscillations (pink circles) alongside a two-level Bloch equation model (solid black curve) in the presence of Gaussian Overhauser noise of standard deviation $\sigma = 4.8$ MHz. Alongside, we plot a fit of the form $a \cos(2\pi\Omega t)e^{-t/\tau_{1/e}}$ (black dashed lines). Rabi frequencies extracted from the Bloch equation model are (a) 5.25 MHz, (b) 9.75 MHz, (c) 15.25 MHz, (d) 18.5 MHz.

fallen to $1/e$ of its initial value. In addition, we plot a fit of the form $a \cos(2\pi\Omega t)e^{-t/\tau_{1/e}}$, which illustrates the inability of this functional form to capture the behaviour of the system in this regime. Figure 4.8 (b) presents the corresponding measurement when $\Omega \sim 2\sigma$. Here, we see that whilst the Bloch equation approach is still needed in order to correctly reproduce the observed behaviour, the exponential fit has become more faithful to the data than it was for $\Omega \sim \sigma$. As we increase Ω further (Fig. 4.8 [c,d]) the Bloch equation model no longer includes the dominant decay processes and as a result overestimates decay time.

For Rabi frequencies greater than those shown in Fig. 4.8 (a,b), we there-

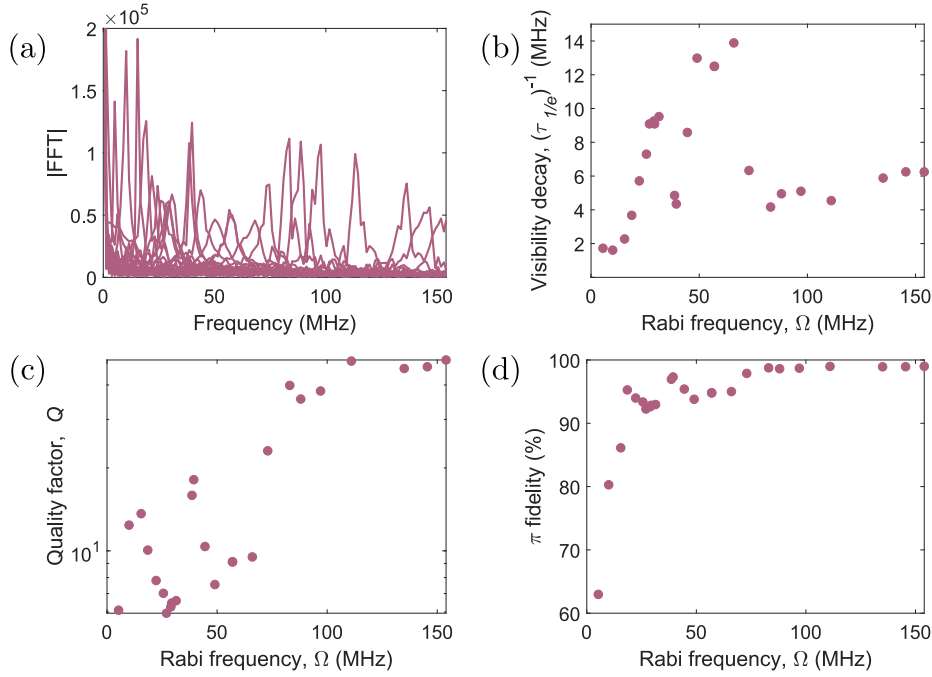


Figure 4.9: (a) FFT of Rabi oscillations, for a set of different Rabi frequencies. (b) Extracted inverse decay time, (c) resulting Q factor and (d) π fidelity, all plotted as a function of extracted Rabi frequency.

fore fit with a exponentially decaying cosine. In this case, we extract the decay rate and Rabi frequency simply from the fit; Q factor and π fidelity follow using $Q = 2\Omega\tau_{1/e}$ and $f_\pi = \frac{1}{2}(1 + e^{-1/Q})$.

4.7.2 The three regimes of electron Rabi oscillations

We plot the FFT of the entire dataset in Fig. 4.9 (a) as a guide to the eye. We then plot the extracted inverse decay time against Rabi frequency in Fig. 4.9 (b), along with the resulting Q factor and π fidelity (Fig. 4.9 [c, d] respectively). In these data we note three distinct regimes.

The first concerns the low Rabi frequency limit, where the response of the system is governed by Overhauser noise. In this regime, we observe the

smallest inverse decay times, but the smallest fidelities.

The second regime applies at high Rabi frequencies, exceeding 80 MHz. Here, we expect the shielding of the system from Overhauser noise by the drive to improve with increasing Rabi frequency. This is because in the limit $\Omega \gg \sigma$, the Rabi frequency can be approximated

$$\sqrt{\Omega^2 + \sigma^2} \approx \Omega \left(1 + \frac{\sigma^2}{2\Omega^2}\right). \quad (4.11)$$

Meanwhile, the amplitude of Rabi oscillations depends on detuning according to

$$\frac{\Omega^2}{\Omega^2 + \sigma^2} \approx \left(1 - \frac{\sigma^2}{\Omega^2}\right). \quad (4.12)$$

Fluctuations in both of these parameters are therefore suppressed by increasing Ω . However, we observe that this regime is instead described by a Q factor which is capped; varying Rabi frequency has no effect on Q . This can equivalently be seen in the inverse decay time, which increases linearly with Ω ; this indicates that the drive power accelerates the decay rate of our Rabi oscillations. Whilst the fidelity is capped, we nevertheless attain a maximum value, at $\Omega = 154$ MHz, of 98.86(4)% - the highest ever achieved using optical control of an electron spin in a QD.

The third regime denotes the region from 20-80MHz, within which we observe decay rates much larger than would be expected from the above power-dephasing arguments, alongside a reduced Q factor and fidelity. In this regime, a different mechanism is therefore responsible for the behaviour which we observe.

4.7.3 Hartmann-Hahn resonances in a QD

In order to understand the behaviour of our system in the intermediate Rabi-frequency regime, we move into the dressed state picture. Here, we consider our drive as redefining an eigenbasis for the system, indicated by $|\hat{\uparrow}\rangle$ and $|\hat{\downarrow}\rangle$ - the dressed states, which are parallel and antiparallel to the Rabi vector, respectively. In this picture, the dressed states are separated in energy by $\hbar\Omega$, which is in direct correspondence with the “undressed” picture where the drive induces spin precession around the Bloch sphere at frequency Ω : Rabi rotations. We have previously seen that the QD is described by an electro-nuclear state, which we can characterise by electron spin polarisation, and nuclear polarisation I_z . In the dressed state picture, for each value of I_z we obtain two electronic states (the dressed states), and when I_z changes by one unit, the energy of both of these states shifts by the nuclear Zeeman energy ω_z^n . Changing I_z by one unit also alters the Rabi frequency, and so the dressed state splitting (i.e. the ladder is again anharmonic). However, since the hyperfine shift of a single nuclear spin flip (which is of order 1 MHz [238]) is much smaller than the Rabi frequency, this can be neglected.

We depict the level scheme in Fig. 4.10 (a,b); in this picture, when the Rabi frequency is different to the nuclear Zeeman energy, states of different I_z are separated in energy, which impedes their coupling. However, when the Rabi frequency matches the nuclear Zeeman energy, states of different I_z are brought into resonance. This configuration allows states of different I_z to couple together via the non-collinear hyperfine interaction. This type of interaction, known as a Hartmann-Hahn resonance [239], corresponds to a state transfer from the electron to the nuclear ensemble, and in our case leads

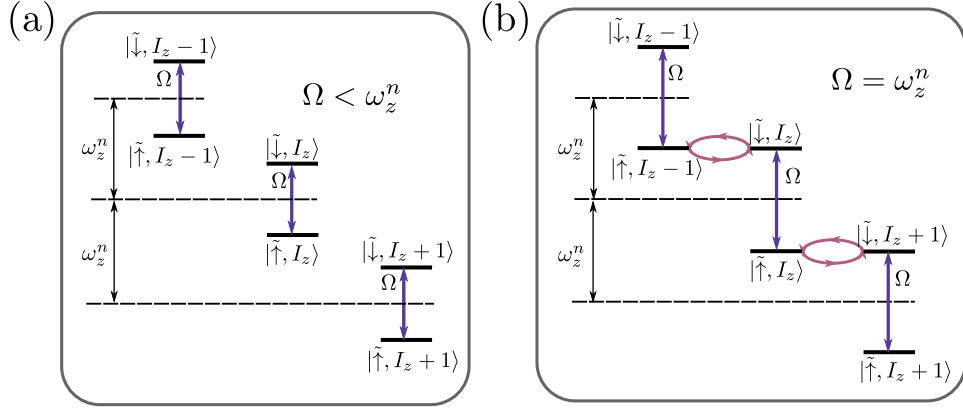


Figure 4.10: Electro-nuclear level diagram schematic in the dressed state picture, when (a) the Rabi frequency Ω is less than the nuclear Zeeman energy ω_z^n and (b) when they are equal.

to an enhanced decay rate and reduced visibility under Rabi oscillations. In this way we can tune the rate of electro-nuclear interaction with our drive.

In order to include these resonances in our model, we use the nuclear spectral densities plotted in Fig. 4.11 (a). These represent the number of transitions which exist at a given frequency; a depiction of their physical origin is shown in Fig. 4.11 (b). Two families of transition are present, corresponding to those that change nuclear spin projection by one ($\Delta m = 1$) or two ($\Delta m = 2$) units. We include both spin $I = 3/2$ and $I = 9/2$ species, since our QD includes both (gallium and arsenic for the former, indium for the latter). In addition to the Zeeman splittings shown in Fig. 4.11 (b), the nuclear levels are also subject to quadrupolar shifts. We previously introduced the Hamiltonian in Eq. 2.30. Isolating the diagonal part, we arrive at [176]:

$$\hat{H}_Q = \sum_j B_Q^j \left\{ \frac{1}{2} \left[(\hat{I}_x^j)^2 + (\hat{I}_y^j)^2 \right] \sin^2 \theta^j + (\hat{I}_z^j)^2 \cos^2 \theta^j \right\}. \quad (4.13)$$

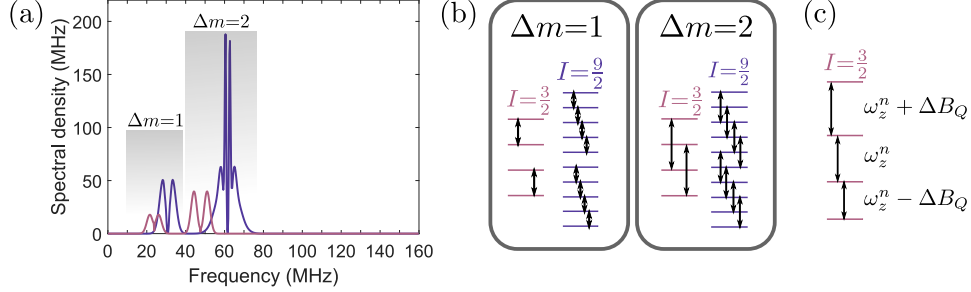


Figure 4.11: (a) Spectral density of nuclear states for indium (purple) and arsenic (pink). Transitions which change nuclear projection by 1 and 2 units are included. (b) Schematic of quadrupolar transitions which give rise to the spectral densities plotted in (a). (c) Detail of levels depicted in (b), for $I = \frac{3}{2}$. In addition to the nuclear Zeeman energy ω_z^n , levels acquire a relative quadrupolar shift ΔB_Q .

Along the direction of the magnetic field, the j -th nucleus therefore acquires a shift:

$$B_Q^j (\hat{I}_z^j)^2 \cos^2 \theta^j \quad (4.14)$$

which amounts to a shift in the energy of a nuclear level, according to the magnitude of its projection. In the simplest relevant case, where $I = 3/2$, the four levels are shifted into the configuration depicted in Fig. 4.11 (c). Here, the quadrupolar interaction alters the splitting between nuclear levels by an amount

$$\Delta B_Q = 2B_Q^j \cos^2 \theta^j \quad (4.15)$$

in the configuration depicted in Fig. 4.11 (c). This shift is the reason for the multi-peak structure, even within each I and Δm , seen in Fig. 4.11 (a).

These Hartmann-Hahn resonances correspond to coherent coupling between states of different nuclear projection. However, the presence of multi-

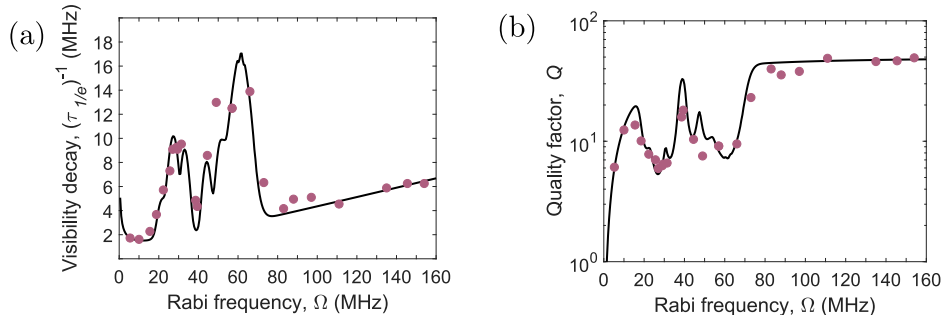


Figure 4.12: Experimentally measured (pink circles) and modelled (black curves) (a) visibility decay rate and (b) quality factor as a function of Rabi frequency.

ple nuclear species, alongside large strain inhomogeneities, mean that these resonances present themselves as an enhanced decay rate of our Rabi oscillations, as transitions to states with different nuclear projections are driven, destabilising the lockpoint of the optical cooling.

Having calculated the spectral densities, we fit to the experimentally measured decay rate by allowing the total number of nuclei, along with the quadrupolar constants and angles for both indium and arsenic, to vary. Gallium is neglected due to its significantly smaller spectral density [156]. Further, we must convolve with the ESR lineshape (which corrects the spectral selectivity of the ESR by including dephasing of the electron spin, alongside power broadening) [224]. Simultaneously including the effects of Overhauser noise, with a width constrained by an independent measurement, alongside a laser-induced spin decay, we arrive at the theory curves presented in Fig. 4.12. These display close quantitative agreement with our experimental data. We demonstrate that by tuning our Rabi frequency, we can selectively couple or decouple the electron spin from its nuclear environment.

Selective coupling to nuclear modes will be explored in detail in Chapter 5. However, for the remainder of this Chapter, we will explore the conse-

quences of decoupling on the electron spin.

4.8 Spin locking

So far in this Chapter, we have developed fast, high-fidelity, multi-axis electron spin control, and demonstrated that this can control the coupling between an electron spin and its environment of nuclear spins. This can be done by driving Rabi oscillations, as we did in Section 4.7, but there exist many other approaches. In this Section, we will utilise a continuous driving scheme known as spin locking [208, 240]. In close analogy to the results of Section 4.7, this scheme can be used both to enhance environmental coupling (where it is known as “NOVEL” [241, 242]) and to minimise environmental coupling [243]. Here, we will work in the latter regime.

The pulse sequence is depicted in Fig. 4.13, and proceeds as follows. After initialisation, the spin is rotated into the equatorial plane of the Bloch sphere using a $\frac{\pi}{2}$ pulse. The phase of the driving field is then increased by $\frac{\pi}{2}$, placing the system into one of the eigenstates of the drive (which are the dressed states). In this configuration, the spin is “locked” to be parallel to the Rabi vector. After a locking time T , remaining coherence is probed using a final $\frac{\pi}{2}$ pulse, whose phase ϕ is swept through 2π , followed by a readout pulse.

In this picture, fluctuations in the ESR manifest themselves as a detuning of the drive, which raises the Rabi vector out of the equatorial plane of the Bloch sphere. If these fluctuations in detuning happen more slowly than the Rabi frequency, the Bloch vector will remain parallel (i.e. locked) to the Rabi vector (in analogy with the action of a Landau-Zener transition); conversely if they are faster than the Rabi frequency, the Bloch and Rabi vectors will

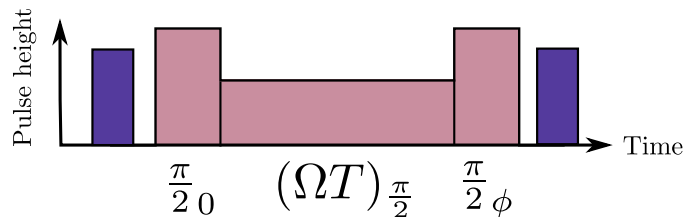


Figure 4.13: Spin locking pulse sequence. The locking pulse (at Rabi frequency Ω , and lasting for time T) is bookended by two projection pulses, the second of which has a variable phase ϕ .

no longer be parallel, and the component of the Bloch vector perpendicular to the Rabi vector will precess (i.e. this component is unlocked). Hence, when Ω exceeds the frequencies of environmental dynamics, the system is protected from dephasing.

4.8.1 The three regimes of spin locking

We begin with an experiment to characterise the performance of spin locking with Rabi frequency. This is done using a simplified version of the sequence shown in Fig. 4.13, where we read out using a phase $\phi = 0$ (π) to probe the length of the Bloch vector parallel (antiparallel) to the resonant Rabi vector. We perform the initial and final projection $\frac{\pi}{2}$ pulses at high Rabi frequency (> 100 MHz), where we previously found the highest fidelities. We then vary the Rabi frequency of the locking pulse.

As we did in Section 4.7, we can again separate the parameter space of Rabi frequency into three regimes, an example of each of which is presented in Fig. 4.14. The first, in panel (a), concerns the low Rabi frequency limit, where Ω is smaller than the nuclear Zeeman energies. Here, Ω is comparable to the Overhauser width σ , meaning that we do not fully decouple from Overhauser fluctuations. These lift the Rabi vector out of alignment with the

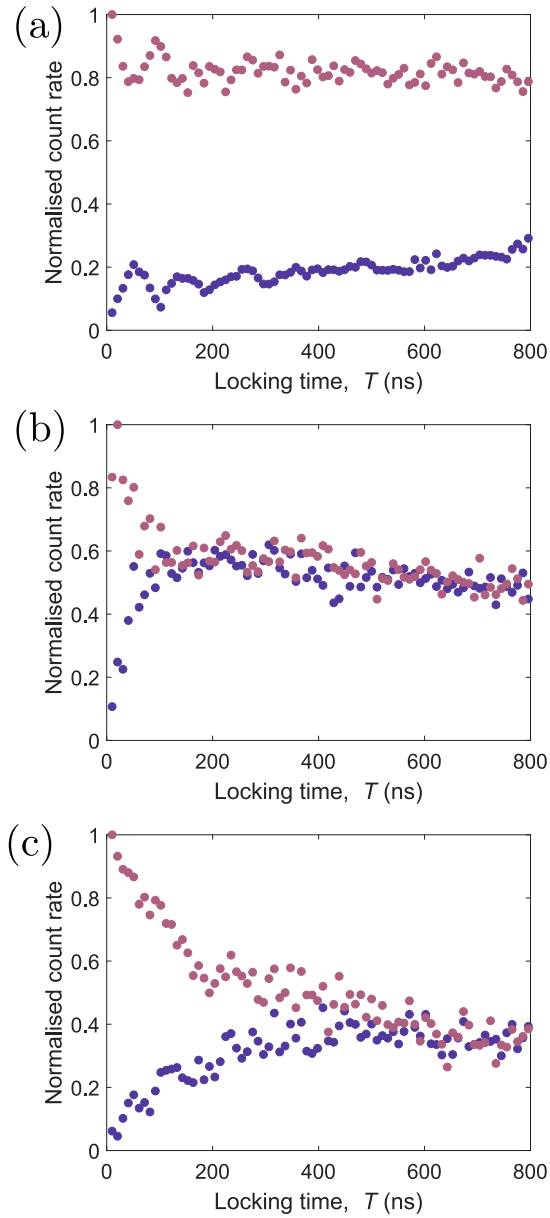


Figure 4.14: Count rate following a spin locking pulse of variable length T , read out using a phase of 0 (π) to produce the pink (purple) data points, and using a locking Rabi frequency of (a) 10 MHz, (b) 62 MHz, (c) 125 MHz.

Bloch vector, causing the Bloch vector to be driven. The resulting precession of the Bloch vector around the Rabi vector includes oscillation along the direction of the zero-detuning Rabi vector, at the (grand) Rabi frequency. Both the amplitude and frequency of these oscillations are dependent on the Overhauser fluctuation, but the phase is not. Our Overhauser-field-averaged measurement therefore displays small oscillations, approximately at the Rabi frequency. In addition to these, we observe that 60% of the initial visibility remains after 800 ns of locking.

The second regime, presented in panel (b) of Fig. 4.14, refers to the case where the Rabi frequency Ω is comparable to the nuclear Zeeman energies. The electron spin is subject to transverse noise which evolves at these frequencies as the nuclear spins undergo Larmor precession. As was previously explained, when the spin-locking Rabi frequency is commensurate with the noise frequency, the effects of the noise are enhanced. Here, the amplification of environmental noise causes a fast decay of coherence in under 50 ns.

Figure 4.14 (c) presents data taken in the regime where the Rabi frequency exceeds the nuclear Zeeman energies, where we expect the optimal performance of spin locking for the reasons outlined above. However, in stark contrast to expectation, the coherence of our quantum superposition decays within 200 ns, significantly faster than under a weak locking pulse. We will return to a discussion of this decay in Section 4.9.

4.8.2 State preservation using spin locking

The low-power regime is clearly the optimal for state preservation. To capture its behaviour, we use a simple model based on the optical Bloch equations, and average a Gaussian distribution of detunings with width fixed by

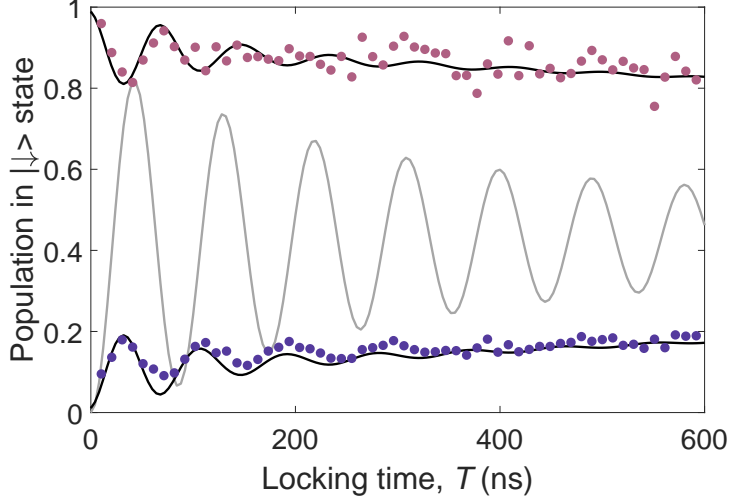


Figure 4.15: Count rate after a spin locking pulse of length T , using a readout phase of 0 (π) (pink [purple] circles), along with a model (black curve). In addition, we plot modelled Rabi oscillations at the same Rabi frequency (grey curve). Count rate is converted to population by comparing to the model.

our measurement of T_2^* (shown in Fig. 4.4). This model, presented in Fig. 4.15, closely agrees with our experimental data, using an Overhauser width $\sigma = 4.8$ MHz and a Rabi frequency $\Omega = 11$ MHz. Alongside, we plot the corresponding Rabi curve, which demonstrates the superior performance of spin locking in preserving the length of the Bloch vector.

Whilst the two models are fed identical Rabi frequencies, the oscillations which they exhibit have different frequencies. These models sum over a Gaussian spread of detunings (representative of the Overhauser field distribution). In the Rabi model, the zero-detuning oscillations have the largest amplitude, and the largest weight in the sum. Conversely, in the spin locking model, the most heavily weighted oscillations in the sum arise at finite detuning, where the oscillation frequency is higher (at zero detuning, the spin state is perfectly locked and does not oscillate). This explains the dif-

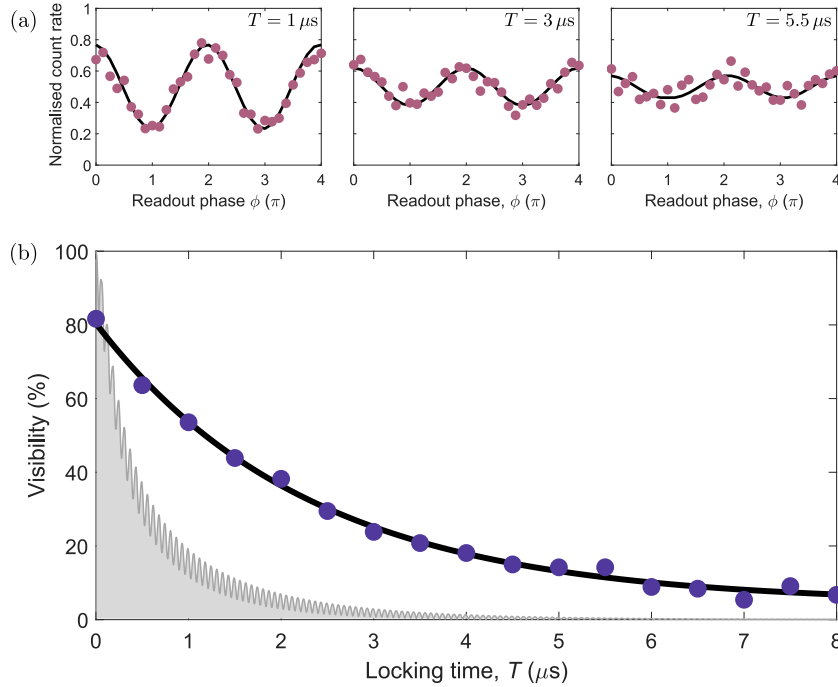


Figure 4.16: Full spin-locking decay profile. (a) Normalised count rate after the spin locking pulse sequence, as a function of the phase ϕ of the final $\frac{\pi}{2}$ pulse (pink circles). From left to right, the locking time T is $[1, 3, 5.5] \mu\text{s}$. Alongside, we fit the data with a sinusoid (black curves), and normalise the count rate by $\max(\text{fit}) + \min(\text{fit})$, allowing direct extraction of the visibility. (b) Extracted visibilities for each locking time T (purple circles). We fit these with an exponential decay (black curve), allowing extraction of the spin locking decay time of $2.3(3) \mu\text{s}$. Alongside, we plot the equivalent visibility under a Rabi drive (grey shaded area).

ference in oscillation frequency between the two models, despite the same inhomogeneous distribution of detunings.

Having confirmed the superior performance of spin locking to Rabi drive at relatively short time delays and using a simplified readout scheme, we now proceed to a full characterisation. Using the spin-locking sequence depicted in Fig. 4.13, we perform tomography of the Bloch vector as a function of locking time T , allowing us to extract a visibility; Fig. 4.16 (a) presents three such datasets. We fit these visibilities to an exponential decay in Fig.

4.16 (b), allowing us to extract a spin-locking decay time of $2.3(3) \mu\text{s}$. The short-delay visibility is limited by the ability of our microwave system to change phase on a fast timescale (i.e. its bandwidth), since the spin-locking sequence is made up of immediately consecutive pulses.

Alongside, we plot the corresponding visibility under a direct Rabi drive at the same Rabi frequency of $\Omega = 16 \text{ MHz}$ (grey curve in Fig. 4.16 [b]), which exhibits decay on a 100-ns timescale. This decay is modulated at the Rabi frequency, where decoherence due to nuclear inhomogeneities is partially refocussed at integer multiples of a 2π rotation. This measurement confirms our ability to preserve the quantum state for a longer time than would be accessible under Rabi drive.

4.9 Laser-induced spin relaxation

Throughout the experiments presented in this Chapter we observe a visibility decay rate which depends linearly on Rabi frequency, once nuclear effects have been factored out. This places a hard limit on control fidelity and restricts the decay time under both Rabi drive and spin locking. Here, we probe this decay channel further. We initialise the electron spin, after which we shine a single, far-detuned optical frequency onto the QD. After this pulse, we read the electron spin out. Any electron spin population revealed by the readout pulse must be present due to a spin relaxation (T_1) process, and varying the length T of the detuned pulse allows us to extract the rate of spin relaxation which is induced by this pulse.

In Fig. 4.17 we perform precisely that measurement as a function of the power P of the far-detuned laser pulse, and for detunings of 800 GHz and 1600 GHz from the optically excited states. We observe that the far-detuned

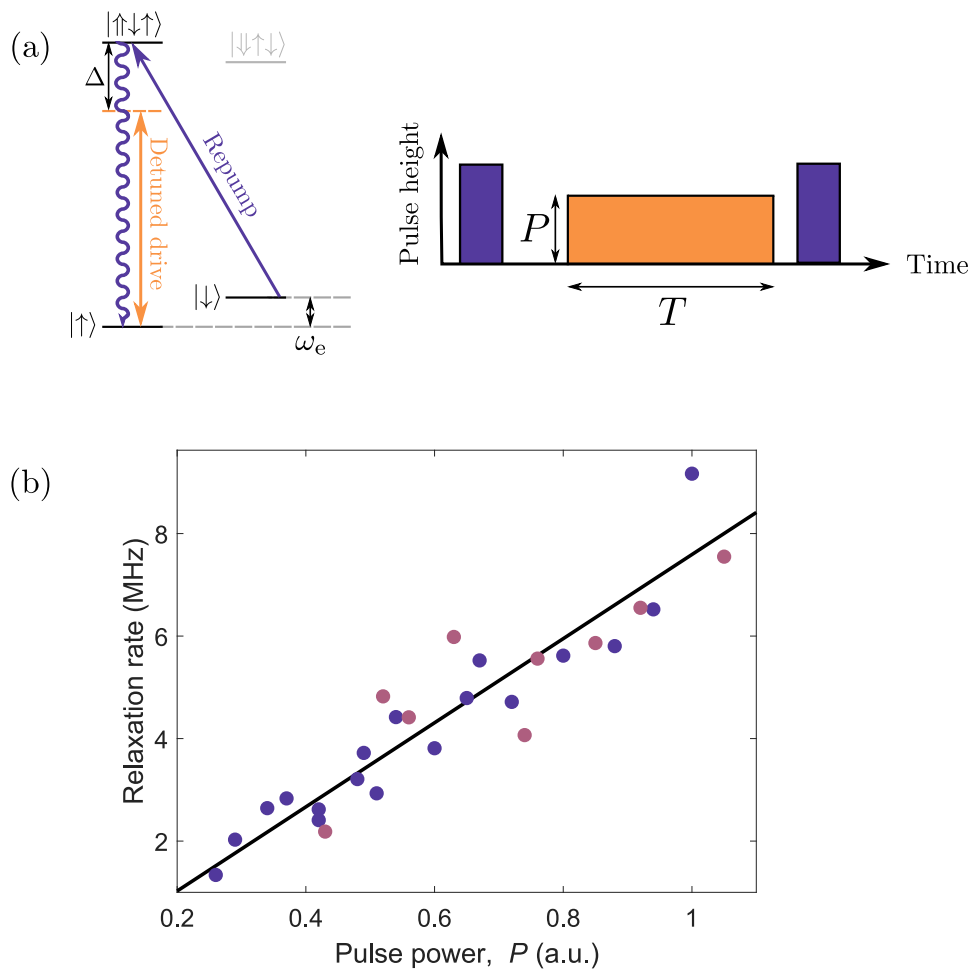


Figure 4.17: Probing optically induced spin relaxation. (a) Level scheme and pulse sequence. (b) Extracted relaxation rate as a function of detuned laser power, for a detuning $\Delta = 800(1600)$ GHz from the optically excited states (purple [pink] circles).

pulse does indeed induce a pure relaxation process, whose rate depends linearly on the power of the pulse. Further, we observe no dependence on the detuning from the optical excited states. The insensitivity to detuning necessitates a mechanism unrelated to the transitions of the QD itself. The optical generation of charges which can then become trapped inside the diode structure has been suggested as a mechanism to explain shifts in the frequency of optical lines of a QD [113]. However, a sufficiently small distance between the QDs and the blocking barrier prevents charge trapping, and our capping layer thickness of 10 nm satisfies this condition [244]. Nevertheless, optical generation of charges can cause shifts of QD resonances even in the absence of trapping [245].

This photocurrent could limit control fidelity by generating electrical noise. This is consistent with the observation that hole spin control has a lower fidelity than electron spin control, because hole spins are more sensitive to electrical noise than electron spins [156, 157]. The physical origin of this photocurrent is unclear, but minimising it is likely to be crucial for improving our spin rotation fidelities.

4.10 Conclusions & Outlook

In this Chapter we have developed and demonstrated a novel technique for electron spin control in QDs, combining high fidelities with multi-axis control and arbitrary flexibility for the first time in this system. These important capabilities allowed us to demonstrate the ability of this technique to tune the coupling rate between an electron spin and its environment. Turning this coupling off, we were able to show protection of a known quantum state for a time an order of magnitude longer than it would otherwise survive,

using a pulse sequence known as spin locking. In the next Chapter, we shall expand the possibilities for turning environmental coupling on.

Chapter 5

Quantum Correlations in a Mesoscopic Ensemble

In the previous Chapters, we married an optical nuclear spin preparation technique with an optical electron spin control technique, which enabled multi-axis, high-fidelity electron spin control. By using this capability, we saw the possibility of tuning the interactions between the electron and its nuclear environment. In this Chapter, we will explore some of the many interesting and important research directions made possible by these results. In particular, our aim will be to use our well-controlled spin qubit to probe the nuclear spin ensemble.

Here, rather than disabling environmental coupling, we drive it: we use our optical electron spin control to bring the electron spin into resonance with nuclear spin-flipping modes. We show that we can resolve these modes, which correspond to single collective excitations distributed within the nuclear ensemble. Next, we show how the interaction strength of the electron

with these modes can reveal intimate information about the nuclear spin state populations, going beyond the mean-field treatment and allowing us to fully reconstruct the nuclear population distribution. Finally, by tracking these interaction strengths as a function of an imposed nuclear polarisation, we reveal the presence of quantum correlations in the ensemble.

The data in this Chapter were taken with Clara Bachorz. Theoretical analysis was performed by Leon Zaporski. The results of this Chapter have been presented in a peer-reviewed journal article: [246].

5.1 A many-body system of nuclear spins

An isolated many-body system can play host to correlations underpinning non-equilibrium, or quantum, phases of matter [247–250]. In some cases, interactions between members of the system are sufficiently weak to be neglected, and the system can be manipulated and measured via global controls (such as NMR [208]). When interactions become important, this simplified picture is no longer accurate and the ensemble exhibits correlations to which global measurements are blind. Measurements which are sensitive to inter-particle correlations can be realised using tomography based on single-particle measurements, possible in quantum gas microscopes [251, 252] (via spatial resolution) and dilute central-spin systems [253–259] (where individual nuclei can be spectrally resolved and coherently addressed via a proxy electronic spin). Another avenue to correlation-sensitive measurement is by exploiting collective excitations of the ensemble [260] (of which polaritons [261] and magnons [262] are examples), which can be used to uncover information about the state of the particles which together make up the ensemble [263]. This measurement approach is particularly well-suited to

dense ensembles, where single-particle resolution is not achievable; in this case, coupling the system to a proxy qubit allows it to be conveniently manipulated and probed. This type of coupling is achieved in a number of systems, including the interface of a superconducting qubit with an electronic [264] or a nuclear [265] spin ensemble, a single photon coupled to an ensemble of artificial atoms via cavity quantum electrodynamics [266–268], a Rydberg polariton in a cloud of atoms [269, 270], and a single electron spin coupled to a dense nuclear spin ensemble [30, 163].

In their own right, nuclear spins constitute a fundamentally interesting and attractive platform for studying quantum physics. Their intrinsically long-lived coherence [161, 271–273] coupled with their potential for high-fidelity quantum control [254, 255, 274, 275] means that they have been the focus of a wide range of proposals, including for quantum information processing [276–279], quantum error correction [253], quantum simulation [280], and quantum memory [171, 281–287].

As we previously described in detail in Section 2.6, in the particular case of a semiconductor QD, the importance of interactions between the electron spin and its environment of nuclear spins has been established by over a decade of research [163, 288, 289]. The unique one-to-all coupling between the electron spin and nuclear spins found in a QD makes it a system of particular interest for studying many-body effects, and the interaction with the central electron spin has been proposed as a platform for the generation of entanglement and spin squeezing in the nuclear ensemble [159, 290, 291].

Experimentally, despite this enormous potential, nuclear spins in QDs have hitherto manifested themselves as an obstacle to ideal quantum control (as we saw in Chapters 3 & 4) and as a source of decoherence. Understanding their dynamics is therefore foundational to exploiting the nuclear spins as a

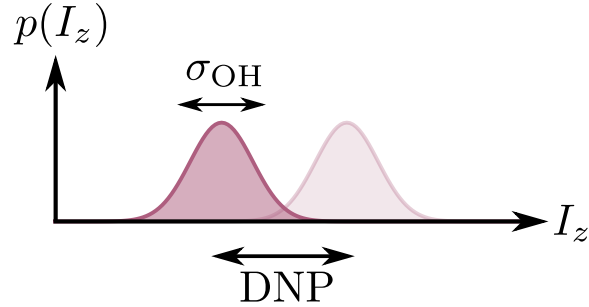


Figure 5.1: Nuclear spin distribution schematic. On an axis of nuclear polarisation I_z , the nuclear distribution is described by a set of probabilities $p(I_z)$ having a width described by the Overhauser width, σ_{OH} . DNP shifts the centre of the distribution.

quantum resource.

The nuclear spins present themselves as a frustration to electron spin dynamics via two main channels. The first of these refers to fluctuations in the nuclear spin polarisation, which give rise to a corresponding fluctuation on the ESR via the Overhauser shift, placing a limit on electron spin coherence. The second of these is dynamical nuclear polarisation (DNP), which causes the Overhauser shift to change over the course of an experiment, frustrating attempts to probe the undressed behaviour of the electron spin. Because the electro-nuclear interaction is hyperfine, it depends on nuclear polarisation, and the nuclear state is therefore typically described in polarisation space. The distribution which describes the nuclear spin state, depicted schematically in Fig. 5.1, has a width - parametrised by the Overhauser width - and a centre - the average polarisation. In this way, many of the effects arising from a complex many-body interaction with $\sim 10^5$ nuclear spins are captured using just two parameters, describing their mean-field interaction with the electron spin.

Mitigating the unfortunate consequences of the nuclear spin distribution for the electron spin dynamics has followed a wide variety of routes. Firstly,

the problem of a large Overhauser width can be sidestepped by protecting the electron spin from its environment using decoupling control sequences (as in Refs. [156, 157] and Section 4.8, for example). These approaches are based on filtering the effects of low frequency environmental noise, leaving the inhomogeneous dephasing time (T_2^*) untouched, but allowing the longer, homogeneous dephasing time (T_2) to be accessed. However, an alternative approach is to reduce the Overhauser width itself, by addressing the nuclear spins. These techniques, often referred to as “narrowing” or “cooling”, have allowed the demonstration of a spin coherence extension by an order of magnitude in QDs [176, 185, 229, 292, 293], and we previously exploited one such technique to lead to the results of Chapter 4.

Secondly, and similarly, the effects of DNP can be minimised using a broad range of techniques. Maintaining an average electron spin polarisation close to zero largely prevents the build-up of nuclear polarisation (as we saw in Section 3.9, and as used in Ref. [156]), and active stabilisation of the average nuclear polarisation also prevents large changes in Overhauser shift. The nuclear polarisation itself can also be manipulated, often by driving via the electron [178, 294–301], and the generation of nuclear polarisation has in turn been proposed as a technique for enhancing electron spin coherence [302, 303].

In semiconductor QDs, direct nuclear spin manipulation has also been demonstrated, using global radio-frequency control fields to address nuclear magnetic resonances [304–307]. This approach has allowed structural analysis of the QD [299, 308], as well as direct probing [309] and extension [310] of nuclear spin coherence in QDs. Beyond, NMR control has allowed the nuclear spin distribution to be described not only in terms of the average polarisation but using average populations of spin projections [311], and

even the exploitation of the nuclear ensemble as a two-qubit quantum register [207].

Despite this experimental *tour de force*, there remain several outstanding challenges in the study of nuclear spins in QDs. To date, measurements of the nuclear spin ensemble have relied on detecting shifts in the electron spin splitting - mean-field Overhauser shifts. This has given numerous insights into electro-nuclear dynamics [163, 180, 312], including species-resolved decomposition of the mean-field dynamics via Hahn-echo spectroscopy [156, 189, 313], and even resolution of quantum back-action of single electron spins on the nuclei [314] and the Overhauser shift of a single nuclear spin flip [238]. However, no QD nuclear spin probing technique which has sensitivity to inter-particle correlations has been developed, and this leaves a tantalising gap between experimental possibilities and the exciting predictions of correlated, or even entangled, many-body states which could be generated via the QD electron. Tackling some of these challenges will be the focus of this Chapter.

Throughout the work presented in this Chapter, we employ the nuclear spin preparation technique described in Section 4.4. This technique has the dual benefit of reducing the amplitude of quasi-static nuclear spin fluctuations, enhancing the electron spin inhomogeneous dephasing time, and of stabilising the nuclear polarisation to reduce the effects of DNP.

5.2 Nuclear magnons in quantum dots

Our nuclear spin preparation technique is based on a driven coupling between states of different nuclear polarisation, as we show in Fig. 5.2. We can

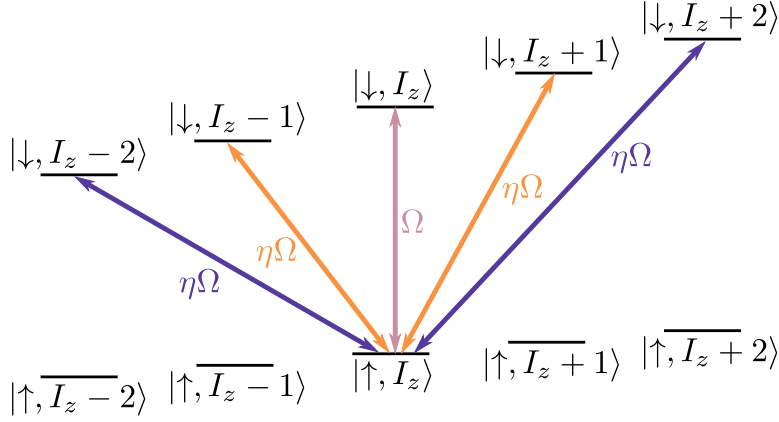


Figure 5.2: Electro-nuclear ladder of states. From the starting state $|\uparrow, I_z\rangle$ arrows indicate allowed transitions which flip the electron spin alone (pink arrow), or accompanied by a single (orange arrows) or double (purple arrows) nuclear spin flip. Nuclear spin-flipping transitions are reduced in strength relative to the ESR by a factor of η .

express this coupling via the following correction term to the Hamiltonian:

$$\hat{V}_Q'' = -2\Omega\hat{S}_y \sum_j \frac{A^j B_Q^j}{(\omega_z^n)^2} \left[\frac{1}{2}(\hat{I}_x^j \hat{I}_y^j + \hat{I}_y^j \hat{I}_x^j) \sin^2 \theta^j + (\hat{I}_z^j \hat{I}_y^j + \hat{I}_y^j \hat{I}_z^j) \sin 2\theta^j \right]. \quad (5.1)$$

Terms proportional to $\sin 2\theta$ allow single nuclear spin flips, and terms in $\sin^2 \theta$ allow double nuclear spin flips.

Using this preparation technique, we realise an Overhauser width an order of magnitude smaller than the bare, unprepared QD [176]; in fact, this is comparable to those achieved previously using alternative narrowing techniques [185]. The new, cooled, Overhauser distribution has a width of a few MHz, which is exceeded by the nuclear Zeeman energies (which are a few tens of MHz [156]). We have therefore entered the regime where the watershed possibility of observing modes associated with single nuclear spin flips becomes possible.

The final piece in the puzzle is a method for driving these transitions. In order to do this, we need a driving technique with spectral selectivity on the scale of the ESR width (a few MHz). Whilst this could in principle be effectuated by a sufficiently long train of ultrafast electron spin rotations, precisely timed to coincide with the nuclear Zeeman frequencies, this is in practice impossible for the reasons outlined at length in Section 3.1. We therefore, again, rely on the virtues of our novel electron spin control technique, whose spectral selectivity makes such a measurement straightforward.

After preparing the nuclear spins and electron spin, we drive the system with a pulse whose length and (two-photon) detuning we control. Since we wish to resolve features separated by a few tens of MHz, we must work with a small Rabi frequency in order to avoid power broadening. Following this pulse, we track the response of the system by repumping the electron spin; the resulting count rate constitutes our signal.

At a drive time close to the π time of the ESR, we reveal the data presented in Fig. 5.3 (a); the ESR lineshape is clear. Its width is a convolution of the electron spin inhomogeneous dephasing rate and the Rabi frequency, and here is fitted to 20(2) MHz, below the nuclear Zeeman energies (which at our magnetic field of 3.5 T are 25.27 MHz for arsenic and 32.66 MHz for indium). In addition, we guide the eye with dashed lines to mark these energy scales relative to the ESR; the sufficiency of our resolution is again apparent.

Performing the same measurement at a longer drive time reveals the data shown in Fig. 5.3 (b). Alongside the principal ESR, we now resolve four nuclear spin-flipping transitions, distinguished by their relative detuning from the ESR; we find resonances detuned by single and double units of the nuclear Zeeman energies. Figure 5.3 (c) displays the full dependence

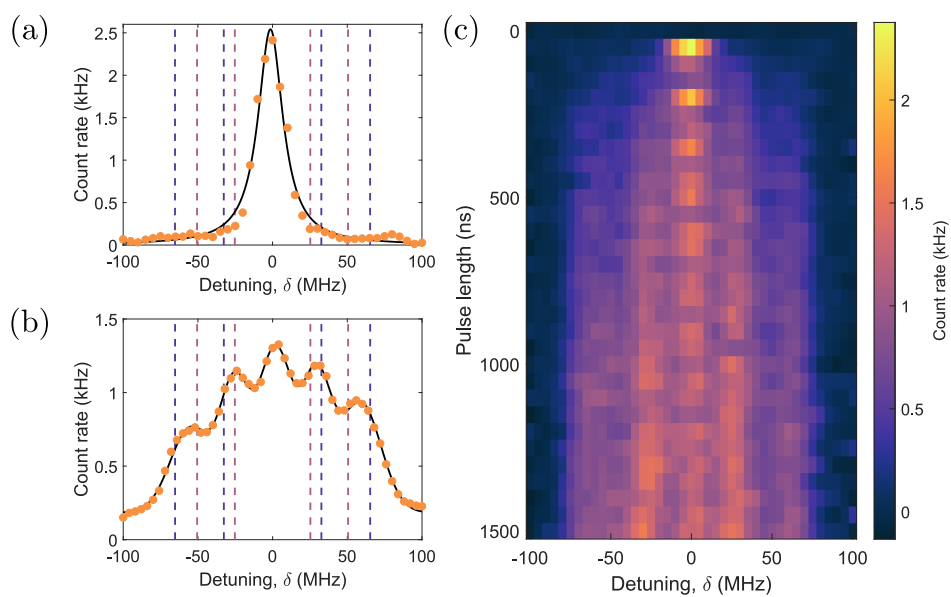


Figure 5.3: Count rate as a function of detuning δ from the ESR, at a drive time of (a) 50ns and (b) 1000ns. Dashed lines indicate $\pm 1, 2$ units of the arsenic (pink) and indium (purple) Zeeman energy. Solid curves are fits, based on a single (quintuple) Lorentzian (a [b]). (c) Count rate as a function of detuning and drive time.

of the system on pulse length and detuning, from which linecuts are taken and presented in panels (a,b). In addition to Rabi oscillations of the central ESR, the emergence of well-resolved nuclear spin-flipping modes is apparent.

Crucial to this experimental observation is the fact that the electron cannot distinguish individual nuclear spins; its Gaussian wavefunction couples close-to-homogeneously to N of $\mathcal{O}(100,000)$ nuclei in the QD. For this reason, these nuclei all partake in the nuclear spin-flipping mode, meaning that the single (or double) nuclear spin flip is distributed across the ensemble. This leads to a degeneracy factor $\sim \sqrt{N}$, collectively enhancing the interaction strength and rendering these processes observable. This leads to a prefactor of $\eta \sim \frac{AB_Q\sqrt{N}}{(\omega_z^2)^2}$ on the nuclear spin-flipping processes when compared to the ESR; taking literature values, we find $\eta \sim 0.1$ [176].

The collective nature of these spin excitations motivates our use of the term “magnon” from hereon in. However, in contrast to magnons in ferromagnetic materials, our magnons are mediated by the central electron spin. A collective nuclear spin excitation, before these results, had only been observed via ensemble measurements of atomic gases [315] and magnetic materials [316,317].

The observation of a collective interface between the QD electron spin and nuclear spins constitutes a landmark result for the study of QD spin physics, as well as for the development of quantum technologies using QDs. We have built on these results by demonstrating the coherent nature of interactions between the electron spin and magnons [176,238], and by showing that the electron spin can be deployed as a sensor to detect single magnons via their Overhauser shift [238]. Of particular relevance to the remainder of this Chapter, our observation of magnons opens a new window into the state of the QD nuclear spins.

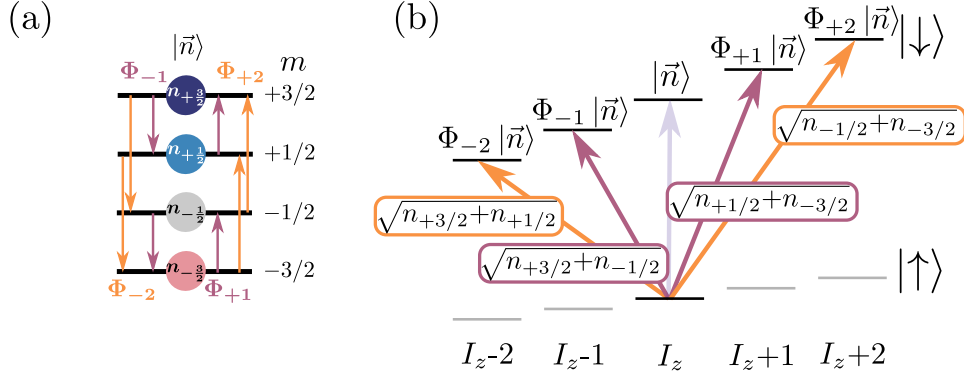


Figure 5.4: (a) Nuclear population exists in a four-level space spanned by the four possible spin projections m of a spin-3/2 nucleus. Within this manifold, magnonic transitions which increase or decrease m by one (pink arrows) or two (orange arrows) units are allowed by the Φ operators, as depicted. (b) When starting from the same initial state, different magnon modes are collectively enhanced by different subsections of the population distribution.

5.3 Magnons as a measurement technique

As we saw in the introduction to this Chapter, single collective excitations [260] can be used to reveal information about the state occupied by the underlying particles [263]. Here, we will exploit our single-magnon transitions to do exactly that.

The nuclear ensemble of a QD is made up of indium, arsenic, and gallium, all of which are spinful ($I = 9/2$ for indium, $I = 3/2$ for gallium and arsenic). We parametrise each species using the populations of each of its Zeeman-split spin-states: $|\vec{n}\rangle = (n_{3/2}, n_{1/2}, n_{-1/2}, n_{-3/2})$ (Fig. 5.4).

From the electron's indiscriminate view of the nuclei, the nuclei combine to give the Overhauser shift:

$$\delta_{\text{O}} = \frac{3}{2}A^{\text{As}}\mathcal{I}_z^{\text{As}} + x\frac{9}{2}A^{\text{In}}\mathcal{I}_z^{\text{In}} + (1-x)\frac{3}{2}A^{\text{Ga}}\mathcal{I}_z^{\text{Ga}}. \quad (5.2)$$

$\mathcal{I}_z^j \in [-1; 1]$ is the species-specific fraction of the maximum polarisation (which occurs when all spins of that species have projection $m = I$). A^j indicates the hyperfine constant for species j ($A^{\text{As}} = 11.1 \text{ GHz}$, $A^{\text{In}} = 13.5 \text{ GHz}$, $A^{\text{Ga}} = 9.2 \text{ GHz}$), and x is the concentration of indium. We use I_z to refer to the ensemble polarisation, over all species. For the case of a nuclear state which contains no coherences [156, 178, 208, 232, 294–298, 300], we can relate the interaction Rabi frequency of each of the four magnon modes to the underlying single-particle spin-state populations $|\vec{n}\rangle$:

$$\begin{aligned}
\Omega_{+1} &= \alpha_1 \sqrt{n_{-3/2} + n_{+1/2}} \\
\Omega_{+2} &= \alpha_2 \sqrt{n_{-3/2} + n_{-1/2}} \\
\Omega_{-1} &= \alpha_1 \sqrt{n_{+3/2} + n_{-1/2}} \\
\Omega_{-2} &= \alpha_2 \sqrt{n_{+3/2} + n_{+1/2}}.
\end{aligned} \tag{5.3}$$

As shown in Fig. 5.4 (b), these expressions apply when starting in a given initial state.

It can be shown that, in the case of $I = 3/2$, the constants of proportionality are:

$$\begin{aligned}
\alpha_1 &= \sqrt{12N} \Omega \sin 2\theta \frac{aB_Q}{2\omega_n^2} \\
\alpha_2 &= \sqrt{12N} \Omega \cos^2 \theta \frac{aB_Q}{4\omega_n^2}
\end{aligned} \tag{5.4}$$

for N nuclei participating, an ESR drive Rabi frequency Ω , quadrupolar angle θ , hyperfine constant per nucleus a , quadrupolar constant B_Q , and nuclear Zeeman energy ω_n [246]. Crucially, Ω_{+1} shares its constant with Ω_{-1} , and likewise for $\Omega_{\pm 2}$.

Finally, we note that this treatment is not exact for the indium nuclei

present in our QD, which have $I = 9/2$. We will discuss this in Section 5.8.

5.4 Polarising using Raman cooling

The thermal, unprepared state occupied by the nuclear spins is simply $|\vec{n}\rangle = (0.25, 0.25, 0.25, 0.25)$. In order to probe the non-equilibrium nuclear dynamics, we again use our optical preparation step. Whilst in the earlier discussion we drew the close analogy between our preparation technique and Raman cooling of atoms, there is a crucial difference between these two systems: our system can be pictured as an anharmonic (rather than a harmonic) ladder of states, where the hyperfine interaction between the electron and the nuclei alters the electron spin splitting, as a function of nuclear polarisation. This property gives us the ability to select the stable lockpoint of our feedback, simply by changing the frequency of the drive: the system is locked to the resonance condition of our drive laser, which we are free to change.

This technique, which we term “Raman dragging”, is illustrated schematically in Fig. 5.5. We begin with Raman cooling at zero polarisation, where the Raman frequency ω_R matches the electron Zeeman splitting ω_e . We then increase ω_R , which moves the stable lockpoint of the feedback function; we drive a polarisation in the nuclear ensemble, in order to maintain the resonance condition via the Overhauser shift. This effect is entirely analogous to our previous description of dragging, except that the process is driven via a microwave-frequency transition (the ESR) rather than an optical one.

In order for the system to follow the drive, we must alter ω_R slowly for the nuclei to stay locked to our feedback. We find experimentally the optimum ramp rate for ω_R as 0.04 GHz s^{-1} , meaning that reaching our maximum

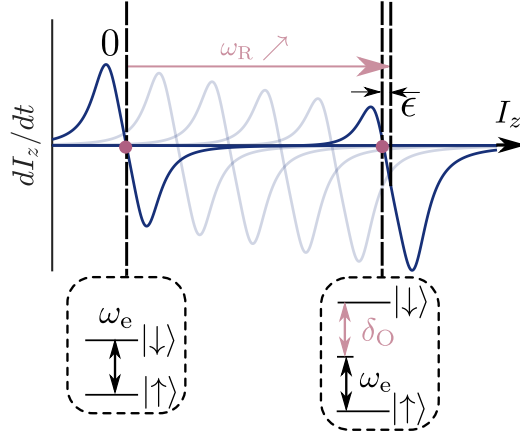


Figure 5.5: Raman dragging schematic. Our Raman cooling technique generates a feedback function (blue curves), which pump the nuclei towards a stable lockpoint defined by its polarisation I_z (pink circles). Increasing the frequency of the Raman cooling, ω_R , moves the stable lockpoint, causing the generation of an Overhauser shift δ_O in order to maintain the resonance condition.

Overhauser shift of 13.2 GHz takes 5.5 minutes. After this routine, we can perform multiple measurements without losing the nuclear polarisation by alternating a probe sequence (of a few μs) with a feedback sequence (which is ten times the length of the probe sequence). Such an alternating cycle ensures that we stay at the desired polarisation well beyond the intrinsic nuclear spin relaxation time, and avoids backaction of our measurement on the nuclear state. Further, we monitor the Raman fluorescence from the feedback sequence during our experiment, only re-polarising from zero when the lockpoint is lost i.e. when the Raman fluorescence disappears. In this way, we can hold the system at finite polarisation for hours at a time.

The action of our Raman cooling is in competition to nuclear diffusion processes. As we polarise the system, diffusion becomes directional: the system prefers to return to its equilibrium configuration, at zero polarisation. This causes the feedback function to become asymmetric when at non-zero

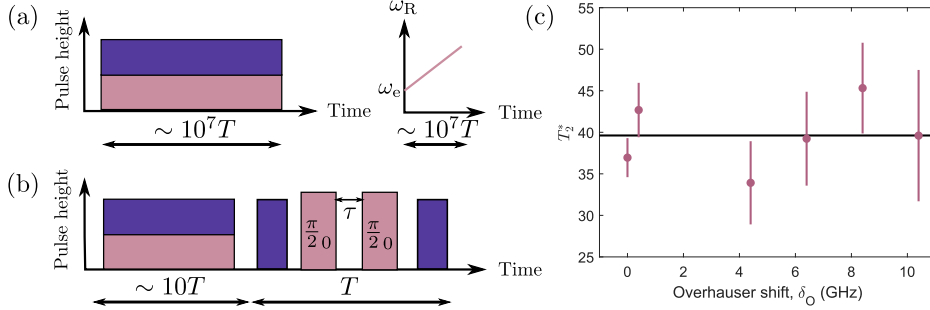


Figure 5.6: (a) Polarisation pulse sequence. Raman cooling, during which the system is driven with Raman (pink) and repump (purple) lasers (left panel), is used to polarise. During this stage, the frequency of the Raman drive ω_R is swept linearly from ω_e up $\omega_e + \delta_O$. (b) Ramsey measurement sequence. The system is held at finite polarisation by Raman cooling, and is probed using Ramsey interferometry in order to extract T_2^* . (c) Cooling performance, characterised using T_2^* , as a function of Overhauser shift. The black curve is a constant fit with a value of 39(4) ns. Error bars indicate 66% confidence intervals.

polarisation, as depicted in Fig. 5.5. At some polarisation, the diffusion rates exceed the Raman locking rates and the stable point disappears (a bifurcation).

We first characterise the performance of Raman cooling over our range of experimentally accessible polarisations, by measuring the electron spin T_2^* . The resulting data are presented in Fig. 5.6; we find roughly constant ESR width, indicating that introducing a finite polarisation does not significantly impede the performance of Raman cooling.

5.5 Probing magnon asymmetry

With this established, we proceed to measure the magnon spectrum over our range of experimentally accessible polarisations. In order to do this, we use the polarisation sequence described above to drag the system to a finite polarisation. From there, we use a drive pulse of length $1 \mu\text{s}$ and of

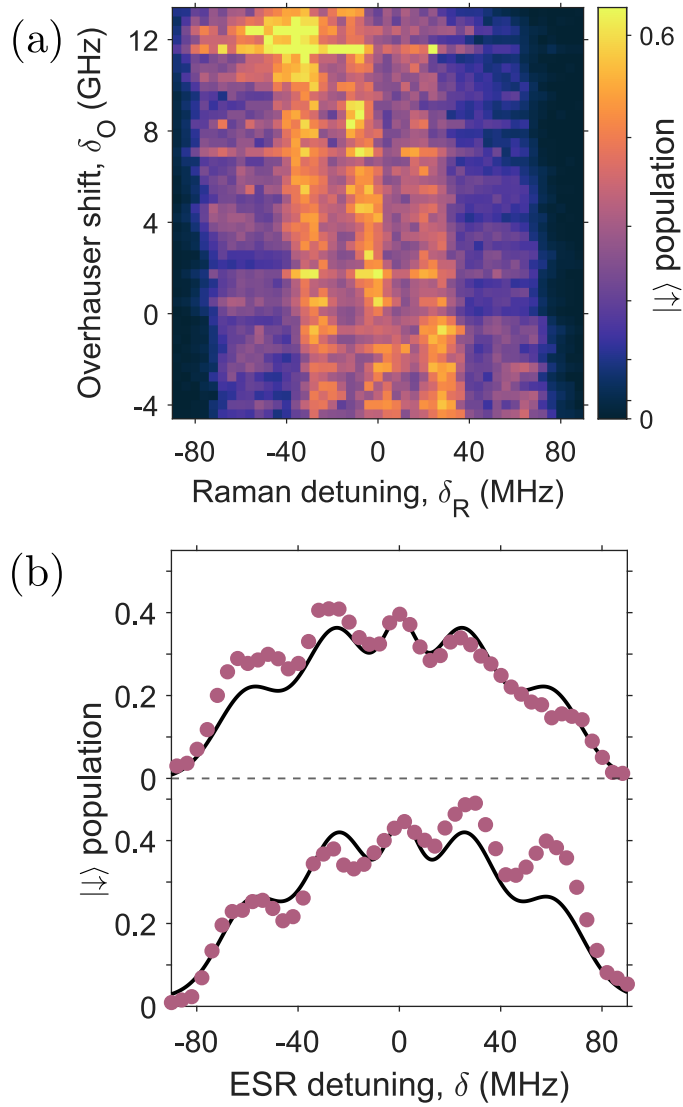


Figure 5.7: (a) Electron $|\downarrow\rangle$ population, read out following a polarisation sequence generating an Overhauser shift δ_O and a drive pulse of length $1\mu\text{s}$ and detuning δ_R relative to the end of the polarisation sequence. (b) Linecuts from data in (a) taken at $\delta_O = 7.6$ (-4.4) GHz (top [bottom]). The solid black curve is a fit to the spectrum at $\delta_O = 0$. In this panel, the shift in lockpoint evident in (a) has been subtracted i.e. our detuning δ is referenced to the ESR, not the preparation.

Raman detuning δ_R relative to the Raman frequency ω_R used to hold the system at polarisation. Reading the population after this drive pulse reveals the data which we present in Fig. 5.7 (a). Indeed, we see that we remain sideband-resolved throughout the range of Overhauser shifts probed here. This allows two striking features to emerge.

The first is an offset, ϵ , of the centre of the spectrum, proportional to the Overhauser shift. The origin of this offset is depicted in Fig. 5.5: at finite polarisation, the feedback curve becomes asymmetric, because diffusion processes preferentially bring the system back to its thermal, unpolarised state. This asymmetry causes the stable lockpoint of the system to be offset away from the one defined precisely by the Raman frequency ω_R , and here amounts to a few-MHz correction when at a few-GHz Overhauser shift.

The second feature, which we highlight in Fig. 5.7 (b), is an asymmetry in the spectrum. When at negative Overhauser shift, magnon modes which increase polarisation appear more prominent in the spectrum, whilst at positive Overhauser shift the opposite is true. This asymmetry arises due to the imbalance in nuclear spin-state populations which is present at finite polarisation.

In order to exploit the relations in Eq. 5.3, we must extract the interaction Rabi frequencies from these data. We first verify explicitly that sideband height can indeed be translated to Rabi frequency by probing magnonic transitions in the coherent regime [176]. Here, we access that regime by increasing our Rabi frequency in order to exceed inhomogeneities. We then tune the detuning of the drive pulse to match the grand Rabi frequency with the nuclear Zeeman energy. Figure 5.8 presents the time-dependent signal which we obtain. When at positive polarisation (Fig. 5.8 [a]) the magnon mode which corresponds to a more prominent peak in the spectrum (inset),

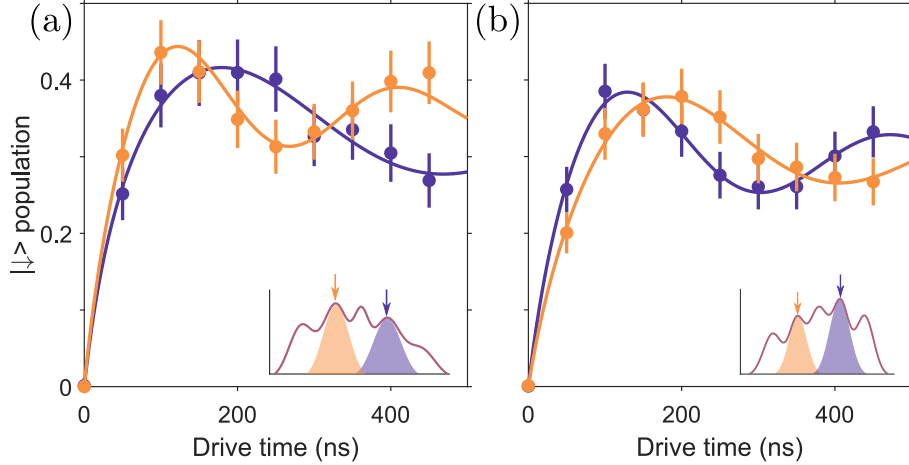


Figure 5.8: Electron $|\downarrow\downarrow\rangle$ population as a function of drive time T for a pulse which is resonant with the positive (negative) first sideband (purple [yellow] circles), as indicated by the inset schematic. Solid curves are fits of the form $\left\{-a\left(1 - \frac{x}{b+x}\right) \cos(2\pi[cx + d]) + e\right\}$. (a) $\delta_O > 0$. (b) $\delta_O < 0$.

reducing the polarisation, exhibits a faster exchange. Conversely, when at negative polarisation (Fig. 5.8 [b]), the polarisation-increasing magnon mode is preferred. This result demonstrates the qualitative correspondence of peak height to Rabi frequency. Next, we will quantify this correspondence.

5.6 Species-resolved spin-state reconstruction

In Eq. 5.8, we gave an expression for fractional polarisation \mathcal{I}_z in terms of asymmetry. In fact, this expression is true for each species which exists in our system - indium, gallium, and arsenic. If we can resolve magnon modes for each species, we can infer species-specific fractional polarisations, which then combine to give the total Overhauser shift according to Eq. 5.2.

Magnon modes for these species are split by a few MHz at our external field ($\omega_z^{\text{As}} = 25.27$ MHz, $\omega_z^{\text{In}} = 32.66$ MHz, $\omega_z^{\text{Ga}} = 35.77/45.43$ MHz). In

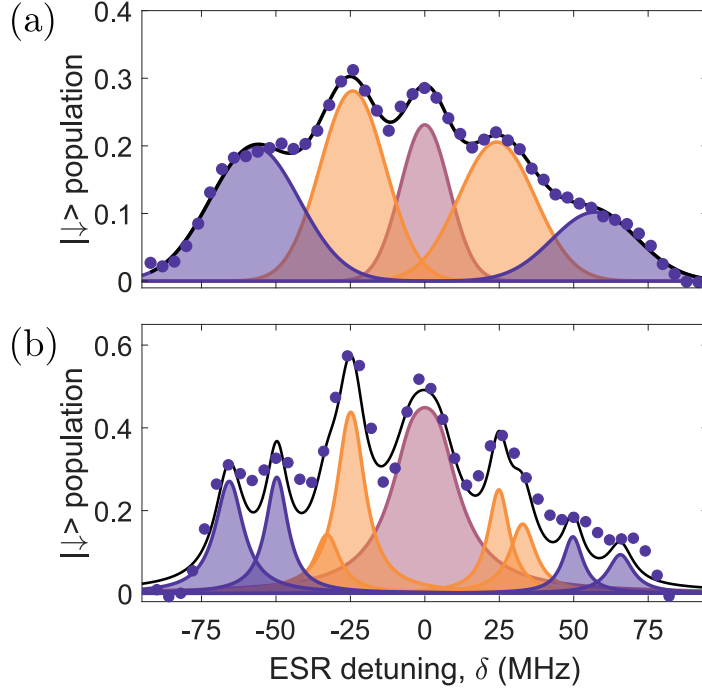


Figure 5.9: (a) Magnon spectrum. Data points (purple circles) are fitted (black curve) using a function consisting of five separate Lorentzians, for the ESR (pink curve), first sidebands (orange curves) and second sidebands (purple curves). (b) Magnon spectrum, after deconvolution using a Wiener filter. Data points (purple circles) are fitted (black curve) using 9 independent two-level systems (coloured curves, colour coding as for [a]).

order to extract species-specific information by resolving these features, we must include a further post-processing step. We have independently measured the Overhauser width using free induction decay (presented in Fig. 5.6) to be 7 MHz. This informs the construction of an optimised Wiener filter [318] which removes faithfully the inhomogeneous broadening from the spectrum. The result of this process is depicted in Fig. 5.9 (b): we reveal doublet structures contained in each of the four magnon clusters seen so far corresponding to species-specific magnon modes for indium and arsenic.

As we previously mentioned, in order to achieve this resolution, we must

work in the regime of low Rabi frequency. Under this condition, magnon transitions are overdamped by (electronic and nuclear) dephasing processes, as is apparent from the data in Fig. 5.3. We treat each magnonic mode as a two-level system with a fixed dephasing rate which is fixed by an independent measurement (the data in Fig. 5.3), allowing us to fit a lineshape to each mode independently; this process leads, as an example, to the model curves shown in Fig. 5.9. In this way, we extract an exchange frequency $\Omega_{\pm k}$ for each of the eight magnonic modes present in the deconvolved spectrum.

We introduce a dimensionless parameter ν_k (for $k = 1, 2$) which we term the asymmetry:

$$\nu_k = \frac{\Omega_{-k}^2 - \Omega_{+k}^2}{\Omega_{-k}^2 + \Omega_{+k}^2}. \quad (5.5)$$

The fortuitous combination of populations in Eq. 5.3 now becomes clear: linear combinations of ν_1 and ν_2 correspond to population differences in the nuclear ensemble:

$$\begin{aligned} n_{+3/2} - n_{-3/2} &= -\frac{1}{2}(\nu_2 + \nu_1) \\ n_{+1/2} - n_{-1/2} &= -\frac{1}{2}(\nu_2 - \nu_1). \end{aligned} \quad (5.6)$$

Up to now, the nuclear ensemble has exclusively - with two notable exceptions [207, 311] - been described in terms of its fractional polarisation, which we denoted \mathcal{I}_z . We can make a straightforward connection to this quantity by linearly combining these fractional populations, with the appropriate weights:

$$\mathcal{I}_z^* = \frac{2}{3} \left[\frac{3}{2}(n_{+3/2} - n_{-3/2}) + \frac{1}{2}(n_{+1/2} - n_{-1/2}) \right] \quad (5.7)$$

and the rearrangement in terms of asymmetries follows naturally:

$$\mathcal{I}_z^\star = -\frac{1}{3}(2\nu_2 + \nu_1). \quad (5.8)$$

We use \star to highlight that this definition of \mathcal{I}_z^\star is reconstructed from asymmetry; in the case of a thermal state, this definition is precisely equivalent to the previous one (where \mathcal{I}_z is the fraction of the maximum polarisation), $\mathcal{I}_z^\star = \mathcal{I}_z$.

We therefore see that by measuring the interaction Rabi frequency of a magnon, we can infer information about the nuclear ensemble which goes beyond the mean-field treatment: we find \mathcal{I}_z^\star , but also the population imbalances within the $|m| = 3/2$ and $|m| = 1/2$ manifolds.

Because gallium is not visible in our spectrum and because indium has $I = 9/2$ and hence does not obey Eq. 5.3 exactly, we work with the arsenic sub-ensemble for now. This results in a direct measurement of population imbalances in the arsenic sub-ensemble, which we present in Fig. 5.10. Our results indicate that the build-up of the mean field δ_O is accounted for by an imbalance in the $3/2$ subspace, with the $1/2$ subspace remaining close to unpolarised throughout. Alongside these data, we plot the corresponding imbalances expected for a thermal distribution (dashed curves). Whilst this accurately reproduces the data for the $3/2$ subspace, the data for the $1/2$ subspace deviates from this assumption and we must reconstruct the full nuclear distribution in order to understand the relevant dynamics.

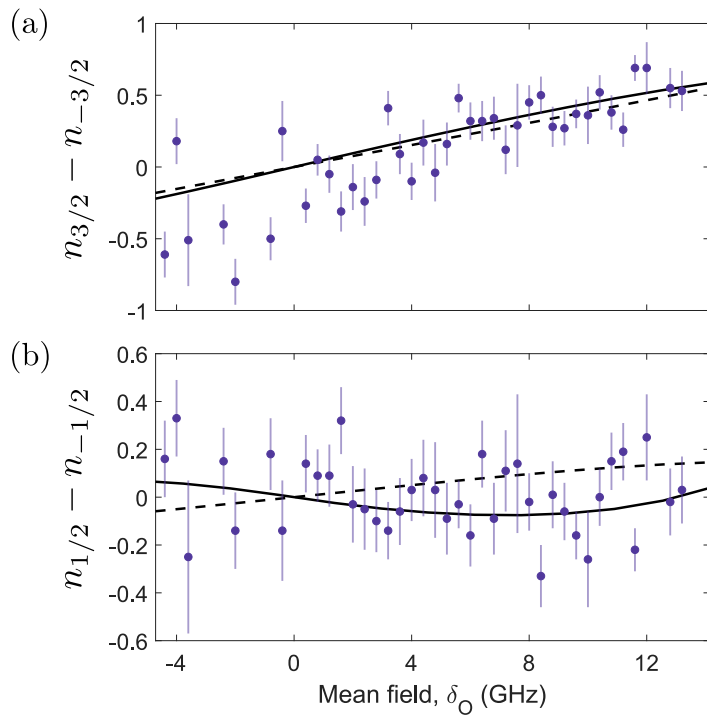


Figure 5.10: Extracted population differences in (a) the 3/2 manifold and (b) the 1/2 manifold (purple data points), alongside corresponding quantities for a thermal (dashed curves) and cooled (solid curves) nuclear state, as a function of the mean field δ_O . Error bars indicate 66% confidence intervals.

5.7 Full population reconstruction

Whilst our magnon modes allow extraction of fractional polarisation \mathcal{I}_z^* , as well as the population differences $(n_{+3/2} - n_{-3/2})$ and $(n_{+1/2} - n_{-1/2})$, they are blind to the populations \vec{n} themselves. To understand this, picture a polarisation-preserving population transfer from the 3/2 manifold to the 1/2 manifold e.g. $|\vec{n}\rangle = (\alpha, \beta, \gamma, \delta) \rightarrow |\vec{n}'\rangle = (\alpha - \epsilon, \beta + \epsilon, \gamma + \epsilon, \delta - \epsilon)$. Under this operation, no change in the magnon-derived parameters occurs, and the ensemble therefore contains further information which cannot be extracted directly using magnons. In order to reconstruct the populations \vec{n} , we must assemble a dynamical model which pits magnon excitation rates against nuclear diffusion rates. In order to do this, we use the Fokker-Planck formalism, and apply the population conservation constraint $n_{+3/2} + n_{+1/2} + n_{-1/2} + n_{-3/2} = 1$. This reduces the problem to the three-dimensional space $\vec{n}_{3D} = (n_{+3/2}, n_{+1/2}, n_{-3/2})$ and allows us to obtain the steady-state populations. The extracted population differences are shown in Fig. 5.10, where we find good agreement with our experimental data. The populations themselves are then plotted in Fig. 5.11, and compared with the equivalent quantities for a thermal state. The populations prepared by optical cooling are thermal-like only at the extrema (zero polarisation, and maximum polarisation), deviating for all intermediate polarisations. In our case, the selection rules dictated by the quadrupolar interaction (illustrated in Fig. 5.4) mean that $\Phi_{\pm 1}$ processes deplete the $m = -3/2$ and $m = 1/2$ levels when polarising to $\mathcal{I}_z > 0$, giving rise to an imbalance $(n_{+1/2} - n_{-1/2})$ which is negative, even at positive polarisations. A disagreement with the behaviour of a thermal state is a universal feature of states prepared by dragging.

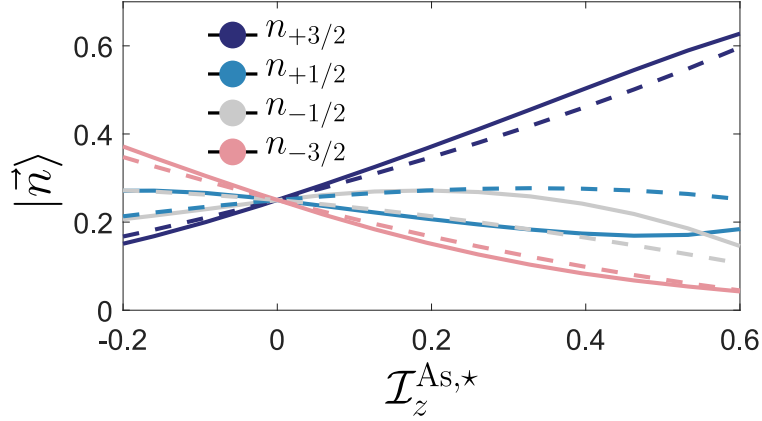


Figure 5.11: Spin-state populations in the arsenic sub-ensemble for a thermal (dashed curves) and optically cooled (solid curves) state, as a function of asymmetry-commensurate polarisation \mathcal{I}_z^* . Colour relates to population according to the inset schematic.

Our model gives us access not only to the spin-state populations, but also their widths, $\Delta\vec{n}_{3\text{D}}$. We project this three-dimensional distribution onto three sets of two-dimensional axes, and plot the results in Fig. 5.12. In the space spanned by $\vec{n}_{3\text{D}}$, our feedback mechanism pumps the nuclear state strongly towards the plane of constant \mathcal{I}_z , and weakly within this plane towards a single stable point. For this reason, the $(n_{+3/2}, n_{-1/2})$ plane, which is almost parallel to the constant- \mathcal{I}_z plane, displays a projection which is close to thermal. This is not true of the remaining two projections, which show distributions which are squeezed and tilted relative to the thermal case. This result is indicative of the spin-state correlations within our nuclear state, which therefore cannot be expressed using a separable, classical distribution.

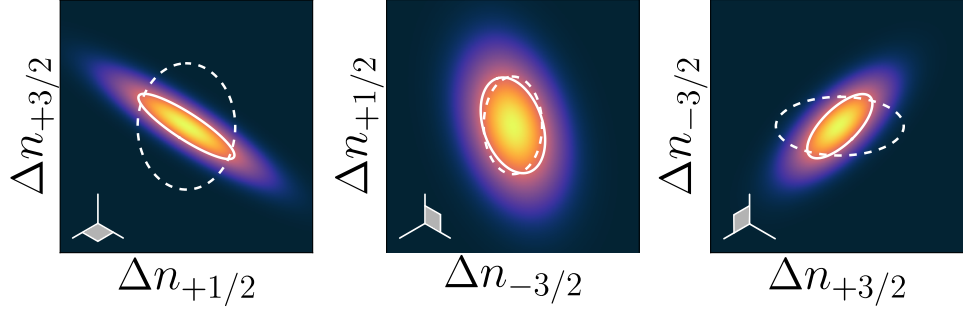


Figure 5.12: Arsenic spin-state distributions (mean subtracted) taken from a Fokker-Planck model, at an arsenic polarisation $\mathcal{I}_z^{\text{As},*} = 0.2$. The white curves represent one standard deviation, for a thermal (dashed) and cooled (solid) state.

5.8 An entangled many-body state

Up to this point, our discussion - consistent with previous works on QD systems [156, 178, 208, 232, 294–298, 300] - explicitly assumed that the nuclear state is classical. This assumption allowed the derivation of Eqs. 5.2, 5.3, 5.5, and led to intuitive relations between populations and asymmetry, via collective enhancement. In the presence of coherences, however, these relations no longer hold. We consider the case where the spin angular momenta are summed coherently such that the total angular momentum of the ensemble is the same as that of a single spin: a dark state [260]. In this scenario, the maximum mean-field would be that given by the maximal polarisation of a single spin i.e. the fractional polarisation $\mathcal{I}_z = \mathcal{O}(\frac{1}{N})$. In this configuration, no polarisation-increasing magnon transitions are possible, and we would thus reach $\nu_{1,2} = 1$ and $\mathcal{I}_z^* = 1$ in spite of the small mean field. More generally, $\mathcal{I}_z^* < \mathcal{I}_z$ is a signature of a state with reduced total angular momentum (compared to a classical state). For $\mathcal{I}_z^* > \mathcal{I}_z$, the opposite applies: this is caused by a state with increased total angular momentum.

We now cast this intuitive picture into more formal language. From

Ref. [319] we take the following inequality:

$$\langle \Delta \hat{I}_x^2 \rangle + \langle \Delta \hat{I}_y^2 \rangle + \langle \Delta \hat{I}_z^2 \rangle \geq \frac{N}{2}, \quad (5.9)$$

which applies to an ensemble of N spin-1/2 particles; $\langle \Delta \hat{I}_j^2 \rangle$ is the variance of the angular momentum projection along the direction j . The inequality in Eq. 5.9 is satisfied by all separable states, and a violation thereof implies entanglement.

Alongside, we massage the asymmetry parameter into a convenient form for this discussion. We begin by noting that the magnon exchange frequencies can be recast in terms of correlators of collective spin operators \hat{I}_\pm :

$$\Omega_\pm^2 \propto \langle \hat{I}_\mp \hat{I}_\pm \rangle. \quad (5.10)$$

The asymmetry parameter can therefore be reassembled in terms of these correlators in the following manner:

$$\begin{aligned} \nu &= \frac{\Omega_-^2 - \Omega_+^2}{\Omega_-^2 + \Omega_+^2} \\ &= \frac{\langle [\hat{I}_+, \hat{I}_-] \rangle}{\langle \{\hat{I}_+, \hat{I}_-\} \rangle} \end{aligned} \quad (5.11)$$

where $[\bullet, \bullet]$ and $\{\bullet, \bullet\}$ denote the commutator and anticommutator, respectively. Both the numerator and denominator of Eq. 5.11 can be straightforwardly written using the angular momentum commutation relations:

$$\begin{aligned} \langle [\hat{I}_+, \hat{I}_-] \rangle &= 2\langle \hat{I}_z \rangle \\ \langle \{\hat{I}_+, \hat{I}_-\} \rangle &= 2\langle \hat{I}_x^2 + \hat{I}_y^2 \rangle \end{aligned} \quad (5.12)$$

and the asymmetry parameter is then

$$\nu = \frac{\langle \hat{I}_z \rangle}{\langle \hat{I}_x^2 \rangle + \langle \hat{I}_y^2 \rangle}. \quad (5.13)$$

From here, we can easily write the variances $\langle \Delta \hat{I}_x^2 \rangle, \langle \Delta \hat{I}_y^2 \rangle$ in terms of the asymmetry parameter:

$$\langle \Delta \hat{I}_x^2 \rangle + \langle \Delta \hat{I}_y^2 \rangle = \frac{\hat{I}_z}{\nu} - \langle \hat{I}_x \rangle^2 - \langle \hat{I}_y \rangle^2. \quad (5.14)$$

Hence, using Eq. 5.9, we can use the asymmetry parameter as a formal entanglement witness:

$$\nu \leq \frac{\langle \hat{I}_z \rangle}{\frac{N}{2} - \langle \Delta \hat{I}_z^2 \rangle + \langle \hat{I}_x \rangle^2 + \langle \hat{I}_y \rangle^2}. \quad (5.15)$$

Returning to the language of fractional polarisation $\mathcal{I}_j = \langle \hat{I}_j \rangle / I_{\max}^z$ (where $I_{\max}^z = N/2$ for a spin-1/2 system), we rewrite Eq. 5.15 in the following form:

$$\mathcal{I}_z^* \leq \frac{\mathcal{I}_z}{1 - \frac{N}{2} \Delta^2 \mathcal{I}_z + \frac{N}{2} (\mathcal{I}_x^2 + \mathcal{I}_y^2)}. \quad (5.16)$$

Whilst Eq. 5.16 was derived for a spin-1/2 system, it has some important features which are independent of the spin character of the ensemble and depend only on fractional polarisations. Firstly, the denominator can only be less than one (which is where the observation $\mathcal{I}_z^* > \mathcal{I}_z$ does not imply entanglement) in a state where fluctuations in \mathcal{I}_z are $\mathcal{O}(\frac{1}{N})$. In our case, these fluctuations are reduced by a factor ~ 400 relative to the thermal case i.e. we realise $\Delta^2 \mathcal{I}_z \ll \frac{1}{N}$ and we can safely neglect this term. In this case, we can write a simple condition on \mathcal{I}_z^* , whose violation in our measurement

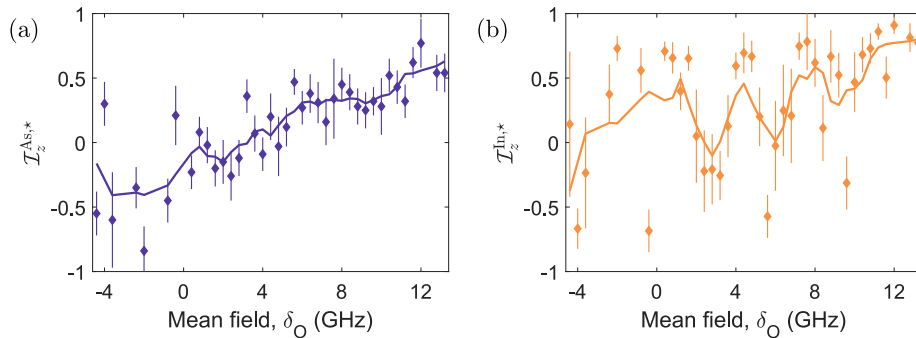


Figure 5.13: Fractional polarisation extracted from magnon asymmetry as a function of mean field δ_{O} , for (a) arsenic and (b) indium. Solid diamonds are data points, and error bars indicate a 66% confidence interval. Solid lines are calculated by passing the data points through a first-order Savitsky-Golay filter with a 1.6-GHz window.

would necessarily imply entanglement:

$$\mathcal{I}_z^* > \mathcal{I}_z. \quad (5.17)$$

In our system, since we have three nuclear species, it is expedient to work with the mean field δ_{O} , which captures the relative importance of the species-specific polarisations from the point of view of the electron (which we previously expressed in Eq. 5.2).

At this point, we must give due consideration to indium’s spin-9/2 character, which means that it does not obey Eq. 5.8 exactly. In order to navigate this, we use our definition that $\mathcal{I}_z = \mathcal{I}_z^*$ in the case of a thermal state, independent of total spin I . For a thermal state, it is straightforward to calculate \mathcal{I}_z and $\frac{1}{3}(2\nu_2 + \nu_1)$ (which equals \mathcal{I}_z^* when $I = 3/2$). The relation between these two quantities when $I = 9/2$ therefore gives the correction which we should apply to $\mathcal{I}_{z,I=3/2}^*$ in order to find $\mathcal{I}_{z,I=9/2}^*$. The correction function is at most a factor of 2 [246].

We have already directly extracted the magnon exchange frequencies for

indium and arsenic. Therefore, and using the above procedure for indium, we can straightforwardly calculate their asymmetry-commensurate polarisations \mathcal{I}_z^* , which are shown in Fig. 5.13.

Whilst magnonic modes associated with gallium are not visible in the spectrum, its contribution to the Overhauser shift cannot be neglected. We estimate its polarisation using a two-species Fokker-Planck formalism, including arsenic and gallium, and find the set of stable points $(\mathcal{I}_z^{\text{As}}, \mathcal{I}_z^{\text{Ga}})$ [246]. The relation between these two quantities is set by the strength of the feedback which is experienced by each species, decided by their relative hyperfine constants and Zeeman energies A/ω_z and included in our model via species-specific scattering rates. Taking $(\mathcal{I}_z^{\text{As}}, \mathcal{I}_z^{\text{Ga}})$ over our range of accessible arsenic polarisations and performing linear fits to both, we find that $\mathcal{I}_z^{\text{Ga}} = 0.46\mathcal{I}_z^{\text{As}}$. We use this relation to estimate $\mathcal{I}_z^{\text{Ga}}$ from the data in Fig. 5.13 (a).

We can then arrive at an asymmetry-commensurate Overhauser shift:

$$\delta_{\text{O}}^* = \frac{3}{2}A^{\text{As}}\mathcal{I}_z^{\text{As},*} + x\frac{9}{2}A^{\text{In}}\mathcal{I}_z^{\text{In},*} + (1-x)\frac{3}{2}A^{\text{Ga}}\mathcal{I}_z^{\text{Ga},*}. \quad (5.18)$$

The hyperfine constants A^j are well known parameters, and the best fit for the indium concentration x is 0.5 [156]; across all previous works, x has been reported to range from 0.25-0.75 [320].

In direct parallel to Eq. 5.17, we compare δ_{O}^* with the mean field which we impose experimentally, δ_{O} . The result is plotted in Fig. 5.14; we observe a striking enhancement of δ_{O}^* , which exceeds δ_{O} by a factor of 2.9(1). Even if we assume that the QD studied here is among the most gallium-rich InGaAs QDs ever reported (i.e. $x = 0.25$), this enhancement factor is reduced only to 1.9(1). This result therefore constitutes the fingerprint of entanglement

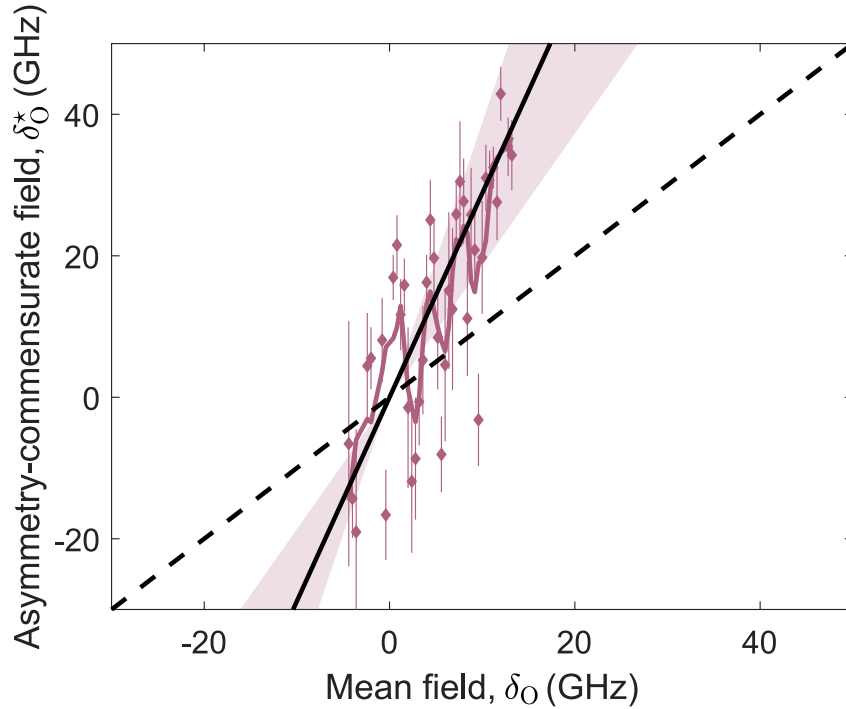


Figure 5.14: δ_O^* , extracted from asymmetry, vs. δ_O imposed experimentally (pink data points). The solid pink curve is the data passed through a Savitsky-Golay filter with a 1.6-GHz window. The solid black line is a fit to the data, with a gradient of 2.9(1). The dashed black line is the one-to-one correspondence which would be displayed by a classical state. The shaded coral area is the equivalent result for the full range of previously reported indium concentrations, $x = 0.25 - 0.75$.

within the nuclear ensemble.

We can glean further intuition from this result by recasting Eq. 5.13 in terms of $\langle \hat{I} \rangle$ and $\langle \hat{I}_z \rangle$:

$$\nu = \frac{\langle \hat{I}_z \rangle}{\langle \hat{I}^2 \rangle - \langle \hat{I}_z \rangle^2}. \quad (5.19)$$

An asymmetry which is enhanced compared to the thermal case (where

$\nu = \langle \hat{I}_z \rangle / I_{\max}$ is achieved when

$$\langle \hat{I}^2 \rangle \sim \langle \hat{I}_z \rangle (\langle \hat{I}_z \rangle + 1); \quad (5.20)$$

indeed, in this case the asymmetry is maximally enhanced to $\nu \sim 1$. The condition in Eq. 5.20 corresponds to a sub-radiant, or dark, state. (By a very similar argument, the opposite case where ν is reduced below its classical value is a hallmark of a super-radiant, or bright, state.) Dark state coherences, such as those whose fingerprint we uncover here, have been predicted to manifest themselves in QDs [283, 321–323].

5.9 Conclusions and Outlook

In this Chapter we have demonstrated polarisation of a QD nuclear spin ensemble using a new technique, opening some important future avenues.

Firstly, we saw in the background to this Chapter that the attractive properties of a QD nuclear spin ensemble has led to its proposition for a wide range of technological applications, in particular as a quantum memory. In this protocol, a quantum state is transferred from an electron spin confined to the QD onto the nuclear spin ensemble, and imprinted back onto the electron spin at a later time. Because the coherence times of nuclear spins are orders of magnitude longer than those of the electron spin [161], this approach promises great improvement in the performance of QDs as quantum network nodes.

The transfer step must perform an operation of the following form:

$$\frac{1}{\sqrt{2}}(|\uparrow\rangle + |\downarrow\rangle) \otimes |I_z\rangle \longrightarrow |\uparrow\rangle \otimes \frac{1}{\sqrt{2}}(|I_z\rangle + |I_z + 1\rangle) \quad (5.21)$$

The proposal of greatest relevance to our QD system, detailed in Ref. [171], realises this operation - which corresponds to excitation of a single magnon, conditional on the electron state - by an intrinsic asymmetry in coupling rates. In other words, the scheme works by relying on the faster excitation of magnons from $|\downarrow\rangle$ than from $|\uparrow\rangle$. This is precisely the asymmetry which we presented in Fig. 5.8, which illustrates the feasibility of this approach. In the proposal of Ref. [171], the principal limitation of memory fidelity comes from an imperfect asymmetry, itself a consequence of incomplete polarisation. However, the results which we have presented in this Chapter indicate that full asymmetry can be achieved even whilst operating at low polarisation. This has the additional benefit of reducing the unwanted effects of nuclear spin diffusion, whose rate increases with polarisation. Realistic operation of such a scheme could reach the proof-of-principle level in the current experimental setup.

Secondly, whilst our technique provides novel insight into the nuclear state, it is restricted to the z projection of nuclear polarisation (along with total angular momentum). Combining our approach with global controls using NMR fields, we could perform a tomography of the entangled many-body states which we generate, in the collective basis.

Finally, the long-awaited demonstration of entanglement within the nuclear ensemble illustrates the status of QDs as a realistic testbed for many-body physics [291, 324].

The most interesting of these outlooks rely on coherent interface between the electron and magnon modes. As we have seen in this Chapter, in InGaAs QDs the operation fidelity achievable is low. The drastic variation of the strain environment across the QD leads to inhomogeneous coupling to different nuclear lattice sites. This fact of the system places an unavoidable

limit on the coherence of the electro-nuclear interface which can be realised. Unfortunately, this is so fundamental to the InGaAs QD that we can only address it by moving to a different physical system. Chapter 6 will provide further details on this outlook.

Chapter 6

A Spin Confined to a GaAs Quantum Dot

As we have seen in the preceding Chapters, semiconductor quantum dots constitute a fascinating physical system, holding spectacular promise for the development of quantum technological applications. The most interesting features of this system result from the nuclear environment which constitutes the QD. We have seen that this allowed the study of collective phenomena, by exploiting the proxy qubit resident in the QD. Beyond, the nuclear ensemble promises the long-term storage of a quantum state, allowing a QD to be operated as a quantum repeater.

Reaching these goals with QDs requires a highly coherent interaction between the electron and its nuclear ensemble. Whilst we have seen that InGaAs QDs can support some electro-nuclear coherence, the facts of the material and growth process place hard limitations on the possibilities with these samples. If QDs are to develop as a viable platform for quantum

technologies, a new generation of nanostructures will be necessary.

In this Chapter, we will detail work developing a new type of QD samples. We show gate-controlled emission, coherent interaction between an optical field and the QD excitons, and electron spin preparation. This allows us to measure the spin lifetime, and we then perform coherent control of an electron spin confined to a GaAs QD. These results demonstrate the future potential of these QD samples.

The data in this Chapter were taken with Leon Zaporski. The samples used in this Chapter were grown at the Johannes Kepler Universität in Linz, Austria, in the group led by Armando Rastelli. They were processed in Cambridge by John Jarman and Noah Shofer.

6.1 Background

Thus far, we have worked with self-assembled quantum dots of indium gallium arsenide, formed via the Stranski-Krastanov (SK) growth process. In this type of QD, the nuclear environment is made up of three elements, all with different material constants. In addition, the formation process of these QDs is fundamentally based on a lattice parameter mismatch between the QDs and their surrounding GaAs matrix, which causes InAs to prefer to cluster together into small islands which become our QDs. This leads to a high degree of inhomogeneity of strain across the QD. This is important because the degree of strain controls the strength of quadrupolar coupling between the electron and the nuclei, which therefore also varies across the QD. These material and environmental inhomogeneities are responsible for both the limits on the electron spin coherence [156], and the weak coherence between the electron spin and magnon modes measurable in InGaAs

QDs [176]. These properties are fundamental to a QD formed by lattice parameter mismatch, which is the phenomenon underpinning the SK growth process.

In order to circumvent these challenges, we must therefore take a different route, using a different platform. Fortunately, a natural alternative exists: the GaAs quantum dot, embedded in an AlGaAs matrix. These two structures have matched lattice parameters, meaning that the QDs are strain free (if left to their own devices). Whilst this will have happy consequences for the nuclear spin properties later on, it for now means that a more deliberate approach must be taken in order to cause the formation of QDs.

Instead of Stranski-Krastanov growth, the generation of QDs in this material proceeds via a technique known as droplet epitaxy [325]. Starting with a substrate of $\text{Al}_{0.4}\text{Ga}_{0.6}\text{As}$, droplets of aluminium are deposited on the surface. Under carefully chosen conditions, these droplets cause deposition of arsenic from the substrate immediately underneath, leaving empty space behind: the droplets act as “nanodrills”, which etch “nanoholes” in the substrate [326–332]. Within these nanoholes, GaAs is deposited, forming lattice-matched, low-strain QDs [333, 334].

In terms of optical properties, these QDs have been shown to be bright and coherent single-photon sources [335–338]. In addition, they have a number of advantages over their Stranski-Krastanov-grown predecessors. Their optical emission around 780nm is close to rubidium transitions, which could allow the convenient formation of a hybrid quantum system [335, 339, 340]. The growth process gives a high degree of tunability over the density of QDs on the wafer as well as their emission wavelength [341, 342]. Further, the growth process allows them to have very high symmetry, which

has led to their implementation as sources of entangled pairs of photons [337, 339, 343–349]. Many of these works exploit the external application of strain to the sample in order to enhance their entanglement fidelity [350], a technique which also allows post-growth tuning of emission wavelength [325, 340, 351–353].

With regards to their spin properties, studies have probed and exploited the electro-nuclear (hyperfine) interaction in GaAs QDs [300, 301, 311, 354]. The homogeneous nature of the nuclei of a GaAs QD has already been exploited, allowing the implementation of an NMR quantum computing algorithm [207]. Finally, resonance fluorescence has been performed on these QDs, which allowed optical preparation of the electron spin and a measurement of the spin lifetime in Faraday geometry [355].

These results constitute the foundational framework on which the study of a homogeneous ensemble of nuclear spins could be built. The coherent nature of both the optical interactions and the nuclear environment of GaAs QDs has been confirmed. Further, the possibility of applying strain to the samples, key to actuating electro-nuclear coupling, has been demonstrated. Despite this progress, the study of these new samples remains in its infancy, and we start from a basic characterisation of our samples, following the steps outlined in Chapter 2.

6.2 Sample structure

Our samples are grown using the above method, and are very similar in form to the InGaAs samples previously discussed in Section 2.1. The sample structure is depicted schematically in Fig. 6.1; the principal difference is that the QDs are housed inside a p-i-n diode. This requires a small change to

the processing procedure, because the contact to the back gate must not short with the p doped layer. In order to avoid this, we etch through the p doping, making the back contact without contacting the p doped layer. This can be seen in Fig. 6.1 (a), where our gate is placed in a region of the sample which has been locally etched to remove the p doped layer. This is also visible in Fig. 6.1 (b), a photo of our sample; the upper golden strip is the back contact, and horizontal hairlines above and below this contact indicate the etched region.

We again use a solid immersion lens (SIL) in order to enhance our collection efficiency. We find experimentally that the SIL is extremely difficult to attach to these samples, frequently detaching as the sample is cooled to 4.2 K. We avoid this by attaching the SIL to the sample using a mixture of GE varnish and acetone, as illustrated in Fig. 6.1 (b). Combined with a slow cool-down procedure (taking ~ 12 hours), this gives reliable SIL attachment at low temperatures.

Finally, these samples have a single pair of layers which constitute their distributed Bragg reflector (DBR) (Fig. 6.1 [a]). To further increase our collection efficiency, future generations of these samples will be grown with more extensive DBRs.

6.3 Experimental setup

Here, we note briefly the small differences in setup when compared to previous Chapters. The only difference of significance for the experiments presented here is that the QDs emit around 780 nm, which necessitates a different set of lasers and optical components. Here, we use a Toptica DL Pro and a MogLabs diode laser, both at 780 nm. In addition, we use a different EOM:

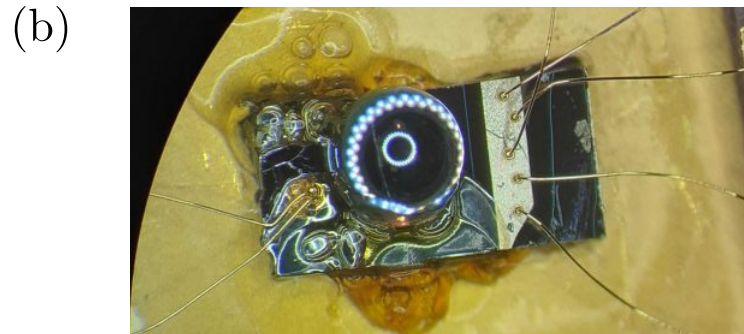
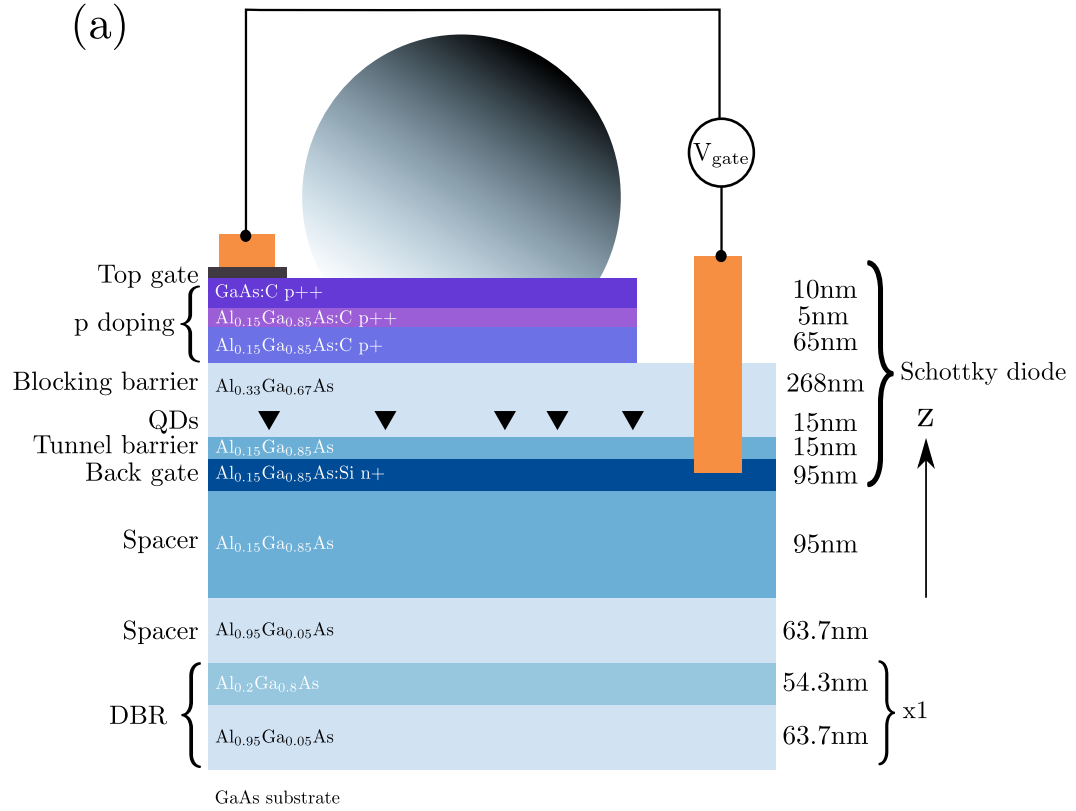


Figure 6.1: (a) Sample structure schematic. (b) Photo of sample, looking along the z axis of (a). Golden strip on right of sample: back contact. Golden circular region on left of sample: top gate. Central (superhemi-) spherical object: SIL. Surrounding brown substance: GE varnish and acetone blend. Thin golden leads: external connections to diode gates.

a 20-GHz device supplied by IxBlue. Fibres, waveplates, and AOMs are also wavelength dependent and we select new models appropriately. Otherwise, the setup is unchanged.

6.4 Sample characterisation

Photoluminescence measurements of our sample reveal the data shown in Fig. 6.2. Two classes of lines appear: those below 383 THz, which correspond to optical emission via the electronic s-shell states, and those above, which proceed via electronic p-shell states. We will use the s-shell states for the rest of our experiments. We observe distinct charging plateaus, as we require for both charge state selection and long spin lifetime. The lines appear close to the transform limit, within the resolution of our spectrometer. They are dimmer than equivalent InGaAs QD transitions measured under PL; we attribute this to the lack of DBR on our sample, and the lack of wetting layer in these structures. The wetting layer present in InGaAs samples facilitates exciton recombination in PL by acting as an intermediary through which excited charges in the structure can relax into the QD bound states [356]. Fortunately, the absence of this mechanism in GaAs QD samples does not affect the strength of their coherent interactions with a resonant laser.

From here, we proceed to resonance fluorescence. We begin with the neutral exciton, revealing the data in Fig. 6.3. Fitting this dataset allows us to extract a fine structure splitting of 2.1 GHz, in close agreement with literature [355]. Further, we measure FWHMs of 1.08 (1.62) GHz for the low (high) energy transition. These values are close to the transform limit, which is around 1 GHz [335], and indicate the low noise present in these samples over the timescale of this measurement (2 seconds).

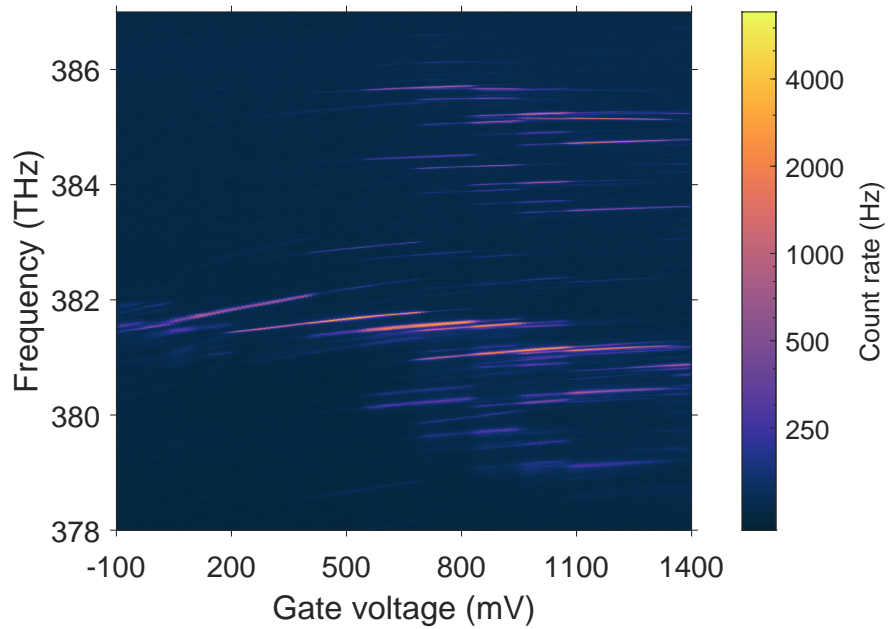


Figure 6.2: PL of a GaAs QD at 0 T.

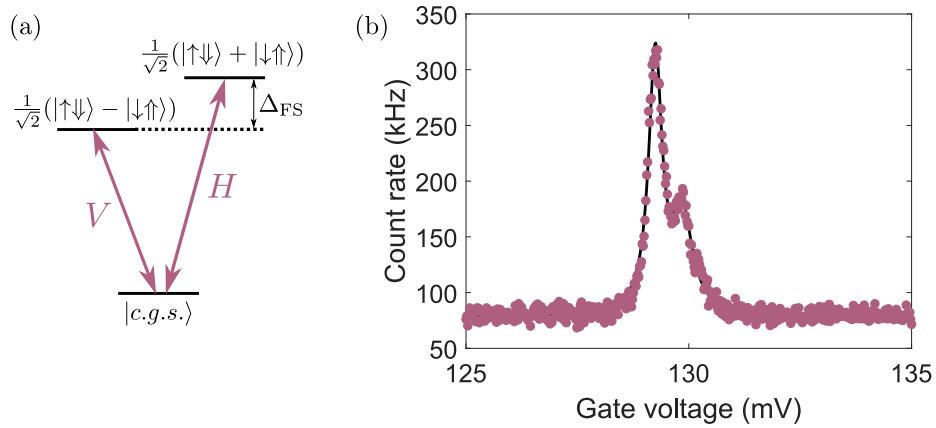


Figure 6.3: (a) Neutral exciton level diagram. (b) Count rate as a function of gate voltage (pink circles) along with a bi-Lorentzian fit (black curve), taken at 10% of the saturation power.

Next, we turn our attention to the spin properties of the system, which requires application of an external magnetic field. Here, ours is oriented to place us in Voigt geometry, and has a magnitude of 6.5 T. A PL spectrum taken under this condition is shown in Fig. 6.4, where several of the lines are now Zeeman-split. Finer resolution of these split lines requires measurement via resonance fluorescence, which we perform on the negative exciton on Fig. 6.5. Remarkably, we resolve all four transitions associated with X^- , allowing extraction of the magnitude of the electron and hole g factors. These can be distinguished from one another using the measurements of Section 6.7. We summarise these parameters, along with the corresponding ones extracted from the neutral exciton, in the table below.

Exciton	X^0	X^-
g_e	–	-0.0253
g_h	–	0.131
$g_e - g_h$	0.0506	0.156

We have taken these g factors to have the same signs as measured in Ref. [301]. The striking disagreement between the neutral and negative exciton g factors has been observed elsewhere and attributed to the relatively weak lateral confinement exerted by these QDs [357].

The data shown in Fig. 6.5 further displays a count rate which is highly dependent on the gate voltage across the sample; at the edges of the region of stability of X^- , count rate is enhanced, whilst in the centre, count rate is suppressed. This behaviour is a hallmark of spin-state preparation via optical pumping: in the centre of the plateau, the electron spin lifetime T_1 is extended, suppressing fluorescence. At the plateau edges, the electron spin is rapidly re-set by tunnelling in and out of the QD, shortening T_1

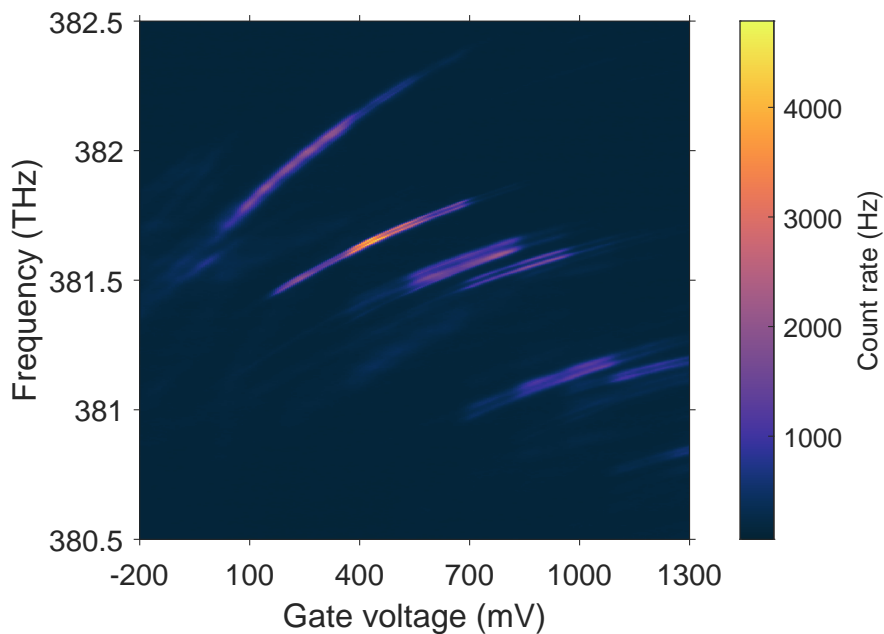


Figure 6.4: PL of a GaAs QD at 6.5 T.

and enhancing fluorescence. This measurement allows us to identify the X^- stability plateau and cotunnelling regions.

6.5 Spin lifetime

We can now proceed to study the behaviour of our confined spin. The measurements of this Section were performed on a different device, n-doped and with a thicker tunnel barrier.

Spin pumping is a dynamic process, and a steady-state measurement such as that depicted in Fig. 6.5 is therefore not able to extract its full behaviour. In order to do this, we implement a time-resolved, pulsed measurement, depicted schematically in Fig. 6.6. Two laser pulses, offset in

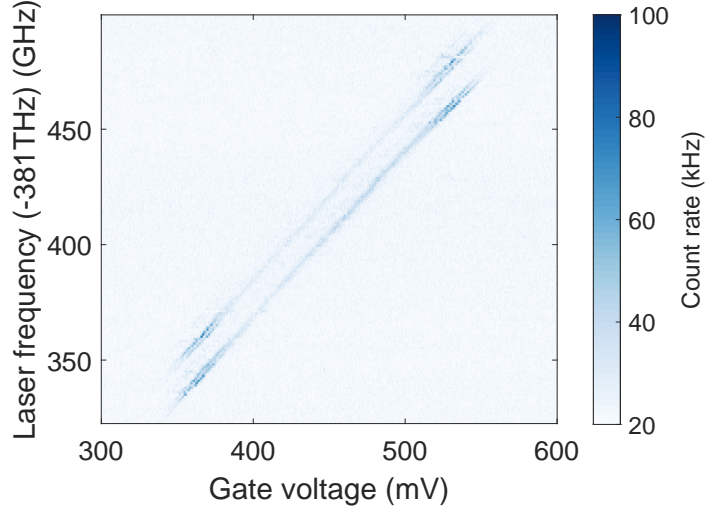


Figure 6.5: RF map of the X^- plateau at a magnetic field of 6.5 T.

frequency by the sum of electron and hole Zeeman energies, drive the system one after the other. Their action is to pump the electron spin backwards and forwards between its ground states.

In Fig. 6.7 (a), we plot the count rate during one of these pulses i.e. we zoom in on the purple pulse of Fig. 6.6 (b). In addition to laser background, a transient behaviour is visible, testifying to the “pumping” nature of the system in this regime. Performing the same measurement for increasing pump pulse power P (as denoted in Fig. 6.6), we observe the acceleration of the pumping process, as shown in Fig. 6.7 (b). This measurement bounds the lifetime of the excited state to be shorter than the shortest pumping time which we measure (8.96 ns). Given previous measurements of optical excited state lifetimes of a few hundred picoseconds, this is an expected result [337]. These data show that we can readout and prepare the spin state to high fidelity within a few tens of nanoseconds.

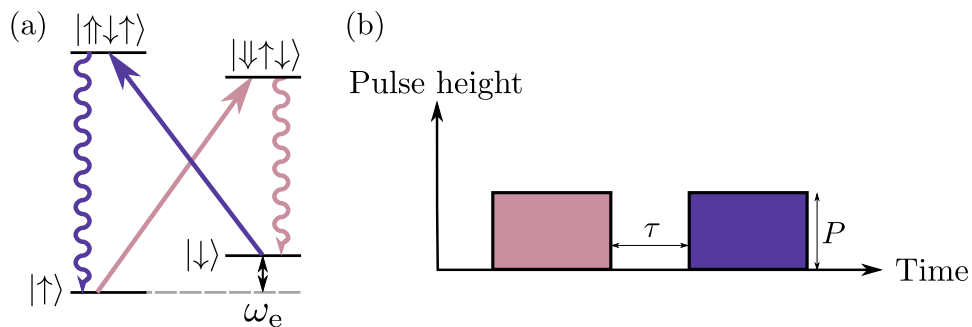


Figure 6.6: (a) X^- level diagram. Solid arrows are processes driven resonantly by a laser. Wiggly arrows denote spontaneous decay. Colours mark the full pumping channel. (b) Pulse sequence schematic. Two pulses of different frequencies interrogate the system one after the other.

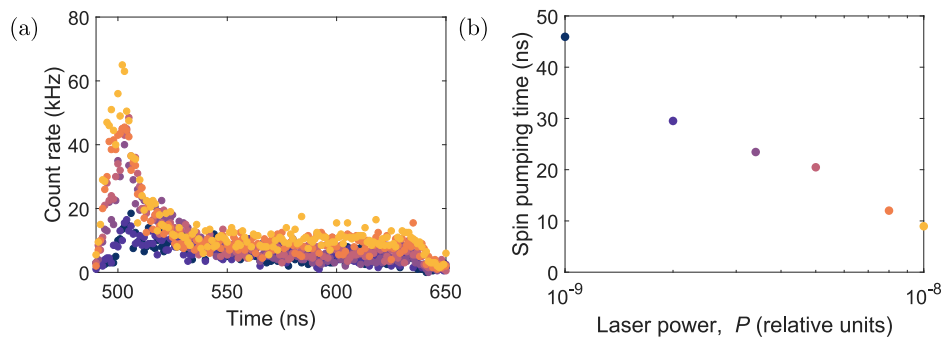


Figure 6.7: Spin pumping laser power. (a) Count rate during the pump pulse, for a set of increasing laser powers (dark to light colour). (b) Spin pumping times extracted from the data in (a), indicated by colour.

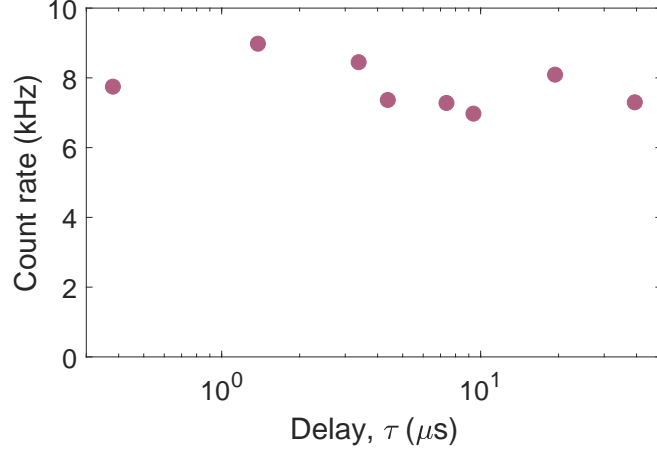


Figure 6.8: Count rate as a function of delay between two pulses which are set to pump the spin in opposite directions.

One important property to which we have access using these repump pulses is the spin lifetime, T_1 . In order to measure this, we use the same two-colour measurement, but now vary the separation τ of the two pulses. Tracking the resulting count rate on the final pulse allows us to measure the spin relaxation time. These data are presented in Fig. 6.8, where we observe an unchanged count rate up to a pulse separation of $40 \mu\text{s}$. We can therefore safely benchmark T_1 as much longer than $40 \mu\text{s}$. The only other measurement of this parameter in a GaAs QD was performed in Faraday geometry via the weakly allowed diagonal transitions, yielding $T_1 = 48 \mu\text{s}$ [355]. The lifetime places a limit on spin coherence according to $T_2 \leq 2T_1$. Since T_2 has not been measured in a GaAs QD, we can only roughly estimate it from the InGaAs QD T_2 of a few microseconds [156]. The data presented here therefore indicate that our spin lifetime is unlikely to limit spin coherence.

6.6 Spin control

Our spin manipulation operations have thus far operated via incoherent processes (spontaneous scattering). In order to exploit the electron spin as a qubit, we must develop coherent control. In order to do this, we use ultrashort laser pulses derived from a modelocked laser, in line with the first demonstrations of coherent spin control in QDs [41–43]. The physical mechanism underpinning this approach has been described in detail in Section 2.5, and we therefore proceed directly to the experimental data, which is presented in Fig. 6.9. We observe high-visibility oscillation up to a rotation angle of 3π , confirming the coherent nature of the process. Alongside, the rotation angle θ depends sublinearly on pulse power P ; by fitting the data in Fig. 6.9 according to $\theta \propto P^\beta$ we extract an exponent $\beta = 0.65(1)$. Whilst the mechanism underpinning this sublinearity is unclear, our observations are in close agreement with previous implementations of this spin control technique [42]. This is the first demonstration of coherent spin control in an optically active GaAs QD, and constitutes a key result in the study of spin physics on this platform.

6.7 Spin coherence

6.7.1 Ramsey interferometry

From this point, it is straightforward to perform Ramsey interferometry, a technique which was described in detail in Section 2.7. Free precession of the electron spin allows information about the environmental noise to be extracted by tracking the length of the Bloch vector. This reveals the

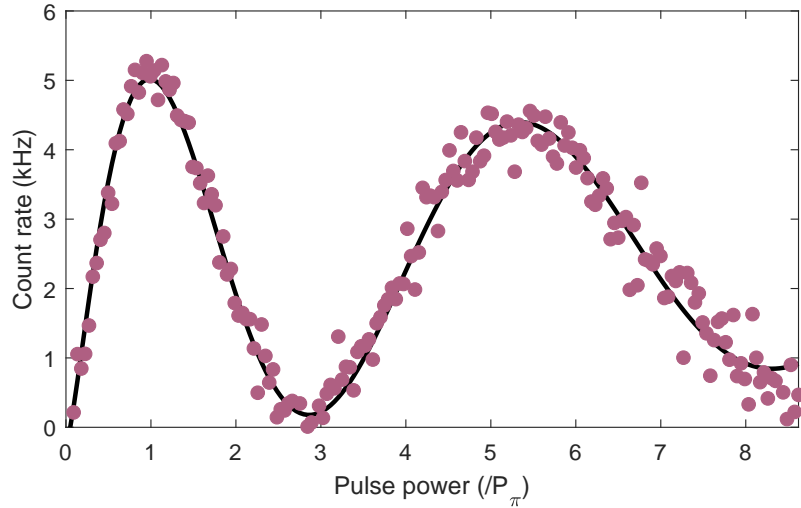


Figure 6.9: Count rate (pink circles) following an ultrashort pulse whose power, P , is tuned. The x-axis quotes pulse power relative to the power required for a π rotation, P_π . A fit of the form $a \cos(\pi[P/P_\pi]^\beta) e^{-(P/\kappa)}$ (black curve) yields $\beta = 0.65(1)$.

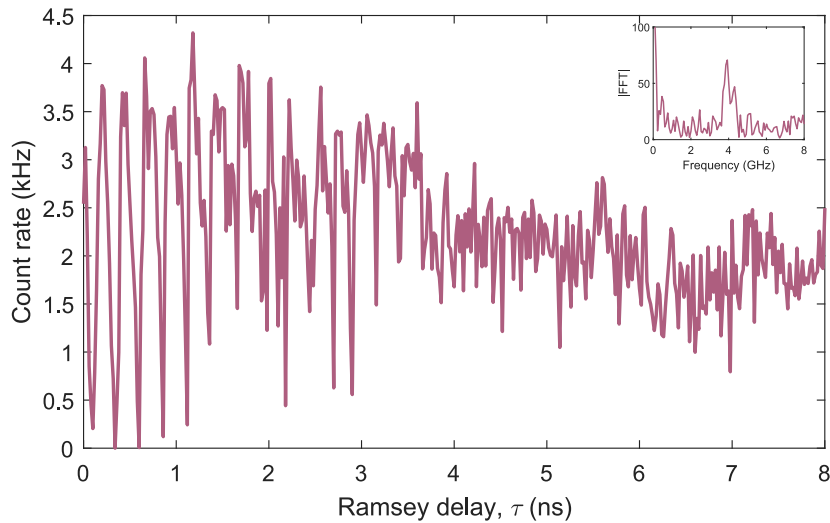


Figure 6.10: Count rate following two $\frac{\pi}{2}$ pulses (solid pink line), as a function of their temporal separation τ . Inset: FFT of data in main panel.

data shown in Fig. 6.10. We observe spin precession at the electron Zeeman energy, in addition to a saw-tooth pattern characteristic of a measurement affected by nuclear spin feedback [156].

In order to minimise nuclear spin feedback, we use the approach detailed in Ref. [156] and Section 3.9: we alternate the initial electron spin state between $|\uparrow\rangle$ and $|\downarrow\rangle$ from one sequence to the next. In this way, we maintain an average electron spin polarisation close to zero throughout the experiment, which minimises electron-mediated feedback. The results of this experiment are presented in Fig. 6.11 (a,b). We find that nuclear spin feedback persists; the data are remarkably similar to those presented in Fig. 6.10. The effects of our measurement on the nuclear spin environment are apparent when we analyse the data in Fourier space in Fig. 6.11 (c,d). Here, we observe a frequency offset of electron spin precession which depends on scan direction. Together, these data suggest a feedback mechanism which is not electron-mediated. We repump the electron spin via an excited state which carries a hole spin, and since the noncollinear interaction of the hole is present even in the absence of strain, this is a likely culprit.

Nevertheless, the data in Fig. 6.11 allow us to extract the electron spin inhomogeneous dephasing time. As is evident in the Figure, alternating the initial electron spin state results in two signals, whose contrast depends on the remaining coherence despite the presence of nuclear spin feedback. Here, we extract a Gaussian decay envelope with $T_2^* = 5.9(3)$ ns. This is a threefold enhancement in coherence when compared to an InGaAs QD [156], arising due to the larger size of a GaAs QD [357] and their lack of (high-spin) indium nuclei.

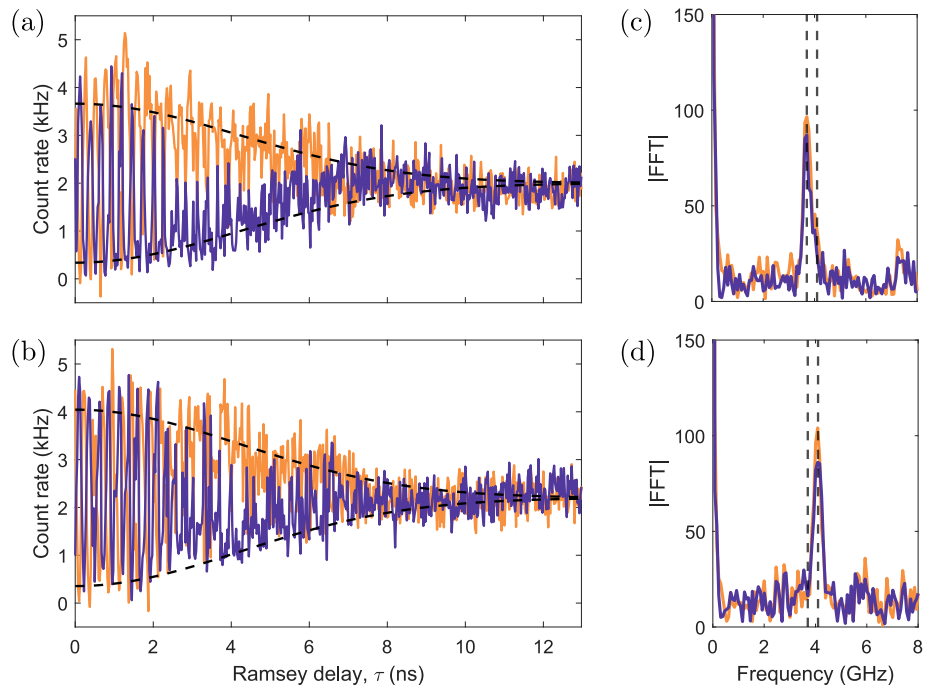


Figure 6.11: Ramsey interferometry, measured with (without) a π pulse immediately before the sequence (purple [orange]) line. Data acquired for scan direction: (a) increasing τ , (b) decreasing τ . Dashed curves are a Gaussian fit to the contrast envelope, with $T_2^* = 5.9(3)$ ns. (c,d) FFT of data in (a,b) respectively, and indicated by colour. Dashed lines at 3.7, 4.1 GHz guide the eye.

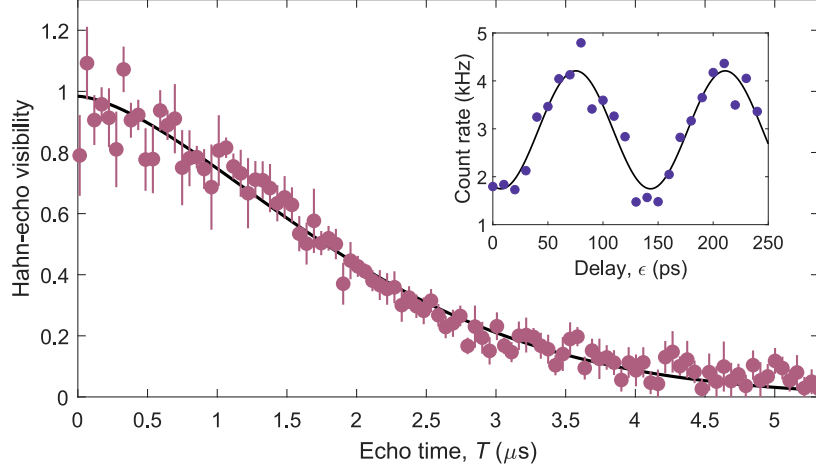


Figure 6.12: Hahn-echo visibility as a function of the echo time T (pink circles). The black curve is a fit of the form $e^{-(T/T_2)^\alpha}$, with $\alpha = 1.57(7)$ and $T_2 = 2277(48)$ ns. Error bars indicate 66% confidence intervals. Inset: Count rate as a function of delay of the central π pulse relative to the midpoint of the two $\frac{\pi}{2}$ pulses, for $T = 2061.3$ ns (purple circles), along with a sinusoidal fit (black curve).

6.7.2 Hahn-echo spectroscopy

We can further probe the coherence of the electron spin using Hahn-echo spectroscopy. This technique, which was previously discussed in Section 2.7 and depicted in Fig. 2.14 (a), proceeds as follows. A first $\frac{\pi}{2}$ pulse is followed by a precession time of $\frac{T}{2}$. The spin is then inverted by a π pulse, after which it is allowed to evolve for another time $\frac{T}{2}$ before a final $\frac{\pi}{2}$ pulse. Any perturbations to the ESR which are constant during the pulse sequence are filtered out, resulting in an echo of coherence.

Experimentally, we measure the strength of the echo as a function of the overall echo time T . We probe the coherence of the spin by tracking the count rate as we scan the π pulse in time by an amount $\epsilon \ll T$ away from the midpoint of the sequence (inset to Fig. 6.12), and extracting a visibility from the resulting fringes. Fig. 6.12 plots these Hahn-echo visibil-

ities as a function of T . Fitting with the functional form $e^{-(T/T_2)^\alpha}$ yields $\alpha = 1.57(7)$ and $T_2 = 2277(48)$ ns. This coherence time is comparable to similar measurements in InGaAs QDs [156], but the exponent α is strikingly different to the exponential decay previously observed. Under Hahn echo, an exponential decay of coherence is symptomatic of a white noise source, which effectively arises in InGaAs QDs due to the high degree of strain inhomogeneity-induced broadening [156]. Here, $\alpha > 1$ is a signature of a more homogeneous nuclear environment, which no longer appears white to the Hahn-echo sequence.

6.8 Line stability

Throughout the experiments of this Chapter, we have observed jumping of lines under resonant driving. Figure 6.13 depicts the signal which we obtain when at constant laser frequency and constant gate voltage, in the centre of the charging plateaus of X^0 and X^- . The resonance fluorescence of the QD is unstable, leading to a blinking which is particularly pronounced on X^0 .

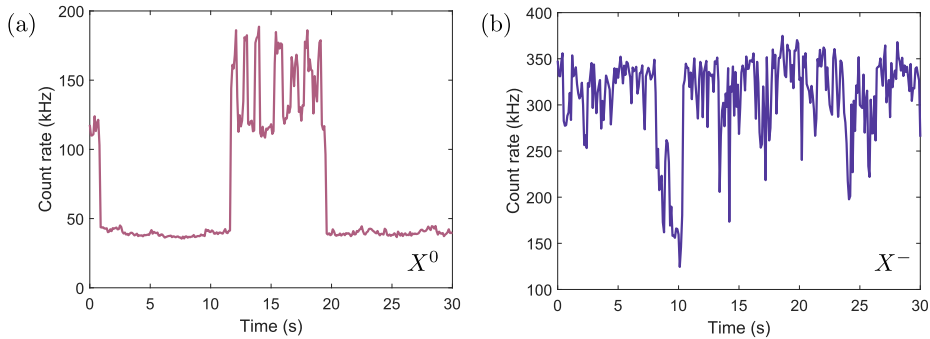


Figure 6.13: Resonance fluorescence from a QD as a function of time, in the centre of the (a) X^0 and (b) X^- plateaus. Power was 20% of saturation.

In order to investigate these effects further, we measure the lineshape

of X^0 by scanning our gate voltage at fixed laser frequency. We repeat this measurement several times, over a timescale of tens of seconds, and investigate how the result depends on laser power. Figure 6.14 presents the experimental data. At low power, we observe good stability over the 40 s-timescale of the experiment. As the laser power is increased, spectral jumps are induced and then accelerated, eventually occurring on a sub-second timescale at the highest power we measure. These jumps are discrete, suggestive of nearby charge traps which can be loaded or unloaded by driving the QD. These jumps have been observed in previous works [335, 358], and are very slow compared to the emission time of the QD.

Since we are here interested in the spin properties of the system, we can proceed in spite of these observations. The jumping effect translates to a reduced count rate and we simply increase our integration time accordingly. This effect is evident in the y-axes of Figs. 6.9 and 6.10, when compared to the count rates expected based on Fig. 6.5. Jumping is, of course, an undesirable property and removing it will be a focus of future growth efforts. This type of noise is not intrinsic to the choice of material, and GaAs QDs which are free from it have been reported [355, 359].

6.9 Conclusions and Outlook

In this Chapter we have introduced the strain-free, GaAs QD as a platform for spin physics. We have demonstrated the optical quality, observing linewidths very close to the transform limit. This allowed us to characterise the spin properties of an electron confined by the QD, including its lifetime and its coherence.

The sample quality presented an additional challenge in performing these

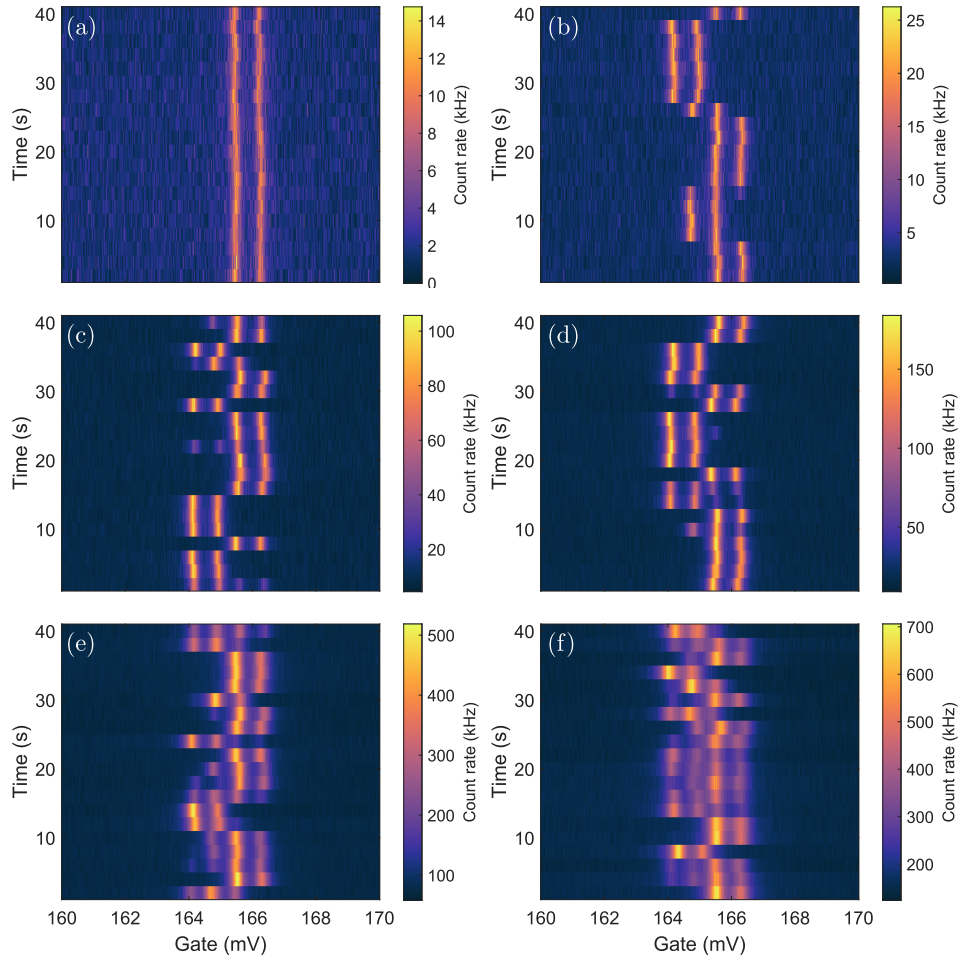


Figure 6.14: X^0 lineshape as a function of laser power, tracked over time. Laser power is (a) 1%, (b) 2%, (c) 10%, (d) 20%, (e) 100%, (f) 200% relative to saturation.

measurements. Reducing the noise originating from the solid-state environment of the QD is a major outstanding challenge for our collaborators in the development of these QDs as a platform for quantum technologies. However, these results illustrate the power of spins: despite significant electrical noise in the sample, we have been able to perform coherent spin control.

Beyond, our measurements demonstrate the viability of GaAs QDs as a host for a single electron spin. We have shown that we can confine and coherently control a long-lived electron spin, and we have measured its inhomogeneous dephasing to be comparable to those typically seen in InGaAs QDs.

A key attraction of using these QDs is the homogeneity of their nuclear environment, which we have already observed in the non-exponential decay of our Hahn-echo visibility. This result motivates the implementation of dynamical decoupling, which promises to improve the coherence time further by offering more broadband filtering of environmental noise [193, 360, 361].

Next, these QDs are expected to be a fascinating host for the magnon physics which we explored in Chapters 4 and 5. In order to make use of the same noncollinear coupling which we previously exploited, strain is necessary. In an InGaAs QD, this strain originates naturally due to the growth process, but is unavoidably highly inhomogeneous [156]. In the case of GaAs QDs, strain is expected to be largely absent thanks to lattice-parameter matching, and we must therefore apply it externally. This has the distinct advantage that the strain will be homogeneous across the QD, meaning that coupling strengths will not vary across nuclear lattice sites (at least, not because of strain), enhancing the coherence of the interface between the electron and magnon modes. So-called strain-tuning devices have been implemented using these samples, primarily to allow tuning of emission

wavelength [325,340,350–353], and showing that this approach can tune the interaction strength with magnon modes would constitute a landmark result for GaAs QDs.

The magnon modes of a GaAs QD are highly interesting because of their expected coherence. They have been the subject of a proposal to operate the system as a quantum memory [171], which predicts an operation fidelity of over 90% under realistic experimental conditions.

In addition, nuclear state preparation in InGaAs QDs has thus far been limited by the inhomogeneity of the ensemble, and it may therefore be possible to enhance the spin properties of a GaAs QD beyond this limit.

Chapter 7

Conclusions and Outlook

The work presented in this dissertation has achieved three main objectives: flexible, high-fidelity manipulation of a single QD-confined spin; measurement of quantum correlations in the many-body nuclear ensemble of a QD by driving collective modes; and demonstration of the coherence properties of the new generation of strain-free QD samples.

In Chapters 3 and 4 we implemented an arbitrarily flexible control technique for high-fidelity coherent manipulation of a single spin in a QD. The technique allowed us to design pulse sequences at will, unconstrained by the practical considerations which plagued the previous state of the art. Here, we used that flexibility to decouple the electron spin from its environment using spin locking. This technique has been vital to the research output of our group, enabling the measurements presented in Refs. [176, 224, 238, 246] (which would have otherwise been impossible). It has been adopted by other QD research groups [362–364], and we hope that more will follow. More broadly, the technique has allowed the first demonstration of coherent

control of the spin of a tin-vacancy centre in diamond [365].

In Chapter 5, we showed a coherent interface between an electron spin and its nuclear environment. This result has led directly to proposals for the exploitation of nuclear modes as a quantum memory [171, 366]. These proposals lead towards the construction of a quantum network of QDs, each with its own in-situ memory.

Further, we proposed a technique for reconstructing the state of a many-body ensemble based on collective measurements. This technique can be applied to any system which is in a classical state, and will be particularly useful where single-particle, or single-site, resolution is not achievable. This technique could be extended to account for the presence of coherences within the ensemble if the degree of entanglement could be quantified. Since nuclear spin cooling generates entanglement, we could measure the asymmetry for a set of different cooling strengths in order to extract a correction factor to account for the presence of entanglement. Unfortunately, the cooling performance and therefore the degree of entanglement is intimately related to the resolution of magnon modes: we cannot observe magnon modes in a thermal nuclear state using our direct drive technique, because the ESR is too broad. This could be bypassed by instead using a magnon drive which is insensitive to the electron T_2^* , such as PulsePol [242] or other tailor-made pulse sequences.

In our case, the result of this technique was a direct measurement of many-body entanglement in the nuclear environment. Quantum-correlated states of the QD nuclei have been the subject of a number of theoretical studies [282, 283, 321, 367], and large entangled states in general have been suggested as a tool for high-resolution spectroscopic measurements [368–370]. More immediately, the dark state which we generate lends itself to the imple-

mentation of a high-fidelity quantum memory under the scheme proposed in Ref. [171] but at low polarisation [283], thanks to the enhancement of asymmetry.

Further, this demonstration opens the possibility of studying quantum many-body dynamics in a QD nuclear ensemble [248–250]. This could include its use as a quantum simulator [371]. Whilst we show subradiance here, the regime of superradiance remains unexplored and in principle allows faster, and therefore more coherent, interaction with magnon modes [372]. In addition, showing the quantum nature of the QD nuclei motivates the study of other collective phenomena, an example of which is the generation of time crystals [324, 373].

In Chapter 6, we demonstrated the first spin control experiments on the new generation of homogeneous, strain-free QD samples. We showed that we can coherently manipulate a QD spin, and measured its coherence time. Immediate extensions of this work are to implement our flexible control technique of Chapters 3 and 4 on this platform, which will likely require nuclear spin narrowing. In turn, such a driven nuclear spin interaction will be based on externally applied strain, which would then combine with flexible control to allow magnons to be driven on this platform. One consequence of the externally applied, homogeneous strain is that the electro-nuclear interface is expected to be highly coherent, and should allow the high-fidelity functioning of a quantum memory [171].

As experimental work on InGaAs QDs has reached full maturity, the technical expertise and physical hardware have likewise developed to allow remarkably complex, atomic physics-style experiments on solid-state systems. Whilst we have begun to run into the hard limitations of the InGaAs QD, the knowhow and setups are primed to carry the torch forward in the

next generation of samples.

Appendices

Appendix A

Microwave system

Throughout this dissertation, we employed a system of microwave generation in order to manipulate a spin confined to our QD. During the natural course of the work, this system evolved in sophistication as the experiments required. Here, we provide further details on these microwave setups. Throughout, the signal is fed to an EOM (EOSpace) which is used to modulate a laser (Toptica DL Pro).

A.1 Setup #1: Phase-disabled hole spin control

Figure A.1 shows a schematic diagram of our earliest microwave system, used for the first section of Chapter 3. In this figure, we include a schematic picture of the signal at each stage. The microwave source (Rohde & Schwarz SMF100A) is multiplied with the output of a delay generator (SRS DG645) on a switch (Mini-Circuits). The resulting microwave-frequency signal, which is turned on and off by the DG645, is amplified (Picosecond Labs 5865,

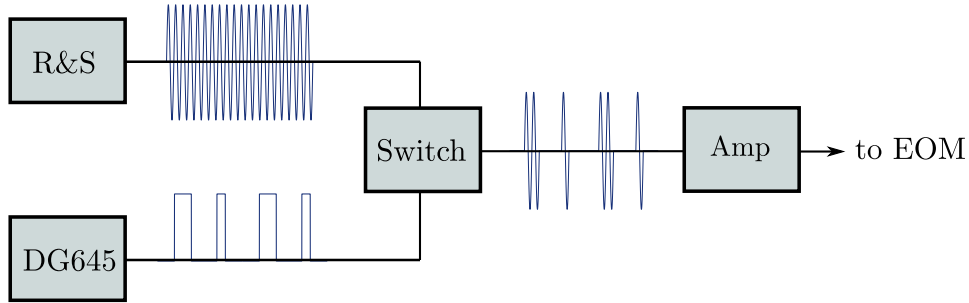


Figure A.1: Microwave setup #1 schematic.

12.5 Gbit/s). The DG645 also functions as the clock for our experiment. This system generates microwave signals at the hole spin resonance (a few GHz), with no control over the phase of the signal.

A.2 Setup #2: Phase-enabled hole spin control

For the second stage of the hole spin control experiment (Chapter 3), we required control over the phase of the microwave signal. In order to achieve this we used the setup shown in Fig. A.2, with an Arbitrary Waveform Generator (AWG, Tektronix AWG70002A) featuring a 12.5 GHz-bandwidth. Because the hole spin resonance was around 9 GHz, the 4.5-GHz signal required is well within the limits of the AWG. This allows the trivial construction of waveforms electronically, with phase jumps encoded into the electrical signal as desired. This also replaced the DG645 as the clock for the experiment.

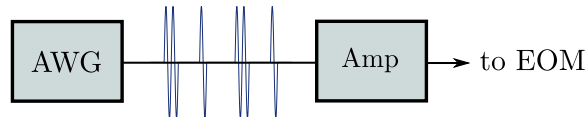


Figure A.2: Microwave setup #2 schematic.

A.3 Setup #3: Electron spin control

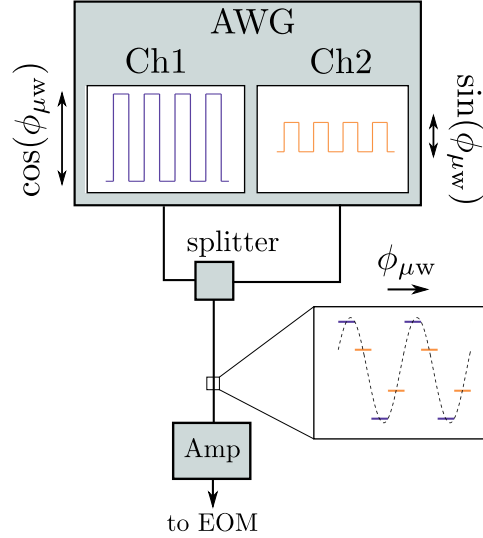


Figure A.3: Microwave setup #3 schematic.

The electron spin has a g factor larger than the hole spin, leading to Zeeman splittings of a few tens of GHz. In addition, the electron spin coherence is richly dependent on magnetic field, but in general improves with increasing magnetic field [156]. In practice, we chose a magnetic field of 3.3 T which was the maximum at which we could match the ESR with the microwave system available. Under these conditions, the ESR was 25 GHz, requiring a microwave signal of 12.5 GHz. Our AWG had a maximum sampling rate of 25 GSamples/s, which allows the minimal construction of a 12.5-GHz signal, using two points per period (i.e. as a square wave). However, this does not allow the encoding of phase, since the positions of the samples are fixed. Our solution to this is shown in Fig. A.3. We mix the two output channels of the AWG using a high-frequency splitter (Mini-Circuits). The AWG has a very precisely tuneable (1ps precision) offset between the two channels,

which we characterise by feeding the splitter output to a spectrum analyser and maximising the resulting power vs. this offset. From there, we increase the offset by a quarter of a period. Now with the channels having a relative phase of $\pi/2$, we generate waveforms with a relative phase of $\pi/2$. The relative amplitude of these waveforms then controls the phase of the resulting signal. This microwave system was used throughout Chapter 4.

A.4 Setup #4: Nuclear spin polarisation

For the experiment presented in Chapter 5, we wish to polarise the nuclear spin environment of the electron spin. The previous microwave setup has a maximum operation frequency of 12.5 GHz, and moreover does not allow tuning of this frequency other than by changing the sampling rate of the AWG, which cannot be done without (temporarily) disabling the outputs. In order to circumvent these challenges, we use the setup depicted in Fig. A.4.

We run the AWG at much lower frequency - 300 MHz - and upconvert it with a 6 GHz microwave tone using a wideband upconverter (Analog Circuits ADRF6780). The upconverter is fed by a Rohde & Schwarz microwave source operated initially at 6.4 GHz, which it frequency-doubles. The resulting 12.8 GHz tone is downshifted by the 300 MHz AWG signal, which supplies the IQ inputs of the upconverter. The 4 IQ inputs are fed by the two channels of the AWG (which play waveforms which are offset by $\pi/4$ from each other), and by their inverses. This results in a 12.5 GHz signal, which is amplified (by a Mini-Circuits ZVA-213-S+ wideband amp) and which generates sidebands separated by 25 GHz to match the ESR. Phase control is achieved trivially since the AWG is operated well within its bandwidth - we

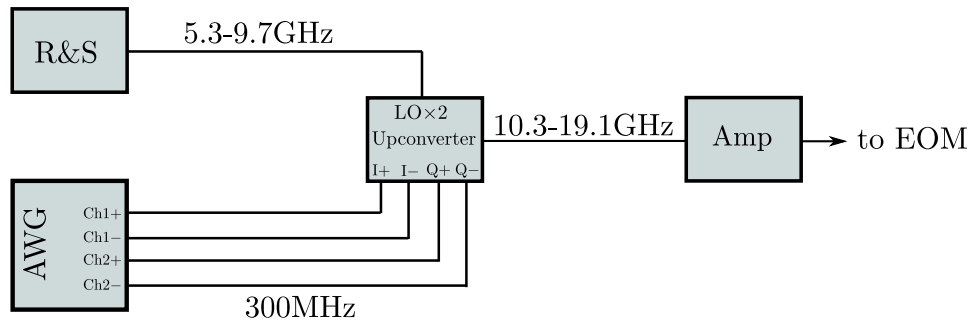


Figure A.4: Microwave setup #4 schematic.

simply define a phase when electrically designing the waveforms.

In order to polarise the system, we must tune the microwave frequency. This microwave setup allows continuous tuning from 5.4 GHz (limited by the upconverter minimum local oscillator frequency) to beyond 9.8 GHz (this was limited by the QD maximum polarisation). This is done by tuning the frequency of the Rohde & Schwarz source.

Bibliography

- [1] Schrödinger, E. Quantisierung als Eigenwertproblem. *Annalen der Physik* **384**, 361–376 (1926).
- [2] Planck, M. Ueber eine Verbesserung der Wien’schen Spectralgleichung. *Verhandlungen der Deutschen Physikalischen Gesellschaft* **2**, 202–204 (1900).
- [3] Davisson, C. J. & Germer, L. H. Reflection of Electrons by a Crystal of Nickel. *Proceedings of the National Academy of Sciences of the United States of America* **14**, 317–22 (1928).
- [4] Millikan, R. A. On the elementary electrical charge and the avogadro constant. *Physical Review* **2**, 109–143 (1913).
- [5] Millikan, R. A. A Direct Determination of “ h ”. *Physical Review* **4**, 73–75 (1914).
- [6] Aspect, A., Dalibard, J. & Roger, G. Experimental test of Bell’s inequalities using time-varying analyzers. *Physical Review Letters* **49**, 1804–1807 (1982).
- [7] Hensen, B. *et al.* Loophole-free Bell inequality violation using electron spins separated by 1.3 kilometres. *Nature* **526**, 682–686 (2015).
- [8] Anderson, M. H., Ensher, J. R., Matthews, M. R., Wieman, C. E. & Cornell, E. A. Observation of Bose-Einstein Condensation in a Dilute Atomic Vapor. *Science* **269**, 198–201 (1995).
- [9] Davis, K. B. *et al.* Bose-Einstein condensation in a gas of sodium atoms. *Physical Review Letters* **75**, 3969–3973 (1995).
- [10] Feynman, R. P. Simulating Physics with Computers. *International Journal of Theoretical Physics* **217** (1982).

- [11] DiVincenzo, D. P. The Physical Implementation of Quantum Computation. *Fortschritte der Physik* **48**, 771–783 (2000).
- [12] Deutsch, D. & Jozsa, R. Rapid Solution of Problems by Quantum Computation. *Proceedings of the Royal Society A: Mathematical, Physical and Engineering Sciences* **439**, 553–558 (1992).
- [13] Grover, L. K. & K., L. A fast quantum mechanical algorithm for database search. In *Proceedings of the twenty-eighth annual ACM symposium on Theory of computing - STOC '96*, 212–219 (ACM Press, New York, New York, USA, 1996).
- [14] Shor, P. & W., P. Algorithms for quantum computation: discrete logarithms and factoring. In *Proceedings 35th Annual Symposium on Foundations of Computer Science*, 124–134 (IEEE Comput. Soc. Press, 1994).
- [15] Bennett, C. H. & Brassard, G. Quantum cryptography: Public key distribution and coin tossing. *Proceedings of IEEE International Conference on Computers, Systems, and Signal Processing* **1**, 175–179 (1984).
- [16] Kimble, H. J. The quantum internet. *Nature* **453**, 1023–1030 (2008).
- [17] Cirac, J. I., Zoller, P., Kimble, H. J. & Mabuchi, H. Quantum State Transfer and Entanglement Distribution among Distant Nodes in a Quantum Network. *Physical Review Letters* **78**, 3221–3224 (1997).
- [18] Cirac, J. I. & Zoller, P. Quantum computations with cold trapped ions. *Physical Review Letters* **74**, 4091–4094 (1995).
- [19] Sørensen, A. & Mølmer, K. Quantum computation with ions in thermal motion. *Physical Review Letters* **82**, 1971–1974 (1999).
- [20] Kielpinski, D., Monroe, C. & Wineland, D. J. Architecture for a large-scale ion-trap quantum computer. *Nature* **417**, 709–711 (2002).
- [21] Devoret, M. H., Martinis, J. M. & Clarke, J. Measurements of Macroscopic Quantum Tunneling out of the Zero-Voltage State of a Current-Biased Josephson Junction. *Physical Review Letters* **55**, 1908–1911 (1985).
- [22] Koch, J. *et al.* Charge-insensitive qubit design derived from the Cooper pair box. *Physical Review A* **76**, 042319 (2007).

- [23] You, J. Q. & Nori, F. Atomic physics and quantum optics using superconducting circuits. *Nature* **474**, 589–597 (2011).
- [24] Arute, F. *et al.* Quantum supremacy using a programmable superconducting processor. *Nature* **574**, 505–510 (2019).
- [25] Zwanenburg, F. A. *et al.* Silicon quantum electronics. *Reviews of Modern Physics* **85**, 961–1019 (2013).
- [26] Yang, C. H. *et al.* Operation of a silicon quantum processor unit cell above one kelvin. *Nature* **580**, 350–354 (2020).
- [27] Hanson, R. & Awschalom, D. D. Coherent manipulation of single spins in semiconductors. *Nature* **453**, 1043–1049 (2008).
- [28] Pompili, M. *et al.* Realization of a multinode quantum network of remote solid-state qubits. *Science* **372**, 259–264 (2021).
- [29] Xia, F., Wang, H., Xiao, D., Dubey, M. & Ramasubramaniam, A. Two-dimensional material nanophotonics. *Nature Photonics* **8**, 899–907 (2014).
- [30] Hanson, R., Kouwenhoven, L. P., Petta, J. R., Tarucha, S. & Vandersypen, L. M. Spins in few-electron quantum dots. *Reviews of Modern Physics* **79**, 1217–1265 (2007).
- [31] Loss, D. & DiVincenzo, D. P. Quantum computation with quantum dots. *Physical Review A* **57**, 120–126 (1998).
- [32] Wolf, S. A. Spintronics: A Spin-Based Electronics Vision for the Future. *Science* **294**, 1488–1495 (2001).
- [33] DiVincenzo, D. P. Quantum Computation. *Science* **270**, 255–261 (1995).
- [34] Briegel, H. J. & Raussendorf, R. Persistent entanglement in arrays of interacting particles. *Physical Review Letters* **86**, 910–913 (2001).
- [35] Lindner, N. H. & Rudolph, T. Proposal for pulsed On-demand sources of photonic cluster state strings. *Physical Review Letters* **103** (2009).
- [36] Economou, S. E., Lindner, N. & Rudolph, T. Optically generated 2-dimensional photonic cluster state from coupled quantum dots. *Physical Review Letters* **105** (2010).

- [37] Schwartz, I. *et al.* Deterministic generation of a cluster state of entangled photons. *Science* **354**, 434–437 (2016).
- [38] Atatüre, M. *et al.* Quantum-Dot Spin-State Preparation with Near-Unity Fidelity. *Science* **312**, 551–553 (2006).
- [39] Heiss, D. *et al.* Observation of extremely slow hole spin relaxation in self-assembled quantum dots. *Physical Review B* **76**, 241306 (2007).
- [40] Gerardot, B. D. *et al.* Optical pumping of a single hole spin in a quantum dot. *Nature* **451**, 441–444 (2008).
- [41] Berezovsky, J., Mikkelsen, M. H., Stoltz, N. G., Coldren, L. A. & Awschalom, D. D. Picosecond Coherent Optical Manipulation of a Single Electron Spin in a Quantum Dot. *Science* **320**, 349–352 (2008).
- [42] Press, D., Ladd, T. D., Zhang, B. & Yamamoto, Y. Complete quantum control of a single quantum dot spin using ultrafast optical pulses. *Nature* **456**, 218–221 (2008).
- [43] Gurudev Dutt, M. V. *et al.* Ultrafast optical control of electron spin coherence in charged GaAs quantum dots. *Physical Review B* **74**, 125306 (2006).
- [44] Vamivakas, A. N. *et al.* Observation of spin-dependent quantum jumps via quantum dot resonance fluorescence. *Nature* **467**, 297–300 (2010).
- [45] Delteil, A., Gao, W.-b., Fallahi, P., Miguel-Sanchez, J. & Imamoglu, A. Observation of Quantum Jumps of a Single Quantum Dot Spin Using Submicrosecond Single-Shot Optical Readout. *Physical Review Letters* **112**, 116802 (2014).
- [46] De Greve, K. *et al.* Quantum-dot spin–photon entanglement via frequency downconversion to telecom wavelength. *Nature* **491**, 421–425 (2012).
- [47] Gao, W. B., Fallahi, P., Togan, E., Miguel-Sanchez, J. & Imamoglu, A. Observation of entanglement between a quantum dot spin and a single photon. *Nature* **491**, 426–430 (2012).
- [48] Schaibley, J. R. *et al.* Demonstration of Quantum Entanglement between a Single Electron Spin Confined to an InAs Quantum Dot and a Photon. *Physical Review Letters* **110**, 167401 (2013).

- [49] Stockill, R. *et al.* Phase-Tuned Entangled State Generation between Distant Spin Qubits. *Physical Review Letters* **119**, 010503 (2017).
- [50] Delteil, A. *et al.* Generation of heralded entanglement between distant hole spins. *Nature Physics* **12**, 218–223 (2016).
- [51] Arthur, J. R. & LePore, J. J. GaAs, GaP, and GaAs_xP_{1-x} Epitaxial Films Grown by Molecular Beam Deposition. *Journal of Vacuum Science and Technology* **6**, 545–548 (1969).
- [52] Cho, A. Y. & Arthur, J. R. Molecular Beam Epitaxy. *Progress in Solid-State Chemistry* **10**, 157–191 (1975).
- [53] Reed, M. A. Spatial quantization in GaAs–AlGaAs multiple quantum dots. *Journal of Vacuum Science and Technology B: Microelectronics and Nanometer Structures* **4**, 358 (1986).
- [54] Cibert, J. *et al.* Optically detected carrier confinement to one and zero dimension in GaAs quantum well wires and boxes. *Applied Physics Letters* **49**, 1275–1277 (1986).
- [55] Sikorski, C. & Merkt, U. Spectroscopy of electronic states in InSb quantum dots. *Physical Review Letters* **62**, 2164–2167 (1989).
- [56] Brunner, K. *et al.* Photoluminescence from a single GaAs/AlGaAs quantum dot. *Physical Review Letters* **69**, 3216–3219 (1992).
- [57] Marzin, J. Y., Gérard, J. M., Izraël, A., Barrier, D. & Bastard, G. Photoluminescence of Single InAs Quantum Dots Obtained by Self-Organized Growth on GaAs. *Physical Review Letters* **73**, 716–719 (1994).
- [58] Banin, U. *et al.* Size-dependent electronic level structure of InAs nanocrystal quantum dots: Test of multiband effective mass theory. *The Journal of Chemical Physics* **109**, 2306–2309 (1998).
- [59] Banin, U., Cao, Y., Katz, D. & Millo, O. Identification of atomic-like electronic states in indium arsenide nanocrystal quantum dots. *Nature* **400**, 542–544 (1999).
- [60] Alivisatos, A. P. Semiconductor Clusters, Nanocrystals, and Quantum Dots. *Science* **271**, 933–937 (1996).
- [61] Kastner, M. A. Artificial Atoms. *Physics Today* **46**, 24–31 (1993).

- [62] Ashoori, R. C. Electrons in artificial atoms. *Nature* **379**, 413–419 (1996).
- [63] Petroff, P. M., Lorke, A. & Imamoglu, A. Epitaxially Self-Assembled Quantum Dots. *Physics Today* **54**, 46–52 (2001).
- [64] Stranski, I. N. & Krastanow, L. Berichtigung zur Arbeit. *Monatshefte für Chemie* **72**, 76–76 (1939).
- [65] Shchukin, V. A. & Bimberg, D. Spontaneous ordering of nanostructures on crystal surfaces. *Reviews of Modern Physics* **71**, 1125–1171 (1999).
- [66] Schaffer, W. J., Lind, M. D., Kowalczyk, S. P. & Grant, R. W. Nucleation and strain relaxation at the InAs/GaAs(100) heterojunction. *Journal of Vacuum Science and Technology B: Microelectronics and Nanometer Structures* **1**, 688 (1983).
- [67] Grunthaner, F. J. *et al.* Molecular beam epitaxial growth and transmission electron microscopy studies of thin GaAs/InAs(100) multiple quantum well structures. *Applied Physics Letters* **46**, 983–985 (1985).
- [68] Gerard, J. *In situ* probing at the growth temperature of the surface composition of (InGa)As and (InAl)As. *Applied Physics Letters* **61**, 2096–2098 (1992).
- [69] Goldstein, L., Glas, F., Marzin, J. Y., Charasse, M. N. & Le Roux, G. Growth by molecular beam epitaxy and characterization of InAs/GaAs strained-layer superlattices. *Applied Physics Letters* **47**, 1099–1101 (1985).
- [70] Brandt, O. *et al.* Structural and optical properties of (100) InAs single-monolayer quantum wells in bulklike GaAs grown by molecular-beam epitaxy. *Physical Review B* **41**, 12599–12606 (1990).
- [71] Leonard, D., Krishnamurthy, M., Reaves, C. M., Denbaars, S. P. & Petroff, P. M. Direct formation of quantum-sized dots from uniform coherent islands of InGaAs on GaAs surfaces. *Applied Physics Letters* **63**, 3203–3205 (1993).
- [72] Yeh, P. *Optical waves in layered media* (Wiley, 2005).
- [73] Marple, D. T. F. Refractive Index of GaAs. *Journal of Applied Physics* **35**, 1241–1242 (1964).

- [74] Zwiller, V. & Björk, G. Improved light extraction from emitters in high refractive index materials using solid immersion lenses. *Journal of Applied Physics* **92**, 660–665 (2002).
- [75] Mansfield, S. M. & Kino, G. S. Solid immersion microscope. *Applied Physics Letters* **57**, 2615–2616 (1990).
- [76] Koyama, K., Yoshita, M., Baba, M., Suemoto, T. & Akiyama, H. High collection efficiency in fluorescence microscopy with a solid immersion lens. *Applied Physics Letters* **75**, 1667–1669 (1999).
- [77] Barnes, W. *et al.* Solid-state single photon sources: light collection strategies. *The European Physical Journal D - Atomic, Molecular and Optical Physics* **18**, 197–210 (2002).
- [78] Drexler, H., Leonard, D., Hansen, W., Kotthaus, J. P. & Petroff, P. M. Spectroscopy of quantum levels in charge-tunable InGaAs quantum dots. *Physical Review Letters* **73**, 2252–2255 (1994).
- [79] Warburton, R. J. *et al.* Optical emission from a charge-tunable quantum ring. *Nature* **405**, 926–929 (2000).
- [80] Högele, A. *et al.* Voltage-Controlled Optics of a Quantum Dot. *Physical Review Letters* **93**, 217401 (2004).
- [81] Stark, J. Beobachtungen über den Effekt des elektrischen Feldes auf Spektrallinien. I. Quereffekt. *Annalen der Physik* **348**, 965–982 (1914).
- [82] Gywat, O., Krenner, H. J. & Berezovsky, J. *Spins in Optically Active Quantum Dots: Concepts and Methods* (Wiley-VCH Verlag GmbH and Co. KGaA, Weinheim, Germany, 2010).
- [83] Finley, J. J. *et al.* Fine structure of charged and neutral excitons in InAs-Al_{0.6}Ga_{0.4}As quantum dots. *Physical Review B* **66**, 153316 (2002).
- [84] Bayer, M. *et al.* Fine structure of neutral and charged excitons in self-assembled In(Ga)As/(Al)GaAs quantum dots. *Physical Review B* **65**, 195315 (2002).
- [85] Krizhanovskii, D. N. *et al.* Individual neutral and charged In_xGa_{1-x}As-GaAs quantum dots with strong in-plane optical anisotropy. *Physical Review B* **72**, 161312 (2005).

- [86] Warburton, R. J. Single spins in self-assembled quantum dots. *Nature Materials* **12**, 483–493 (2013).
- [87] Borri, P. *et al.* Ultralong Dephasing Time in InGaAs Quantum Dots. *Physical Review Letters* **87**, 157401 (2001).
- [88] Ramsay, A. J. *et al.* Phonon-Induced Rabi-Frequency Renormalization of Optically Driven Single InGaAs / GaAs Quantum Dots. *Physical Review Letters* **105**, 177402 (2010).
- [89] Ramsay, A. J. *et al.* Damping of Exciton Rabi Rotations by Acoustic Phonons in Optically Excited InGaAs / GaAs Quantum Dots. *Physical Review Letters* **104**, 017402 (2010).
- [90] Kuhlmann, A. V. *et al.* A dark-field microscope for background-free detection of resonance fluorescence from single semiconductor quantum dots operating in a set-and-forget mode. *Review of Scientific Instruments* **84**, 073905 (2013).
- [91] Carmichael, H. J. & Walls, D. F. A quantum-mechanical master equation treatment of the dynamical Stark effect. *Journal of Physics B: Atomic and Molecular Physics* **9**, 1199–1219 (1976).
- [92] Mollow, B. Power Spectrum of Light Scattered by Two-Level Systems. *Physical Review* **188**, 1969–1975 (1969).
- [93] Mollow, B. R. Resonant scattering of radiation from collision-damped two-level systems. *Physical Review A* **2**, 76–80 (1970).
- [94] Rabi, I. I., Zacharias, J. R., Millman, S. & Kusch, P. A New Method of Measuring Nuclear Magnetic Moment. *Physical Review* **53**, 318–318 (1938).
- [95] Autler, S. H. & Townes, C. H. Stark Effect in Rapidly Varying Fields. *Physical Review* **100**, 703–722 (1955).
- [96] Schabert, A., Keil, R. & Toschek, P. E. Dynamic stark effect of an optical line observed by cross-saturated absorption. *Applied Physics* **6**, 181–184 (1975).
- [97] Wu, F. Y., Grove, R. E. & Ezekiel, S. Investigation of the spectrum of resonance fluorescence induced by a monochromatic field. *Physical Review Letters* **35**, 1426–1429 (1975).

- [98] Xu, X. *et al.* Coherent Optical Spectroscopy of a Strongly Driven Quantum Dot. *Science* **317**, 929–932 (2007).
- [99] Flagg, E. B. *et al.* Resonantly driven coherent oscillations in a solid-state quantum emitter. *Nature Physics* **5**, 203–207 (2009).
- [100] Nick Vamivakas, A., Zhao, Y., Lu, C.-Y. & Atatüre, M. Spin-resolved quantum-dot resonance fluorescence. *Nature Physics* **5**, 198–202 (2009).
- [101] Kuhlmann, A. V. *et al.* Transform-limited single photons from a single quantum dot. *Nature Communications* **6**, 8204 (2015).
- [102] Dalgarno, P. A. *et al.* Coulomb interactions in single charged self-assembled quantum dots: Radiative lifetime and recombination energy. *Physical Review B* **77**, 245311 (2008).
- [103] Hansom, J. *et al.* Environment-assisted quantum control of a solid-state spin via coherent dark states. *Nature Physics* **10**, 725–730 (2014).
- [104] McCutcheon, D. P. S. Optical signatures of non-Markovian behavior in open quantum systems. *Physical Review A* **93**, 022119 (2016).
- [105] Konthasinghe, K. *et al.* Coherent versus incoherent light scattering from a quantum dot. *Physical Review B* **85**, 235315 (2012).
- [106] Matthiesen, C., Vamivakas, A. N. & Atatüre, M. Subnatural Linewidth Single Photons from a Quantum Dot. *Physical Review Letters* **108**, 093602 (2012).
- [107] Michler, P. A Quantum Dot Single-Photon Turnstile Device. *Science* **290**, 2282–2285 (2000).
- [108] Santori, C., Pelton, M., Solomon, G., Dale, Y. & Yamamoto, Y. Triggered Single Photons from a Quantum Dot. *Physical Review Letters* **86**, 1502–1505 (2001).
- [109] Santori, C., Fattal, D., Vučković, J., Solomon, G. S. & Yamamoto, Y. Indistinguishable photons from a single-photon device. *Nature* **419**, 594–597 (2002).
- [110] Shields, A. J. Semiconductor quantum light sources. *Nature Photonics* **1**, 215–223 (2007).

- [111] Besombes, L., Kheng, K., Marsal, L. & Mariette, H. Acoustic phonon broadening mechanism in single quantum dot emission. *Physical Review B* **63**, 155307 (2001).
- [112] Favero, I. *et al.* Acoustic phonon sidebands in the emission line of single InAs/GaAs quantum dots. *Physical Review B* **68**, 233301 (2003).
- [113] Houel, J. *et al.* Probing Single-Charge Fluctuations at a GaAs/AlAs Interface Using Laser Spectroscopy on a Nearby InGaAs Quantum Dot. *Physical Review Letters* **108**, 107401 (2012).
- [114] Kuhlmann, A. V. *et al.* Charge noise and spin noise in a semiconductor quantum device. *Nature Physics* **9**, 570–575 (2013).
- [115] Pechtel, J. H. *et al.* Frequency-Stabilized Source of Single Photons from a Solid-State Qubit. *Physical Review X* **3**, 041006 (2013).
- [116] Hansom, J., Schulte, C. H. H., Matthiesen, C., Stanley, M. J. & Atatüre, M. Frequency stabilization of the zero-phonon line of a quantum dot via phonon-assisted active feedback. *Applied Physics Letters* **105**, 172107 (2014).
- [117] Ates, S. *et al.* Post-Selected Indistinguishable Photons from the Resonance Fluorescence of a Single Quantum Dot in a Microcavity. *Physical Review Letters* **103**, 167402 (2009).
- [118] Liu, F. *et al.* High Purcell factor generation of indistinguishable on-chip single photons. *Nature Nanotechnology* **13**, 835–840 (2018).
- [119] Happ, T. D. *et al.* Enhanced light emission of $\text{In}_x\text{Ga}_{1-x}\text{As}$ quantum dots in a two-dimensional photonic-crystal defect microcavity. *Physical Review B* **66**, 041303 (2002).
- [120] Badolato, A. *et al.* Deterministic coupling of single quantum dots to single nanocavity modes. *Science* **308**, 1158–1161 (2005).
- [121] Kress, A. *et al.* Manipulation of the spontaneous emission dynamics of quantum dots in two-dimensional photonic crystals. *Physical Review B* **71**, 241304 (2005).
- [122] Ota, Y. *et al.* Enhanced photon emission and absorption of single quantum dot in resonance with two modes in photonic crystal nanocavity. *Applied Physics Letters* **93**, 183114 (2008).

- [123] Englund, D. *et al.* Controlling the Spontaneous Emission Rate of Single Quantum Dots in a Two-Dimensional Photonic Crystal. *Physical Review Letters* **95**, 013904 (2005).
- [124] Varoutsis, S. *et al.* Restoration of photon indistinguishability in the emission of a semiconductor quantum dot. *Physical Review B* **72**, 041303 (2005).
- [125] Nguyen, H. S. *et al.* Ultra-coherent single photon source. *Applied Physics Letters* **99**, 261904 (2011).
- [126] Matthiesen, C. *et al.* Phase-locked indistinguishable photons with synthesized waveforms from a solid-state source. *Nature Communications* **4**, 1600 (2013).
- [127] Kiraz, A., Atatüre, M. & Imamoglu, A. Quantum-dot single-photon sources: Prospects for applications in linear optics quantum-information processing. *Physical Review A* **69**, 032305 (2004).
- [128] Gschrey, M. *et al.* Highly indistinguishable photons from deterministic quantum-dot microlenses utilizing three-dimensional in situ electron-beam lithography. *Nature Communications* **6**, 7662 (2015).
- [129] Gazzano, O. *et al.* Bright solid-state sources of indistinguishable single photons. *Nature Communications* **4**, 1425 (2013).
- [130] Somaschi, N. *et al.* Near-optimal single-photon sources in the solid state. *Nature Photonics* **10**, 340–345 (2016).
- [131] Senellart, P., Solomon, G. & White, A. High-performance semiconductor quantum-dot single-photon sources. *Nature Nanotechnology* **12**, 1026–1039 (2017).
- [132] Muller, A. *et al.* Resonance fluorescence from a coherently driven semiconductor quantum dot in a cavity. *Physical Review Letters* **99**, 187402 (2007).
- [133] Shirley, J. H. Solution of the Schrödinger Equation with a Hamiltonian Periodic in Time. *Physical Review* **138**, B979–B987 (1965).
- [134] Allen, L. L. & Eberly, J. H. *Optical resonance and two-level atoms* (Dover, 1987).

- [135] Smith, J. M. *et al.* Voltage Control of the Spin Dynamics of an Exciton in a Semiconductor Quantum Dot. *Physical Review Letters* **94**, 197402 (2005).
- [136] Dreiser, J. *et al.* Optical investigations of quantum dot spin dynamics as a function of external electric and magnetic fields. *Physical Review B* **77**, 075317 (2008).
- [137] Yilmaz, S. T., Fallahi, P. & Imamoglu, A. Quantum-Dot-Spin Single-Photon Interface. *Physical Review Letters* **105**, 033601 (2010).
- [138] Pryor, C. E. & Flatté, M. E. Predicted ultrafast single-qubit operations in semiconductor quantum dots. *Applied Physics Letters* **88**, 233108 (2006).
- [139] Schwan, A. *et al.* Anisotropy of electron and hole g-factors in (In,Ga)As quantum dots. *Applied Physics Letters* **99**, 221914 (2011).
- [140] Rietjens, J. H. *et al.* Optical control over electron g factor and spin decoherence in (In,Ga) AsGaAs quantum dots. *Journal of Applied Physics* **103**, 07B116 (2008).
- [141] Koppens, F. H. L. *et al.* Driven coherent oscillations of a single electron spin in a quantum dot. *Nature* **442**, 766–771 (2006).
- [142] Nowack, K. C., Koppens, F. H. L., Nazarov, Y. V. & Vandersypen, L. M. K. Coherent Control of a Single Electron Spin with Electric Fields. *Science* **318**, 1430–1433 (2007).
- [143] Tokura, Y., van der Wiel, W. G., Obata, T. & Tarucha, S. Coherent Single Electron Spin Control in a Slanting Zeeman Field. *Physical Review Letters* **96**, 047202 (2006).
- [144] Koppens, F. H. L., Nowack, K. C. & Vandersypen, L. M. K. Spin Echo of a Single Electron Spin in a Quantum Dot. *Physical Review Letters* **100**, 236802 (2008).
- [145] Chen, P., Piermarocchi, C., Sham, L. J., Gammon, D. & Steel, D. G. Theory of quantum optical control of a single spin in a quantum dot. *Physical Review B* **69**, 075320 (2004).
- [146] Clark, S. M., Fu, K.-M. C., Ladd, T. D. & Yamamoto, Y. Quantum Computers Based on Electron Spins Controlled by Ultrafast Off-Resonant Single Optical Pulses. *Physical Review Letters* **99**, 040501 (2007).

- [147] Carter, S. G., Chen, Z. & Cundiff, S. T. Ultrafast below-resonance Raman rotation of electron spins in GaAs quantum wells. *Physical Review B* **76**, 201308 (2007).
- [148] Imamoglu, A. *et al.* Quantum information processing using quantum dot spins and cavity qed. *Physical Review Letters* **83**, 4204–4207 (1999).
- [149] Combescot, M. & Betbeder-Matibet, O. Theory of spin precession monitored by laser pulse. *Solid State Communications* **132**, 129–134 (2004).
- [150] Economou, S. E., Sham, L. J., Wu, Y. & Steel, D. G. Proposal for optical U(1) rotations of electron spin trapped in a quantum dot. *Physical Review B* **74**, 205415 (2006).
- [151] De Greve, K. *et al.* Ultrafast coherent control and suppressed nuclear feedback of a single quantum dot hole qubit. *Nature Physics* **7**, 872–878 (2011).
- [152] Foot, C. J. *Atomic physics* (Oxford University Press, 2005).
- [153] Hahn, E. Spin Echoes. *Physical Review* **80**, 580–594 (1950).
- [154] Carr, H. Y. & Purcell, E. M. Effects of diffusion on free precession in nuclear magnetic resonance experiments. *Physical Review* **94**, 630–638 (1954).
- [155] Meiboom, S. & Gill, D. Modified spin-echo method for measuring nuclear relaxation times. *Review of Scientific Instruments* **29**, 688–691 (1958).
- [156] Stockill, R. *et al.* Quantum dot spin coherence governed by a strained nuclear environment. *Nature Communications* **7**, 12745 (2016).
- [157] Huthmacher, L. *et al.* Coherence of a dynamically decoupled quantum-dot hole spin. *Physical Review B* **97**, 241413 (2018).
- [158] Gaudin, M. Diagonalisation d’une classe d’hamiltoniens de spin. *Journal de Physique* **37**, 1087–1098 (1976).
- [159] Bortz, M. & Stolze, J. Spin and entanglement dynamics in the central-spin model with homogeneous couplings. *Journal of Statistical Mechanics: Theory and Experiment* **2007**, P06018–P06018 (2007).

- [160] Schliemann, J., Khaetskii, A. & Loss, D. Electron spin dynamics in quantum dots and related nanostructures due to hyperfine interaction with nuclei. *Journal of Physics: Condensed Matter* **15**, R1809–R1833 (2003).
- [161] Kane, B. E. A silicon-based nuclear spin quantum computer. *Nature* **393**, 133–137 (1998).
- [162] Merkulov, I. A., Efros, A. L. & Rosen, M. Electron spin relaxation by nuclei in semiconductor quantum dots. *Physical Review B* **65**, 1–8 (2002).
- [163] Urbaszek, B. *et al.* Nuclear spin physics in quantum dots: An optical investigation. *Reviews of Modern Physics* **85**, 79–133 (2013).
- [164] Abragam, A. *The principles of nuclear magnetism*, vol. 28 (Clarendon Press, 1961).
- [165] Gammon, D. *et al.* Electron and Nuclear Spin Interactions in the Optical Spectra of Single GaAs Quantum Dots. *Physical Review Letters* **86**, 5176–5179 (2001).
- [166] Testelin, C., Bernardot, F., Eble, B. & Chamarro, M. Hole–spin dephasing time associated with hyperfine interaction in quantum dots. *Physical Review B* **79**, 195440 (2009).
- [167] Overhauser, A. W. Polarization of nuclei in metals. *Physical Review* **92**, 411–415 (1953).
- [168] Paget, D., Lampel, G., Sapoval, B. & Safarov, V. I. Low field electron–nuclear spin coupling in gallium arsenide under optical pumping conditions. *Physical Review B* **15**, 5780–5796 (1977).
- [169] Fischer, J., Coish, W. A., Bulaev, D. V. & Loss, D. Spin decoherence of a heavy hole coupled to nuclear spins in a quantum dot. *Physical Review B* **78**, 155329 (2008).
- [170] Fallahi, P., Yılmaz, S. T. & Imamoglu, A. Measurement of a Heavy-Hole Hyperfine Interaction in InGaAs Quantum Dots Using Resonance Fluorescence. *Physical Review Letters* **105**, 257402 (2010).
- [171] Denning, E. V., Gangloff, D. A., Atatüre, M., Mørk, J. & Le Gall, C. Collective Quantum Memory Activated by a Driven Central Spin. *Physical Review Letters* **123**, 140502 (2019).

- [172] Bulutay, C. Quadrupolar spectra of nuclear spins in strained $\text{In}_x\text{Ga}_{1-x}\text{As}$ quantum dots. *Physical Review B* **85**, 115313 (2012).
- [173] Huang, C.-W. & Hu, X. Theoretical study of nuclear spin polarization and depolarization in self-assembled quantum dots. *Physical Review B* **81**, 205304 (2010).
- [174] Schrieffer, J. R. & Wolff, P. A. Relation between the Anderson model and the Kondo Hamiltonians. *Physical Review* **149**, 491 (1966).
- [175] Klauser, D., Coish, W. A. & Loss, D. Nuclear spin dynamics and Zeno effect in quantum dots and defect centers. *Physical Review B* **78**, 205301 (2008).
- [176] Gangloff, D. A. *et al.* Quantum interface of an electron and a nuclear ensemble. *Science* **364**, 62–66 (2019).
- [177] Latta, C., Srivastava, A. & Imamoğlu, A. Hyperfine Interaction-Dominated Dynamics of Nuclear Spins in Self-Assembled InGaAs Quantum Dots. *Physical Review Letters* **107**, 167401 (2011).
- [178] Högele, A. *et al.* Dynamic Nuclear Spin Polarization in the Resonant Laser Excitation of an InGaAs Quantum Dot. *Physical Review Letters* **108**, 197403 (2012).
- [179] Kroutvar, M. *et al.* Optically programmable electron spin memory using semiconductor quantum dots. *Nature* **432**, 81–84 (2004).
- [180] Khaetskii, A. V., Loss, D. & Glazman, L. Electron Spin Decoherence in Quantum Dots due to Interaction with Nuclei. *Physical Review Letters* **88**, 186802 (2002).
- [181] Yao, W., Liu, R.-B. & Sham, L. J. Theory of electron spin decoherence by interacting nuclear spins in a quantum dot. *Physical Review B* **74**, 195301 (2006).
- [182] Cywiński, L., Witzel, W. M. & Das Sarma, S. Electron Spin Dephasing due to Hyperfine Interactions with a Nuclear Spin Bath. *Physical Review Letters* **102**, 057601 (2009).
- [183] Ramsey, N. F. A molecular beam resonance method with separated oscillating fields. *Physical Review* **78**, 695–699 (1950).

- [184] Barthel, C., Reilly, D. J., Marcus, C. M., Hanson, M. P. & Gossard, A. C. Rapid Single-Shot Measurement of a Singlet-Triplet Qubit. *Physical Review Letters* **103**, 160503 (2009).
- [185] Éthier-Majcher, G. *et al.* Improving a Solid-State Qubit through an Engineered Mesoscopic Environment. *Physical Review Letters* **119**, 130503 (2017).
- [186] Faribault, A. & Schuricht, D. Spin decoherence due to a randomly fluctuating spin bath. *Physical Review B* **88**, 085323 (2013).
- [187] Braun, P.-F. *et al.* Direct Observation of the Electron Spin Relaxation Induced by Nuclei in Quantum Dots. *Physical Review Letters* **94**, 116601 (2005).
- [188] Dou, X. M., Sun, B. Q., Jiang, D. S., Ni, H. Q. & Niu, Z. C. Electron spin relaxation in a single InAs quantum dot measured by tunable nuclear spins. *Physical Review B* **84**, 033302 (2011).
- [189] Bechtold, A. *et al.* Three-stage decoherence dynamics of an electron spin qubit in an optically active quantum dot. *Nature Physics* **11**, 1005–1008 (2015).
- [190] Johnson, A. C. *et al.* Triplet-singlet spin relaxation via nuclei in a double quantum dot. *Nature* **435**, 925–928 (2005).
- [191] Grelich, A., Carter, S. G., Kim, D., Bracker, A. S. & Gammon, D. Optical control of one and two hole spins in interacting quantum dots. *Nature Photonics* **5**, 702–708 (2011).
- [192] Godden, T. M. *et al.* Coherent Optical Control of the Spin of a Single Hole in an InAs / GaAs Quantum Dot. *Physical Review Letters* **108**, 017402 (2012).
- [193] Cywiński, L., Lutchyn, R. M., Nave, C. P. & Das Sarma, S. How to enhance dephasing time in superconducting qubits. *Physical Review B* **77**, 174509 (2008).
- [194] Álvarez, G. A., Ajoy, A., Peng, X. & Suter, D. Performance comparison of dynamical decoupling sequences for a qubit in a rapidly fluctuating spin bath. *Physical Review A* **82**, 042306 (2010).
- [195] Ajoy, A., Álvarez, G. A. & Suter, D. Optimal pulse spacing for dynamical decoupling in the presence of a purely dephasing spin bath. *Physical Review A* **83**, 032303 (2011).

- [196] Cywiński, Ł. Dynamical-decoupling noise spectroscopy at an optimal working point of a qubit. *Physical Review A* **90**, 042307 (2014).
- [197] Bluhm, H. *et al.* Dephasing time of GaAs electron-spin qubits coupled to a nuclear bath exceeding 200 μ s. *Nature Physics* **7**, 109–113 (2011).
- [198] Malinowski, F. K. *et al.* Spectrum of the Nuclear Environment for GaAs Spin Qubits. *Physical Review Letters* **118**, 177702 (2017).
- [199] Szańkowski, P., Ramon, G., Krzywda, J., Kwiatkowski, D. & Cywiński, Ł. Environmental noise spectroscopy with qubits subjected to dynamical decoupling. *Journal of Physics: Condensed Matter* **29**, 333001 (2017).
- [200] Malinowski, F. K. *et al.* Notch filtering the nuclear environment of a spin qubit. *Nature Nanotechnology* **12**, 16–20 (2017).
- [201] Martinis, J. M., Nam, S., Aumentado, J., Lang, K. M. & Urbina, C. Decoherence of a superconducting qubit due to bias noise. *Physical Review B* **67**, 094510 (2003).
- [202] Kabytaye, C. *et al.* Robustness of composite pulses to time-dependent control noise. *Physical Review A* **90**, 012316 (2014).
- [203] Álvarez, G. A. & Suter, D. Measuring the Spectrum of Colored Noise by Dynamical Decoupling. *Physical Review Letters* **107**, 230501 (2011).
- [204] Abobeih, M. H. *et al.* One-second coherence for a single electron spin coupled to a multi-qubit nuclear-spin environment. *Nature Communications* **9**, 2552 (2018).
- [205] Biercuk, M. J., Doherty, A. C. & Uys, H. Dynamical decoupling sequence construction as a filter-design problem. *Journal of Physics B: Atomic, Molecular and Optical Physics* **44**, 154002 (2011).
- [206] Soare, A. *et al.* Experimental noise filtering by quantum control. *Nature Physics* **10**, 825–829 (2014).
- [207] Chekhovich, E. A., da Silva, S. F. & Rastelli, A. Nuclear spin quantum register in an optically active semiconductor quantum dot. *Nature Nanotechnology* **15**, 999–1004 (2020).

- [208] Vandersypen, L. M. K. & Chuang, I. L. NMR techniques for quantum control and computation. *Reviews of Modern Physics* **76**, 1037–1069 (2005).
- [209] Gullion, T., Baker, D. B. & Conradi, M. S. New, compensated Carr-Purcell sequences. *Journal of Magnetic Resonance (1969)* **89**, 479–484 (1990).
- [210] Petta, J. R. *et al.* Coherent Manipulation of Coupled Electron Spins in Semiconductor Quantum Dots. *Science* **309**, 2180–2184 (2005).
- [211] Brunner, D. *et al.* A Coherent Single-Hole Spin in a Semiconductor. *Science* **325**, 70–72 (2009).
- [212] Houel, J. *et al.* High Resolution Coherent Population Trapping on a Single Hole Spin in a Semiconductor Quantum Dot. *Physical Review Letters* **112**, 107401 (2014).
- [213] Prechtel, J. H. *et al.* Decoupling a hole spin qubit from the nuclear spins. *Nature Materials* **15**, 981–986 (2016).
- [214] Monroe, C., Meekhof, D. M., King, B. E., Itano, W. M. & Wineland, D. J. Demonstration of a Fundamental Quantum Logic Gate. *Physical Review Letters* **75**, 4714–4717 (1995).
- [215] Golter, D. A. & Wang, H. Optically Driven Rabi Oscillations and Adiabatic Passage of Single Electron Spins in Diamond. *Physical Review Letters* **112**, 116403 (2014).
- [216] Delley, Y. L., Kroner, M., Faelt, S., Wegscheider, W. & Imamoglu, A. Deterministic entanglement between a propagating photon and a singlet-triplet qubit in an optically active quantum dot molecule. *Physical Review B* **96**, 241410 (2017).
- [217] Zhou, B. B. *et al.* Accelerated quantum control using superadiabatic dynamics in a solid-state lambda system. *Nature Physics* **13**, 330–334 (2017).
- [218] Becker, J. N. *et al.* All-Optical Control of the Silicon-Vacancy Spin in Diamond at Millikelvin Temperatures. *Physical Review Letters* **120**, 053603 (2018).
- [219] Goldman, M. L., Patti, T. L., Levonian, D., Yelin, S. F. & Lukin, M. D. Optical Control of a Single Nuclear Spin in the Solid State. *Physical Review Letters* **124**, 153203 (2020).

- [220] Ladd, T. D. *et al.* Pulsed Nuclear Pumping and Spin Diffusion in a Single Charged Quantum Dot. *Physical Review Letters* **105**, 107401 (2010).
- [221] Emerson, J., Alicki, R. & Życzkowski, K. Scalable noise estimation with random unitary operators. *Journal of Optics B: Quantum and Semiclassical Optics* **7**, S347–S352 (2005).
- [222] Lévi, B., López, C. C., Emerson, J. & Cory, D. G. Efficient error characterization in quantum information processing. *Physical Review A* **75**, 022314 (2007).
- [223] Dankert, C., Cleve, R., Emerson, J. & Livine, E. Exact and approximate unitary 2-designs and their application to fidelity estimation. *Physical Review A* **80**, 012304 (2009).
- [224] Bodey, J. H. *et al.* Optical spin locking of a solid-state qubit. *npj Quantum Information* **5**, 95 (2019).
- [225] Slichter, C. P. *Principles of Magnetic Resonance*, vol. 1 of *Springer Series in Solid-State Sciences* (Springer Berlin Heidelberg, Berlin, Heidelberg, 1978).
- [226] Chow, J. M. *et al.* Randomized Benchmarking and Process Tomography for Gate Errors in a Solid-State Qubit. *Physical Review Letters* **102**, 090502 (2009).
- [227] Levitt, M. H. Composite pulses. *Progress in Nuclear Magnetic Resonance Spectroscopy* **18**, 61–122 (1986).
- [228] Stepanenko, D., Burkard, G., Giedke, G. & Imamoglu, A. Enhancement of Electron Spin Coherence by Optical Preparation of Nuclear Spins. *Physical Review Letters* **96**, 136401 (2006).
- [229] Greulich, A. *et al.* Nuclei-Induced Frequency Focusing of Electron Spin Coherence. *Science* **317**, 1896–1899 (2007).
- [230] Reilly, D. J. *et al.* Suppressing Spin Qubit Dephasing by Nuclear State Preparation. *Science* **321**, 817–821 (2008).
- [231] Xu, X. *et al.* Coherent population trapping of an electron spin in a single negatively charged quantum dot. *Nature Physics* **4**, 692–695 (2008).

- [232] Bluhm, H., Foletti, S., Mahalu, D., Umansky, V. & Yacoby, A. Enhancing the Coherence of a Spin Qubit by Operating it as a Feedback Loop That Controls its Nuclear Spin Bath. *Physical Review Letters* **105**, 216803 (2010).
- [233] Issler, M. *et al.* Nuclear Spin Cooling Using Overhauser-Field Selective Coherent Population Trapping. *Physical Review Letters* **105**, 267202 (2010).
- [234] Heinzen, D. J. & Wineland, D. J. Quantum-limited cooling and detection of radio-frequency oscillations by laser-cooled ions. *Physical Review A* **42**, 2977–2994 (1990).
- [235] Wineland, D. J. & Itano, W. M. Laser cooling of atoms. *Physical Review A* **20**, 1521–1540 (1979).
- [236] Cummins, H. K., Llewellyn, G. & Jones, J. A. Tackling systematic errors in quantum logic gates with composite rotations. *Physical Review A* **67**, 042308 (2003).
- [237] Tycko, R., Cho, H., Schneider, E. & Pines, A. Composite pulses without phase distortion. *Journal of Magnetic Resonance (1969)* **61**, 90–101 (1985).
- [238] Jackson, D. M. *et al.* Quantum sensing of a coherent single spin excitation in a nuclear ensemble. *Nature Physics* **17**, 585–590 (2021).
- [239] Hartmann, S. R. & Hahn, E. L. Nuclear double resonance in the rotating frame. *Physical Review* **128**, 2042–2053 (1962).
- [240] Goldman, M. *Spin temperature and nuclear magnetic resonance in solids* (Clarendon Press, 1970).
- [241] Henstra, A., Dirksen, P., Schmidt, J. & Wenckebach, W. Nuclear spin orientation via electron spin locking (NOVEL). *Journal of Magnetic Resonance (1969)* **77**, 389–393 (1988).
- [242] Schwartz, I. *et al.* Robust optical polarization of nuclear spin baths using Hamiltonian engineering of nitrogen-vacancy center quantum dynamics. *Science Advances* **4**, eaat8978 (2018).
- [243] Miao, K. C. *et al.* Universal coherence protection in a solid-state spin qubit. *Science* **369**, 1493–1497 (2020).

- [244] Ludwig, A. *et al.* Ultra-low charge and spin noise in self-assembled quantum dots. *Journal of Crystal Growth* **477**, 193–196 (2017).
- [245] Matthiesen, C. *Coherent photons from a solid-state artificial atom*. Ph.D. thesis (2013).
- [246] Gangloff, D. A. *et al.* Revealing beyond-mean-field correlations in a nuclear ensemble via a proxy qubit. *To appear in Nature Physics* (2020).
- [247] Amico, L., Fazio, R., Osterloh, A. & Vedral, V. Entanglement in many-body systems. *Reviews of Modern Physics* **80**, 517–576 (2008).
- [248] Abanin, D. A., Altman, E., Bloch, I. & Serbyn, M. Colloquium : Many-body localization, thermalization, and entanglement. *Reviews of Modern Physics* **91**, 021001 (2019).
- [249] Kaufman, A. M. *et al.* Quantum thermalization through entanglement in an isolated many-body system. *Science* **353**, 794–800 (2016).
- [250] Shimazaki, Y. *et al.* Strongly correlated electrons and hybrid excitons in a moiré heterostructure. *Nature* **580**, 472–477 (2020).
- [251] Bakr, W. S., Gillen, J. I., Peng, A., Fölling, S. & Greiner, M. A quantum gas microscope for detecting single atoms in a Hubbard-regime optical lattice. *Nature* **462**, 74–77 (2009).
- [252] Haller, E. *et al.* Single-atom imaging of fermions in a quantum-gas microscope. *Nature Physics* **11**, 738–742 (2015).
- [253] Childress, L. *et al.* Coherent Dynamics of Coupled Electron and Nuclear Spin Qubits in Diamond. *Science* **314**, 281–285 (2006).
- [254] Pla, J. J. *et al.* High-fidelity readout and control of a nuclear spin qubit in silicon. *Nature* **496**, 334–338 (2013).
- [255] Taminiau, T. H., Cramer, J., Van Der Sar, T., Dobrovitski, V. V. & Hanson, R. Universal control and error correction in multi-qubit spin registers in diamond. *Nature Nanotechnology* **9**, 171–176 (2014).
- [256] Car, B., Veissier, L., Louchet-Chauvet, A., Le Gouët, J. L. & Chanelière, T. Selective Optical Addressing of Nuclear Spins through Superhyperfine Interaction in Rare-Earth Doped Solids. *Physical Review Letters* **120**, 197401 (2018).

- [257] Metsch, M. H. *et al.* Initialization and Readout of Nuclear Spins via a Negatively Charged Silicon-Vacancy Center in Diamond. *Physical Review Letters* **122**, 190503 (2019).
- [258] Bourassa, A. *et al.* Entanglement and control of single nuclear spins in isotopically engineered silicon carbide. *Nature Materials* **19**, 1319–1325 (2020).
- [259] Hensen, B. *et al.* A silicon quantum-dot-coupled nuclear spin qubit. *Nature Nanotechnology* **15**, 13–17 (2020).
- [260] Dicke, R. H. Coherence in spontaneous radiation processes. *Physical Review* **93**, 99–110 (1954).
- [261] Fleischhauer, M., Imamoglu, A. & Marangos, J. P. Electromagnetically induced transparency: Optics in coherent media. *Reviews of Modern Physics* **77**, 633–673 (2005).
- [262] Nikuni, T., Oshikawa, M., Oosawa, A. & Tanaka, H. Bose-Einstein condensation of dilute magnons in TlCuCl_3 . *Physical Review Letters* **84**, 5868–5871 (2000).
- [263] Muñoz, A., Klimov, A. B., Grassl, M. & Sánchez-Soto, L. L. Tomography from collective measurements. *Quantum Information Processing* **17**, 286 (2018).
- [264] Zhu, X. *et al.* Coherent coupling of a superconducting flux qubit to an electron spin ensemble in diamond. *Nature* **478**, 221–224 (2011).
- [265] Tabuchi, Y. *et al.* Coherent coupling between a ferromagnetic magnon and a superconducting qubit. *Science* **349**, 405–408 (2015).
- [266] Simon, J., Tanji, H., Thompson, J. K. & Vuletić, V. Interfacing Collective Atomic Excitations and Single Photons. *Physical Review Letters* **98**, 183601 (2007).
- [267] Mlynek, J. A., Abdumalikov, A. A., Eichler, C. & Wallraff, A. Observation of Dicke superradiance for two artificial atoms in a cavity with high decay rate. *Nature Communications* **5**, 5186 (2014).
- [268] Casabone, B. *et al.* Enhanced Quantum Interface with Collective Ion-Cavity Coupling. *Physical Review Letters* **114**, 023602 (2015).

- [269] Heidemann, R. *et al.* Evidence for Coherent Collective Rydberg Excitation in the Strong Blockade Regime. *Physical Review Letters* **99**, 163601 (2007).
- [270] Dudin, Y. O., Li, L., Bariani, F. & Kuzmich, A. Observation of coherent many-body Rabi oscillations. *Nature Physics* **8**, 790–794 (2012).
- [271] Ladd, T. D., Maryenko, D., Yamamoto, Y., Abe, E. & Itoh, K. M. Coherence time of decoupled nuclear spins in silicon. *Physical Review B* **71**, 014401 (2005).
- [272] Kondo, Y. *et al.* Multipulse Operation and Optical Detection of Nuclear Spin Coherence in a GaAs / AlGaAs Quantum Well. *Physical Review Letters* **101**, 207601 (2008).
- [273] Chekhovich, E., Hopkinson, M., Skolnick, M. & Tartakovskii, A. Suppression of nuclear spin bath fluctuations in self-assembled quantum dots induced by inhomogeneous strain. *Nature Communications* **6**, 6348 (2015).
- [274] Waldherr, G. *et al.* Quantum error correction in a solid-state hybrid spin register. *Nature* **506**, 204–207 (2014).
- [275] Kikkawa, J. M. & Awschalom, D. D. All-Optical Magnetic Resonance in Semiconductors. *Science* **287**, 473–476 (2000).
- [276] Jones, J. A., Mosca, M. & Hansen, R. H. Implementation of a quantum search algorithm on a quantum computer. *Nature* **393**, 344–346 (1998).
- [277] Leuenberger, M. N., Loss, D., Poggio, M. & Awschalom, D. D. Quantum Information Processing with Large Nuclear Spins in GaAs Semiconductors. *Physical Review Letters* **89**, 207601 (2002).
- [278] Kampermann, H. & Veeman, W. S. Characterization of quantum algorithms by quantum process tomography using quadrupolar spins in solid-state nuclear magnetic resonance. *The Journal of Chemical Physics* **122**, 214108 (2005).
- [279] Benjamin, S. C., Browne, D. E., Fitzsimons, J. & Morton, J. J. L. Brokered graph-state quantum computation. *New Journal of Physics* **8**, 141–141 (2006).

- [280] Roumpos, G., Master, C. P. & Yamamoto, Y. Quantum simulation of spin ordering with nuclear spins in a solid-state lattice. *Physical Review B* **75**, 094415 (2007).
- [281] Steane, A. & Lucas, D. Quantum Computing with Trapped Ions, Atoms and Light. *Fortschritte der Physik* **48**, 839–858 (2000).
- [282] Taylor, J. M., Marcus, C. M. & Lukin, M. D. Long-Lived Memory for Mesoscopic Quantum Bits. *Physical Review Letters* **90**, 206803 (2003).
- [283] Taylor, J. M., Imamoglu, A. & Lukin, M. D. Controlling a Mesoscopic Spin Environment by Quantum Bit Manipulation. *Physical Review Letters* **91**, 246802 (2003).
- [284] Kurucz, Z., Sørensen, M. W., Taylor, J. M., Lukin, M. D. & Fleischhauer, M. Qubit Protection in Nuclear-Spin Quantum Dot Memories. *Physical Review Letters* **103**, 010502 (2009).
- [285] van Loock, P. *et al.* Hybrid Quantum Repeater Using Bright Coherent Light. *Physical Review Letters* **96**, 240501 (2006).
- [286] Schwager, H., Cirac, J. I. & Giedke, G. Quantum interface between light and nuclear spins in quantum dots. *Physical Review B* **81**, 045309 (2010).
- [287] Witzel, W. M. & Das Sarma, S. Nuclear spins as quantum memory in semiconductor nanostructures. *Physical Review B* **76**, 045218 (2007).
- [288] Chekhovich, E. A. *et al.* Nuclear spin effects in semiconductor quantum dots. *Nature Materials* **12**, 494–504 (2013).
- [289] Coish, W. A. & Baugh, J. Nuclear spins in nanostructures. *Physica Status Solidi (B) Basic Research* **246**, 2203–2215 (2009).
- [290] Rudner, M. S., Vandersypen, L. M. K., Vuletić, V. & Levitov, L. S. Generating Entanglement and Squeezed States of Nuclear Spins in Quantum Dots. *Physical Review Letters* **107**, 206806 (2011).
- [291] Kessler, E. M. *et al.* Dissipative phase transition in a central spin system. *Physical Review A* **86**, 012116 (2012).
- [292] Chow, C. M. *et al.* Nonlocal Nuclear Spin Quieting in Quantum Dot Molecules: Optically Induced Extended Two-Electron Spin Coherence Time. *Physical Review Letters* **117**, 077403 (2016).

- [293] Sun, B. *et al.* Persistent Narrowing of Nuclear-Spin Fluctuations in InAs Quantum Dots Using Laser Excitation. *Physical Review Letters* **108**, 187401 (2012).
- [294] Braun, P.-F. *et al.* Bistability of the nuclear polarization created through optical pumping in $\text{In}_{1-x}\text{Ga}_x\text{As}$ quantum. *Physical Review B* **74**, 245306 (2006).
- [295] Eble, B. *et al.* Dynamic nuclear polarization of a single charge-tunable InAs / GaAs quantum dot. *Physical Review B* **74**, 081306 (2006).
- [296] Maletinsky, P., Badolato, A. & Imamoglu, A. Dynamics of Quantum Dot Nuclear Spin Polarization Controlled by a Single Electron. *Physical Review Letters* **99**, 056804 (2007).
- [297] Tartakovskii, A. I. *et al.* Nuclear Spin Switch in Semiconductor Quantum Dots. *Physical Review Letters* **98**, 026806 (2007).
- [298] Latta, C. *et al.* Confluence of resonant laser excitation and bidirectional quantum-dot nuclear-spin polarization. *Nature Physics* **5**, 758–763 (2009).
- [299] Chekhovich, E. A. *et al.* Pumping of Nuclear Spins by Optical Excitation of Spin-Forbidden Transitions in a Quantum Dot. *Physical Review Letters* **104**, 066804 (2010).
- [300] Puebla, J. *et al.* Dynamic nuclear polarization in InGaAs/GaAs and GaAs/AlGaAs quantum dots under nonresonant ultralow-power optical excitation. *Physical Review B* **88**, 045306 (2013).
- [301] Ulhaq, A. *et al.* Vanishing electron g factor and long-lived nuclear spin polarization in weakly strained nanohole-filled GaAs/AlGaAs quantum dots. *Physical Review B* **93**, 165306 (2016).
- [302] Burkard, G., Loss, D. & DiVincenzo, D. P. Coupled quantum dots as quantum gates. *Physical Review B* **59**, 2070–2078 (1999).
- [303] Coish, W. A. & Loss, D. Hyperfine interaction in a quantum dot: Non-Markovian electron spin dynamics. *Physical Review B* **70**, 195340 (2004).
- [304] Gammon, D. *et al.* Nuclear Spectroscopy in Single Quantum Dots: Nanoscopic Raman Scattering and Nuclear Magnetic Resonance. *Science* **277**, 85–88 (1997).

- [305] Makhonin, M. N. *et al.* Fast control of nuclear spin polarization in an optically pumped single quantum dot. *Nature Materials* **10**, 844–848 (2011).
- [306] Makhonin, M. N. *et al.* Optically tunable nuclear magnetic resonance in a single quantum dot. *Physical Review B* **82**, 161309 (2010).
- [307] Munsch, M. *et al.* Manipulation of the nuclear spin ensemble in a quantum dot with chirped magnetic resonance pulses. *Nature Nanotechnology* **9**, 671–675 (2014).
- [308] Bulutay, C., Chekhovich, E. A. & Tartakovskii, A. I. Nuclear magnetic resonance inverse spectra of InGaAs quantum dots: Atomistic level structural information. *Physical Review B* **90**, 205425 (2014).
- [309] Wüst, G. *et al.* Role of the electron spin in determining the coherence of the nuclear spins in a quantum dot. *Nature Nanotechnology* **11**, 885–889 (2016).
- [310] Waeber, A. M. *et al.* Pulse control protocols for preserving coherence in dipolar-coupled nuclear spin baths. *Nature Communications* **10**, 3157 (2019).
- [311] Chekhovich, E. A. *et al.* Measurement of the spin temperature of optically cooled nuclei and GaAs hyperfine constants in GaAs/AlGaAs quantum dots. *Nature Materials* **16**, 982–986 (2017).
- [312] Dyakonov, M. & Perel, V. Theory of Optical Spin Orientation of Electrons and Nuclei in Semiconductors. *Modern Problems in Condensed Matter Sciences* **8**, 11–71 (1984).
- [313] Botzem, T. *et al.* Quadrupolar and anisotropy effects on dephasing in two-electron spin qubits in GaAs. *Nature Communications* **7**, 11170 (2016).
- [314] Bethke, P. *et al.* Measurement of Backaction from Electron Spins in a Gate-Defined GaAs Double Quantum dot Coupled to a Mesoscopic Nuclear Spin Bath. *Physical Review Letters* **125**, 047701 (2020).
- [315] Choi, K. S., Goban, A., Papp, S. B., van Enk, S. J. & Kimble, H. J. Entanglement of spin waves among four quantum memories. *Nature* **468**, 412–416 (2010).

- [316] Seewald, G., Hagn, E. & Zech, E. Observation of a Nuclear-Magnon Contribution to the Nuclear Spin-Lattice Relaxation of ^{194}Pt in Ferromagnetic Cobalt. *Physical Review Letters* **78**, 5002–5005 (1997).
- [317] Abdurakhimov, L. V., Bunkov, Y. M. & Konstantinov, D. Normal-Mode Splitting in the Coupled System of Hybridized Nuclear Magnons and Microwave Photons. *Physical Review Letters* **114**, 226402 (2015).
- [318] Wiener, N. *Extrapolation, Interpolation, and Smoothing of Stationary Time Series* (Martino Publishing, 2019).
- [319] Vitagliano, G., Hyllus, P., Egusquiza, I. L. & Tóth, G. Spin Squeezing Inequalities for Arbitrary Spin. *Physical Review Letters* **107**, 240502 (2011).
- [320] Biasiol, G. & Heun, S. Compositional mapping of semiconductor quantum dots and rings. *Physics Reports* **500**, 117–173 (2011).
- [321] Imamoglu, A., Knill, E., Tian, L. & Zoller, P. Optical Pumping of Quantum-Dot Nuclear Spins. *Physical Review Letters* **91**, 017402 (2003).
- [322] Hildmann, J., Kavousanaki, E., Burkard, G. & Ribeiro, H. Quantum limit for nuclear spin polarization in semiconductor quantum dots. *Physical Review B* **89**, 205302 (2014).
- [323] Christ, H., Cirac, J. I. & Giedke, G. Quantum description of nuclear spin cooling in a quantum dot. *Physical Review B* **75**, 155324 (2007).
- [324] Zhu, B., Marino, J., Yao, N. Y., Lukin, M. D. & Demler, E. A. Dicke time crystals in driven-dissipative quantum many-body systems. *New Journal of Physics* **21**, 073028 (2019).
- [325] Gurioli, M., Wang, Z., Rastelli, A., Kuroda, T. & Sanguinetti, S. Droplet epitaxy of semiconductor nanostructures for quantum photonic devices. *Nature Materials* **18**, 799–810 (2019).
- [326] Koguchi, N. & Ishige, K. Growth of GaAs Epitaxial Microcrystals on an S-Terminated GaAs Substrate by Successive Irradiation of Ga and As Molecular Beams. *Japanese Journal of Applied Physics* **32**, 2052–2058 (1993).
- [327] Watanabe, K., Koguchi, N. & Gotoh, Y. Fabrication of GaAs Quantum Dots by Modified Droplet Epitaxy. *Japanese Journal of Applied Physics* **39**, L79–L81 (2000).

- [328] Wang, Z. M., Liang, B. L., Sablon, K. A. & Salamo, G. J. Nanoholes fabricated by self-assembled gallium nanodril on GaAs(100). *Applied Physics Letters* **90**, 113120 (2007).
- [329] Stemmann, A., Heyn, C., Köppen, T., Kipp, T. & Hansen, W. Local droplet etching of nanoholes and rings on GaAs and AlGaAs surfaces. *Applied Physics Letters* **93**, 123108 (2008).
- [330] Heyn, C., Stemmann, A. & Hansen, W. Dynamics of self-assembled droplet etching. *Applied Physics Letters* **95**, 173110 (2009).
- [331] Heyn, C. *et al.* Highly uniform and strain-free GaAs quantum dots fabricated by filling of self-assembled nanoholes. *Applied Physics Letters* **94**, 183113 (2009).
- [332] Sonnenberg, D., Graf, A., Paulava, V., Hansen, W. & Heyn, C. Highly versatile ultra-low density GaAs quantum dots fabricated by filling of self-assembled nanoholes. *Applied Physics Letters* **101**, 143106 (2012).
- [333] Griffiths, I. M., Huang, H., Rastelli, A., Skolnick, M. S. & Chekhovich, E. A. Complete characterization of GaAs gradient-elastic tensors and reconstruction of internal strain in GaAs/AlGaAs quantum dots using nuclear magnetic resonance. *Physical Review B* **99**, 125304 (2019).
- [334] Chekhovich, E. A. *et al.* Cross calibration of deformation potentials and gradient-elastic tensors of GaAs using photoluminescence and nuclear magnetic resonance spectroscopy in GaAs/AlGaAs quantum dot structures. *Physical Review B* **97**, 235311 (2018).
- [335] Jahn, J.-P. *et al.* An artificial Rb atom in a semiconductor with lifetime-limited linewidth. *Physical Review B* **92**, 245439 (2015).
- [336] Béguin, L. *et al.* On-demand semiconductor source of 780-nm single photons with controlled temporal wave packets. *Physical Review B* **97**, 205304 (2018).
- [337] Schweickert, L. *et al.* On-demand generation of background-free single photons from a solid-state source. *Applied Physics Letters* **112**, 093106 (2018).
- [338] Schöll, E. *et al.* Resonance Fluorescence of GaAs Quantum Dots with Near-Unity Photon Indistinguishability. *Nano Letters* **19**, 2404–2410 (2019).

- [339] Keil, R. *et al.* Solid-state ensemble of highly entangled photon sources at rubidium atomic transitions. *Nature Communications* **8**, 15501 (2017).
- [340] Kumar, S. *et al.* Strain-induced tuning of the emission wavelength of high quality GaAs/AlGaAs quantum dots in the spectral range of the 87 Rb D 2 lines. *Applied Physics Letters* **99**, 161118 (2011).
- [341] Atkinson, P., Zallo, E. & Schmidt, O. G. Independent wavelength and density control of uniform GaAs/AlGaAs quantum dots grown by infilling self-assembled nanoholes. *Journal of Applied Physics* **112**, 054303 (2012).
- [342] Löbl, M. C. *et al.* Correlations between optical properties and Voronoi-cell area of quantum dots. *Physical Review B* **100**, 155402 (2019).
- [343] Huo, Y. H., Rastelli, A. & Schmidt, O. G. Ultra-small excitonic fine structure splitting in highly symmetric quantum dots on GaAs (001) substrate. *Applied Physics Letters* **102**, 152105 (2013).
- [344] Huber, D. *et al.* Highly indistinguishable and strongly entangled photons from symmetric GaAs quantum dots. *Nature Communications* **8**, 15506 (2017).
- [345] Huber, D., Reindl, M., Aberl, J., Rastelli, A. & Trotta, R. Semiconductor quantum dots as an ideal source of polarization-entangled photon pairs on-demand: a review. *Journal of Optics* **20**, 073002 (2018).
- [346] Liu, G.-Q., Feng, X., Wang, N., Li, Q. & Liu, R.-B. Coherent quantum control of nitrogen-vacancy center spins near 1000 kelvin. *Nature Communications* **10**, 1344 (2019).
- [347] Chen, Y., Zopf, M., Keil, R., Ding, F. & Schmidt, O. G. Highly-efficient extraction of entangled photons from quantum dots using a broadband optical antenna. *Nature Communications* **9**, 2994 (2018).
- [348] Schimpf, C. *et al.* Quantum dots as potential sources of strongly entangled photons: Perspectives and challenges for applications in quantum networks. *Applied Physics Letters* **118**, 100502 (2021).
- [349] Schimpf, C. *et al.* Quantum cryptography with highly entangled photons from semiconductor quantum dots. *Science Advances* **7**, eabe8905 (2021).

- [350] Trotta, R. *et al.* Universal recovery of the energy-level degeneracy of bright excitons in InGaAs quantum dots without a structure symmetry. *Physical Review Letters* **109**, 147401 (2012).
- [351] Seidl, S. *et al.* Effect of uniaxial stress on excitons in a self-assembled quantum dot. *Applied Physics Letters* **88**, 203113 (2006).
- [352] Plumhof, J. D. *et al.* Strain-induced anticrossing of bright exciton levels in single self-assembled GaAs/Al_xGa_{1-x}As and In_xGa_{1-x}As/GaAs quantum dots. *Physical Review B* **83**, 121302 (2011).
- [353] Rastelli, A. *et al.* Controlling quantum dot emission by integration of semiconductor nanomembranes onto piezoelectric actuators. *Physica Status Solidi (B) Basic Research* **249**, 687–696 (2012).
- [354] Sallen, G. *et al.* Nuclear magnetization in gallium arsenide quantum dots at zero magnetic field. *Nature Communications* **5**, 3268 (2014).
- [355] Zhai, L. *et al.* Low-noise GaAs quantum dots for quantum photonics. *Nature Communications* **11**, 4745 (2020).
- [356] Liu, J. *et al.* Photoluminescence characterization of wetting layer and carrier dynamics for coupled InGaAs/GaAs surface quantum dot pair structures. *Optics Express* **28**, 20704 (2020).
- [357] Huber, D. *et al.* Single-particle-picture breakdown in laterally weakly confining GaAs quantum dots. *Physical Review B* **100**, 235425 (2019).
- [358] Hopfmann, C. *et al.* Deterministic preparation of spin qubits in droplet etched GaAs quantum dots using quasi-resonant excitation (2020).
- [359] Zhai, L. *et al.* Quantum Interference of Identical Photons from Remote Quantum Dots (2021).
- [360] Uhrig, G. S. Keeping a quantum bit alive by optimized π -pulse sequences. *Physical Review Letters* **98** (2007).
- [361] Lee, B., Witzel, W. M. & Das Sarma, S. Universal Pulse Sequence to Minimize Spin Dephasing in the Central Spin Decoherence Problem. *Physical Review Letters* **100**, 160505 (2008).
- [362] Appel, M. H. *et al.* Coherent Spin-Photon Interface with Waveguide Induced Cycling Transitions. *Physical Review Letters* **126**, 013602 (2021).

- [363] Tiurev, K. *et al.* High-fidelity multi-photon-entangled cluster state with solid-state quantum emitters in photonic nanostructures (2020).
- [364] Farfurnik, D., Pettit, R. M., Luo, Z., Ravan, S. M. & Waks, E. Arbitrary sequenced spin control of a Quantum Dot strongly coupled to a photonic crystal cavity. In *Frontiers in Optics / Laser Science*, FW4C.5 (OSA, Washington, D.C., 2020).
- [365] Debroux, R. *et al.* Quantum control of the tin-vacancy spin qubit in diamond (2021).
- [366] Sharman, K., Asadi, F. K., Wein, S. C. & Simon, C. Quantum repeaters based on individual electron spins and nuclear-spin-ensemble memories in quantum dots (2020).
- [367] Giedke, G., Taylor, J. M., D'Alessandro, D., Lukin, M. D. & Imamoglu, A. Quantum measurement of a mesoscopic spin ensemble. *Physical Review A* **74**, 032316 (2006).
- [368] Wineland, D. J., Bollinger, J. J., Itano, W. M., Moore, F. L. & Heinzen, D. J. Spin squeezing and reduced quantum noise in spectroscopy. *Physical Review A* **46**, R6797–R6800 (1992).
- [369] Wineland, D. J., Bollinger, J. J., Itano, W. M. & Heinzen, D. J. Squeezed atomic states and projection noise in spectroscopy. *Physical Review A* **50**, 67–88 (1994).
- [370] Bollinger, J. J. ., Itano, W. M., Wineland, D. J. & Heinzen, D. J. Optimal frequency measurements with maximally correlated states. *Physical Review A* **54**, R4649–R4652 (1996).
- [371] Rotondo, P., Cosentino Lagomarsino, M. & Viola, G. Dicke Simulators with Emergent Collective Quantum Computational Abilities. *Physical Review Letters* **114**, 143601 (2015).
- [372] Kaluzny, Y., Goy, P., Gross, M., Raimond, J. M. & Haroche, S. Observation of Self-Induced Rabi Oscillations in Two-Level Atoms Excited Inside a Resonant Cavity: The Ringing Regime of Superradiance. *Physical Review Letters* **51**, 1175–1178 (1983).
- [373] Choi, S. *et al.* Observation of discrete time-crystalline order in a disordered dipolar many-body system. *Nature* **543**, 221–225 (2017).